

**COMPUTATIONAL MODELING OF BLOCH SURFACE
WAVES IN ONE-DIMENSIONAL PERIODIC AND
APERIODIC MULTILAYER STRUCTURES**

by

Vijay Koju

A Dissertation

Presented to the Faculty of the Computational Science Program

Middle Tennessee State University

May 2017

In Partial Fulfillment

of the Requirements for the Degree

Doctorate of Philosophy in Computational Sciences

Dissertation Committee:

Dr. William M. Robertson, Chair

Dr. Abdul Q. M. Khaliq

Dr. Vishwas Bedekar,

Dr. Justin S. Baba

Copyright © 2017, Vijay Koju

To my parents and wonderful wife.

ACKNOWLEDGMENTS

I would like to express my deepest gratitude to my advisor, Dr. William M. Robertson, for his unrelenting support during the course of this dissertation. Without his scholarly guidance this dissertation would not have been possible. I am grateful to him for introducing me to the exciting field of photonics and guiding me through it. Working along with him, I have learned and acquired a vast amount of skills necessary for solving challenging problems in research and in life. He has not only been a very supporting academic advisor, but also a guardian-figure who has supported me and my wife through difficult times.

I would also like to thank my committee members, Dr. Abdul Q. M. Khaliq, Dr. Vishwas Bedekar, and Dr. Justin S. Baba for their constructive inputs and suggestions on my dissertation.

Special thanks are in order for our program director, Dr. John F. Wallin and the Physics and Astronomy department chair, Dr. Ronald Henderson for their full support, both academic and personal, throughout my graduate career.

I would also like to extend my thanks to all the faculty members and staff of the Computational Science Program and Physics and Astronomy department, along with my colleagues for helping me in any way possible. Last but not the least, I would like to thank Middle Tennessee State University and the Computational Science program for funding my graduate studies and research.

ABSTRACT

Photonic crystals and their use in exciting Bloch surface waves have received immense attention over the past few decades. This interest is mainly due to their applications in bio-sensing, wave-guiding, and other optical phenomena such as surface field enhanced Raman spectroscopy. Improvement in numerical modeling techniques, state of the art computing resources, and advances in fabrication techniques have also assisted in growing interest in this field. The ability to model photonic crystals computationally has benefited both the theoretical as well as experimental communities. It helps the theoretical physicists in solving complex problems which cannot be solved analytically and helps to acquire useful insights that cannot be obtained otherwise. Experimentalists, on the other hand, can test different variants of their devices by changing device parameters to optimize performance before fabrication. In this dissertation, we develop two commonly used numerical techniques, namely transfer matrix method, and rigorous coupled wave analysis, in C++ and MATLAB, and use two additional software packages, one open-source and another commercial, to model one-dimensional photonic crystals. Different variants of one-dimensional multilayered structures such as perfectly periodic dielectric multilayers, quasicrystals, aperiodic multilayer are modeled, along with one-dimensional photonic crystals with gratings on the top layer.

Applications of Bloch surface waves, along with new and novel aperiodic dielectric multilayer structures that support Bloch surface waves are explored in this dissertation. We demonstrate a slow light configuration that makes use of Bloch Surface Waves as an intermediate excitation in a double-prism tunneling configuration. This method is simple compared to the more usual techniques for slowing light using the phenomenon of electromagnetically induced transparency in atomic gases or doped ionic crystals operated at temperatures below 4K. Using a semi-numerical approach, we show that a 1D photonic crystal, a multilayer structure composed of alternating layers of TiO_2 and SiO_2 , can be used to slow down light by a factor of up to 400. The results also show that better control of the speed of light can be achieved by changing the number of bilayers and the air-gap thickness appropriately.

The existence of Bloch surface waves in periodic dielectric multilayer structures with a surface defect is well-known. Not yet recognized is that quasi-crystals and aperiodic dielectric multilayers can also support Bloch-like surface waves. We numerically show the excitation of Bloch-like surface waves in Fibonacci quasi-crystals, Thue-Morse aperiodic dielectric multilayers using the prism coupling method. We report improved surface electric field intensity and penetration depth of Bloch-like surface waves in the air side in such structures compared to their periodic counterparts.

Bloch surface waves have also demonstrated significant potential in the field of biosensing technology. We further extend our study into a new type of multilayer structure based on Maximal-length sequence, which is a pseudo random sequence. We study the characteristics of Bloch surface waves in a 32 layered Maximal-length sequence multilayer and perform angular, as well as spectral sensitivity analysis for refractive index change detection. We demonstrate numerically that Maximal-length sequence multilayers significantly enhance the sensitivity of Bloch surface waves.

Another type of structure that support Bloch surface waves are dielectric multilayer structures with a grating profile on the top-most layer. The grating profile adds an additional degree of freedom to the phase matching conditions for Bloch surface wave excitation. In such structures, the conditions for Bloch surface wave coupling can also be achieved by rotating both polar and azimuthal angles. The generation of Bloch surface waves as a function of azimuthal angle have similar characteristics to conventional grating coupled Bloch surface waves. However, azimuthal generated Bloch surface waves have enhanced angular sensitivity compared to conventional polar angle coupled modes, which makes them appropriate for detecting tiny variations in surface refractive index due to the addition of nano-particles such as protein molecules.

TABLE OF CONTENTS

LIST OF TABLES	x
LIST OF FIGURES	xi
CHAPTER 1: INTRODUCTION	1
1.1 Photonic Crystals	1
1.2 Bloch Surface Wave	4
1.3 Bloch Waves and Band Structures	9
CHAPTER 2: NUMERICAL TECHNIQUES	14
2.1 Transfer Matrix Method using Scattering Matrices	14
2.1.1 Scattering Matrix for a Layer	18
2.1.2 Redheffer Star Product	20
2.1.3 Global Scattering Matrix	21
2.1.4 Calculating Transmitted and Reflected Electric Field	23
2.1.5 Calculating Transmittance and Reflectance	24
2.2 Rigorous Coupled Wave Analysis	24
2.2.1 Scattering Matrix for a Layer	30
2.2.2 Redheffer Star Product	32
2.2.3 Global Scattering Matrix	33
2.2.4 Calculating Transmitted and Reflected Electric Field	35
2.2.5 Calculating Diffraction Efficiencies	36
2.2.6 Calculating Overall Reflectance and Transmittance	36
2.3 Finite-Difference Time-Domain Method	37
2.4 Finite Element Method	39

2.4.1	Weak Formulation	41
CHAPTER 3:	SLOW LIGHT BY BLOCH SURFACE WAVE TUNNELING	43
3.1	Introduction	43
3.2	Simulation Approach	44
3.3	Results and Discussions	46
3.4	Summary	48
CHAPTER 4:	EXCITATION OF BLOCH-LIKE SURFACE WAVES IN	
	QUASI-CRYSTALS AND APERIODIC DIELECTRIC MULTILAYERS	51
4.1	Introduction	51
4.2	Materials and Computational Method	52
4.3	Results and Discussions	56
4.4	Summary	65
CHAPTER 5:	SENSITIVITY ENHANCEMENT VIA SLOW BLOCH SUR-	
	FACE WAVE IN MAXIMAL LENGTH SEQUENCE MULTILAYERS..	66
5.1	Introduction	66
5.2	Results and Discussions	68
5.3	Summary	73
CHAPTER 6:	LEAKY BLOCH-LIKE SURFACE WAVES IN THE RADIATION-	
	CONTINUUM FOR SENSITIVITY ENHANCED BIOSENSORS VIA	
	AZIMUTHAL INTERROGATION	79
6.1	Introduction	79
6.2	Computational Method	80
6.3	Results and Discussions	83
6.4	Summary	88
CHAPTER 7:	CONCLUSION AND FUTURE WORK	90

BIBLIOGRAPHY	93
APPENDICES	108
APPENDIX A: MODELING AZIMUTHAL BLOCH SURFACE WAVE IN	
COMSOL MULTIPHYSICS	109
A.1 Model Setup	109
A.2 Geometry Construction	111
A.3 Material Setup	117
A.4 Physics Setup	118
A.5 Mesh Setup	127
A.6 Results	132

LIST OF TABLES

1	First four generations of FQCs and TMADMs	52
2	Maximal-length sequence examples	68
A.1	Parameters used in modeling 3D azimuthal Bloch surface wave	110
A.2	Refractive index parameter for superstrate layer	117
A.3	Refractive index parameter for SiO ₂	118
A.4	Refractive index parameter for TiO ₂	118
A.5	Reflectance and Transmittance from S-parameters	135

LIST OF FIGURES

1	Examples of one, two, and three dimensional photonic crystals. This image is directly extracted from [1].	2
2	Illustrations of infinitely extending perfect 1DPC (a), finite 1DPC with defect (b), and finite 1DPC with surface defect.	3
3	(a) Prism coupling (b) Grating coupling	5
4	(a) Prism configuration for exciting BSW (b) Band structure of a 16-layered TiO ₂ -SiO ₂ multilayer (c-top) Reflectivity versus angle for light coupled to BSW in the multilayer at $\lambda = 632.8$ nm (c-bottom) Reflectivity versus wavelength for light coupled to BSW in the multilayer at $\theta_{inc} = 44.4^\circ$ (d-top) $ E ^2$ field profile of the BSW in the multilayer at $\theta_{inc} = 44.4^\circ$ and $\lambda = 632.8$ nm (d-middle) Cross-sectional view of a 16-layered TiO ₂ -SiO ₂ multilayer with the top defect layer on a glass substrate (d-bottom) $ E ^2$ amplitude of the BSW in the multilayer at $\theta_{inc} = 44.4^\circ$ and $\lambda = 632.8$ nm.	7
5	Experimental BSW resonance array scan showing eight spots of Bovine Serum Albumin (BSA) (Rows 1 and 2) and four spots of Immunoglobulin G (IgG) (Row 3) before (left plot) and after (right plot) exposure to anti-BSA.	9
6	An illustration of infinitely periodic multilayer dielectric structure with plane wave amplitudes associated with the n^{th} unit cell and its neighboring cells.	10
7	A schematic of a 1D multilayer structure.	15
8	Field representations in the i^{th} layer of a 1D multilayer.	18
9	Representation of the scattering matrix of a single layer.	19
10	Representation of global scattering matrix.	22
11	A schematic of a 1D multilayer structure with a grating on the top layer.	25
12	Field representations in the i^{th} layer of a 1D multilayer.	30

13	Representation of the scattering matrix of a single layer.	31
14	Representation of global scattering matrix.	34
15	3D FDTD Yee grid.	37
16	A schematic diagram of the configuration for slow light generation using BSW as an intermediate excitation.	45
17	Surface dispersion diagram for an 8 bilayer multilayer TiO ₂ -SiO ₂ PBGM used in the simulations. The red dashed line represents the limiting lightline in air. The green and blue shaded areas represent radiative and non-radiative regions respectively into the multilayer. The plot units are in reduced angular frequency ($2\pi c/\Lambda$) and wavevector ($2\pi/\Lambda$) where Λ is the periodicity of the multilayer.	49
18	(a) Delay time as a function of wavelength for four different air gap values. (b) Incident (top) and transmitted (bottom) pulses showing 4.209 ps delay. .	50
19	(a) Group Index (blue) and corresponding transmittance (green) as a function of air-gap thickness with the number of TiO ₂ -SiO ₂ bilayers = 8. (b) Group Index (blue) and Air Gap thickness (green) as a function of number of bilayers.	50
20	(a) A schematic of the prism coupling technique to excite Bloch-like surface wave in a dielectric multilayer. (b) A 2D schematic with the system parameters.	54
21	BLSWs in FQC. (a) Reflection map of a 34 layered FQC ($j = 7$) in contact with air as a function of wavelength (λ) and angle of incidence (AoI). (b) Dispersion curves of BLSW ₁ and BLSW ₂ . (c-d) BLSW assisted E-field intensity at the surface for (c) $\lambda = 443.2$ nm and AoI = 45.67° , (d) $\lambda = 760$ nm and AoI = 42.14° . (e-f) Reflectivity curves as a function of AoI at (e) $\lambda = 443.2$ nm, (f) $\lambda = 760$ nm.	57

22	(a) BLSW assisted E-field intensity at the surface of a 13 layered FQC ($j = 5$) at $\lambda = 475$ nm and $\text{AoI} = 42.36^\circ$. (b) Corresponding reflectivity curve for $\lambda = 475$ nm. (a) BLSW assisted E-field intensity at the surface of a 89 layered FQC ($j = 9$) at $\lambda = 440$ nm and $\text{AoI} = 46.53^\circ$. (b) Corresponding reflectivity curve for $\lambda = 440$ nm.	58
23	BLSWs in TMADM. (a) Reflection map of a 32 layered TMADM ($j = 5$) in contact with air as a function of λ and AoI . (b) Dispersion curves of BLSW_1 , BLSW_2 , BLSW_3 and BLSW_4 . (c-f) BLSW assisted E-field intensity at the surface for (c) $\lambda = 762.4$ nm and $\text{AoI} = 42^\circ$, (d) $\lambda = 701.4$ nm and $\text{AoI} = 42.01^\circ$, (e) $\lambda = 488.1$ nm and $\text{AoI} = 41.86^\circ$, (f) $\lambda = 465.1$ nm and $\text{AoI} = 41.85^\circ$.	59
24	(a) BLSW assisted E-field intensity at the surface of a 8 layered TMADM ($j = 3$) at $\lambda = 460$ nm and $\text{AoI} = 42.46^\circ$. (b) Corresponding reflectivity curve for $\lambda = 460$ nm. (a) BLSW assisted E-field intensity at the surface of a 8 layered TMADM ($j = 3$) at $\lambda = 700$ nm and $\text{AoI} = 43.63^\circ$. (b) Corresponding reflectivity curve for $\lambda = 700$ nm.	60
25	BSW assisted E-field intensity at the surface of a periodic counterpart (32 layers) of FQC and TMADM at wavelength 440 nm and incident angle 53.16° .	61
26	(a) Maximum E-field intensity at the surface of the 34 layered FQC (red circle), 32 layered TMADM (blue circle) , and 32 layered PDM (black circle). (b) $\text{Exp}(-1)$ penetration depth beyond the surface of the FQC, TMADM, and PDM into the air side.	62
27	Reflectivity curves of (a) a FQC ($j = 7$) at $\lambda = 443.2$ nm (b) a TMADM ($j = 5$) at $\lambda = 465.1$ nm for different refractive indices n_N of superstrate layer.	62
28	A schematic of a prism coupling technique (Kretschmann configuration) to excite Bloch surface wave using a dielectric multilayer.	67

29	Reflection maps of a 36-layered maximal length sequence multilayer over a wavelength range of 1115nm-1295nm and incident angle range of 66° - 85° for superstrate indices (a) 1.32, (b) 1.33, (c) 1.34, (d) 1.35, (e) 1.36, and (f) 1.37. Shift in the BSW mode as a function of superstrate index is clearly observed. The dotted lines represent the cross-sections of the reflection map plotted in Figure 30(a), and the solid circle in (b) is the wavelength-angle pair for the field enhancement plot shown in Figure 30(b).	69
30	(a) Reflectivity curves of a 36-layered maximal length sequence multilayer at the wavelength 1159.88 nm and over the incident angle range of 72° - 85° for different superstrate indices. The red solid circles connected by solid lines represent the figure of merit for the respective BSWs. (b) Electric field enhancement at the wavelength 1159.88 nm and incident angle 77.07°	74
31	(a) Angular, and (b) spectral sensitivity of a 36-layered maximal length sequence multilayer for different superstrate refractive index changes.	75
32	(a) Angular, and (b) spectral sensitivity of a 36-layered maximal length sequence multilayer for different superstrate refractive index changes.	76
33	(a) Dispersion curves of the BSWs extracted from the reflection maps (Figure 28) using coordinate transformation of the incident angle axis to a parallel wave vector axis. The dotted lines represent the light lines for respective superstrate refractive indices. (b) Group velocities for the dispersion curves .	77
34	(a) Reflectivity curve (b) Electric field profile of a 31 layered maximal-length sequence multilayer using Otto configuration.	78
35	Schematic of a grating coupling technique to excite leaky Bloch surface waves on the surface of a dielectric multilayer.	82

36	Leaky Bloch surface wave at $\phi = 0^\circ$. (a) $\text{TiO}_2\text{-SiO}_2$ multilayer with grating on the top layer. (b) Dispersion curves of the leaky BSWs supported by the structure. The green region is the radiative region (c)-(d) Reflectance of BSW as a function of incident angle and wavelength respectively. (e)-(f) Electric field profiles of BSW modes. The red and blue circles at the resonance peaks represent the reflectance at the corresponding circles in (b).	84
37	Azimuthal dispersion curves of BSWs for different values of superstrate refractive indices and $\theta_{inc} = 5.4^\circ$	85
38	(a) BSW modes as a function of superstrate refractive index and azimuthal angle for different values of θ_{inc} and $\lambda = 632.8$ nm. (b) Azimuthal sensitivity of BSWs.	88
39	(a) Reflectivity curves as a function of Azimuthal angle for different values of n_{sup} . The wavelength (λ) and incident angle (θ) are fixed at 632.8 nm and 5.4° respectively. The results obtained using COMSOL (circles) and an in-house 3D RCWA code (solid lines) show good agreement. (b) x-y (c) x-z (d) y-z plane views of azimuthal BSW at the resonance peak indicated by the arrows in (a).	89
40	Geometries of multilayer structure with grating profile showing different components	119
41	Input and output port boundary condition parameters	122
42	Floquet periodic boundary condition parameters	126
43	Mesh parameters	130
44	Electric field profile, y component, of azimuthal Bloch surface wave	133
45	Reflectance (R) and Transmittance (T) of azimuthal Bloch surface wave	134

CHAPTER 1

INTRODUCTION

When a ray of light passes through a glass slab, some of the light is reflected back from the first interface whereas the rest propagates into the glass. That light travels until it hits the second interface. At the second interface, some of the light is reflected back to the glass and some is transmitted to the air. If a second slab of glass with a slightly different material properties is attached to one side of the first slab, the light is reflected at three interfaces and has to travel through two different materials. The interaction of light with the two slab system is thus more complicated. If multiple copies of the two slab system are stitched together, a periodic multilayered structure is obtained. Light in such structures is multiply reflected and refracted in a similar fashion as in the two slab system, but due to the increased number of interfaces, the interaction of light with periodic multilayered structures is more complex. The periodicity of such a material system gives rise to new features which cannot be observed otherwise. Light of certain wavelengths cannot propagate through such periodic multilayered structures and hence are completely reflected back. The reason for this effect, which was first explained by Lord Rayleigh in 1887, is that the light wave is partially reflected and partially transmitted at each interface, and the multiple reflections from the periodic layer interfaces interact destructively to eliminate the forward propagating wave [1]. Such periodic multilayer structures are known in modern terminology as one-dimensional photonic crystals (1DPC).

1.1 Photonic Crystals

Photonic crystals are man-made periodic materials that when interact with light can “mold” or control the properties and flow of light [1]. The underlying theoretical background of photonic crystals and their interaction with photons was laid out by Yablonovitch [2] and John [3] independently in 1987. This theoretical model is similar to the interaction between ordinary

crystals and electrons which results in electronic band gaps and led to an understanding of semiconductor action. The ground work of Yablonovitch and John led scientists and engi-

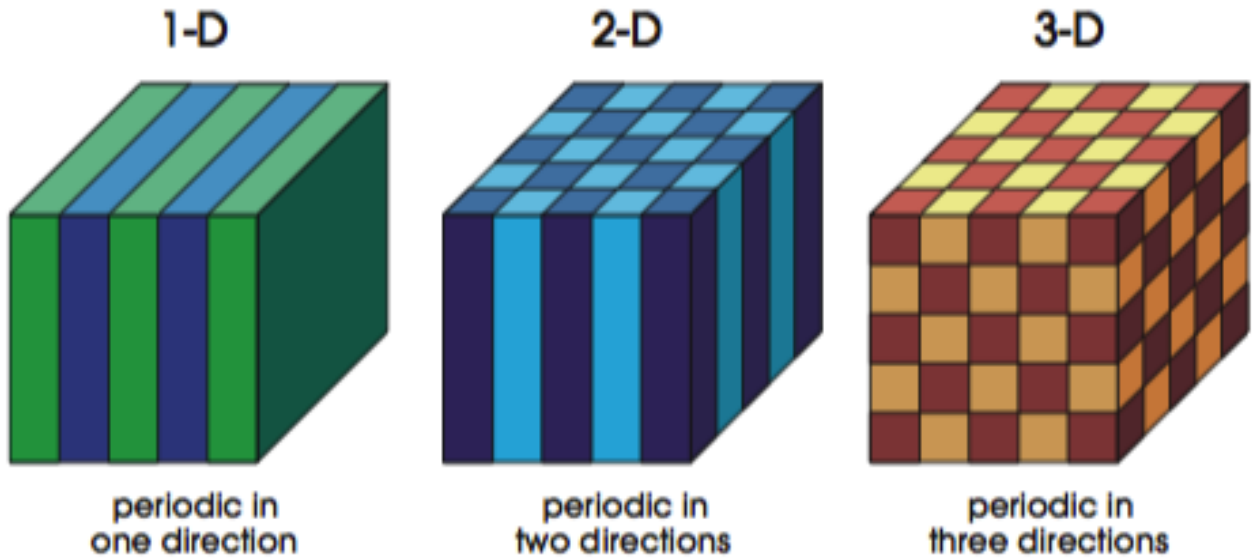


Figure 1: Examples of one, two, and three dimensional photonic crystals. This image is directly extracted from [1].

neers to design, fabricate, and study the properties of different types of photonic crystals, from simple one-dimensional multilayers to complex three-dimensional photonic crystals. Examples of photonic crystals of different dimensions is presented in Figure 1. They forbid light of certain wavelengths to propagate through them. Such wavelength regions are called forbidden bands or photonic band gaps (PBG), and for this reason photonic crystals are also known as PBG materials. Initial experimental investigation of such PBG material and their photonic band structures were done by Robertson et. al. in 1992 [4] and 1993 [5].

Propagation of electromagnetic waves (EM) in PBG materials is well described by the Bloch-Floquet theorem. According to the theorem, when a light wave with a wavelength in the PBG is sent onto the top interface of the photonic crystal from outside, the wave cannot extend into the crystal because no purely real wave vector exists for any mode at that wavelength. Instead, the wave vector is complex, the imaginary part of which is responsible for the exponentially decaying wave amplitude inside the crystal. Thus, the modes in the

crystal are evanescent:

$$\mathbf{E}_K(z, x) = \mathbf{E}_K(z) e^{iKz} e^{i\beta x}, \quad (1)$$

where the Bloch wave number $K = m\pi/\Lambda + iK_i$ (refer section 1.3 for details). Although evanescent modes in photonic crystals are valid solutions of the electromagnetic eigenvalue problem, they diverge as z – direction of propagation – goes to $\pm\infty$, depending on the sign of K_i . Thus, they cannot be excited in a perfectly periodic multilayer structure of infinite extent (Figure 2(a)). However, a defect – layer with a different thickness or refractive index than other such layers – can suppress the exponential growth and thus sustain an evanescent mode. Examples of periodic multilayers are depicted in Figure 2 (b) and (c). This enables photonic crystals to have localized modes with wavelengths inside the PBG.

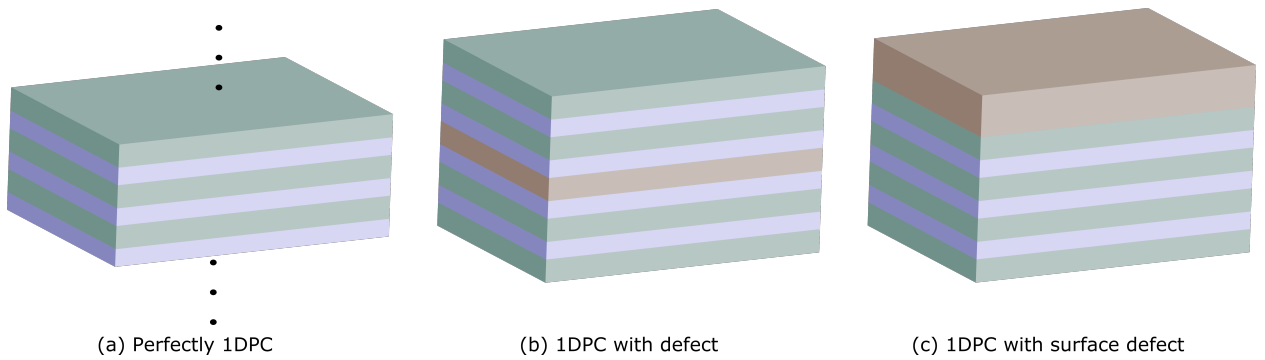


Figure 2: Illustrations of infinitely extending perfect 1DPC (a), finite 1DPC with defect (b), and finite 1DPC with surface defect.

A defect in the center of a periodic PBG material (see Figure 2(b)) creates a defect state in which light can become localized. The periodic multilayer films at both the sides of the defect behave as frequency-specific mirrors. A propagating light wave with such frequency is thus reflected back and forth from either sides of the defect and gets trapped inside it. The defect acts as a resonant cavity, which can be utilized in many applications. For example, resonant cavities can increase the efficiency of zero threshold lasers, as the density of states at the resonance frequency is very high. The same property can also be utilized to creating bandpass filters known as the dielectric Fabry-Perot filters.

1.2 Bloch Surface Wave

In 1977, Yeh et al. [6] studied electromagnetic (EM) propagation in periodic stratified media and explained the theoretical basis for surface EM waves in dielectric multilayer structures. Later in 1991, Meade et al. [7] did a comprehensive study and predicted that PBG structures could support surface EM waves – propagating EM waves localized to the surface of a PBG. Existence of four kinds of surface modes, modes that extend in both the air region and crystal region, modes that extend in the crystal region and decay in the air region, modes that decay in the crystal region and extend the in air region, and modes that decay in both the air and crystal region were shown theoretically. The fourth kind of surface mode that decay exponentially in both the air and crystal sides was experimentally realized by Robertson et al. [8–10] in the following years. These modes called the Bloch Surface Waves (BSW) were originally thought to be detrimental to many of the projected PBG applications because they were optical modes that existed within the forbidden bandgap. However, it was later shown that the dispersion of these modes could be adjusted by the termination conditions of the PBG. BSWs have become recognized as an important excitation in applications in sensing, fast and slow light, and non-linear optics.

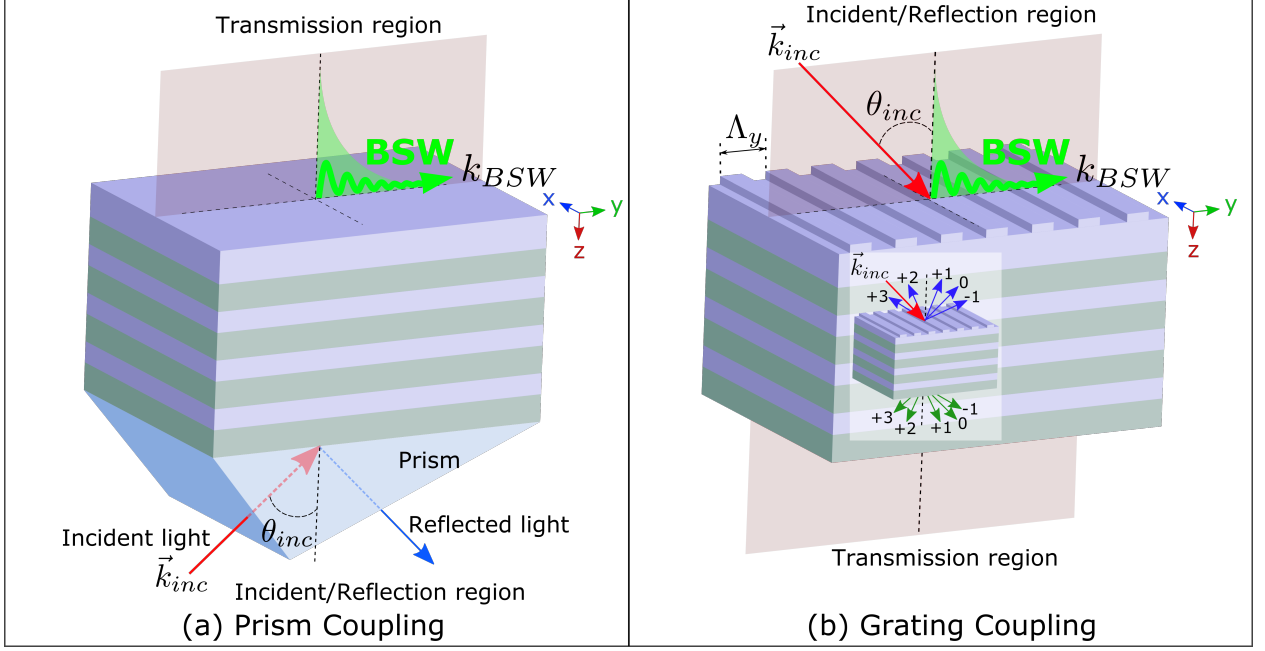


Figure 3: (a) Prism coupling (b) Grating coupling

BSWs can only exist at the surface of PBG structures with a surface defect. An example of such a PBG structure is presented in Figure 2(b). The mode frequency is not allowed to extend into the 1DPC due to the PBG and it decays exponentially in the air side, i.e., these modes are evanescent in nature. Although such modes are intrinsically present at dielectric-air interfaces, they are non-radiative in nature; their momentum is larger than the free-space wave momentum. Due to the momentum mismatch, BSW modes cannot be excited directly by light incident from the air side. This restriction on optical generation of the BSWs can be circumvented either by prism coupling [8, 11, 12] or by grating coupling [13] as shown in Figure 3 (a) and (b) respectively.

BSW using the prism coupling is excited when the parallel wavevector (β) on the top of the 1DPC is equal to k_{BSW} as given by

$$\beta = k_{BSW} = k_0 n_{glass} \sin(\theta_{inc}), \quad (2)$$

where $k_0 = 2\pi/\lambda_0$ is the free-space wave number, n_{glass} is the refractive index of the prism, and θ_{inc} is the angle of incidence of the input wave. Although this technique is well un-

derstood, widely used, and easy to model theoretically, because of the necessity of a bulky prism, it is not conducive to creating practical optical devices on the nanoscale. The purpose of the prism is to decrease the effective wavelength of the light so that it is able to couple to non-radiative surface waves. An alternative technique is to use a grating structure (see Figure 3 (b)) that relaxes the parallel wavevector conservation condition at the surface and essentially permits light to be diffracted directly into surface modes without the use of a prism. As shown in the inset of Figure 3 (b), in the presence of surface gratings on a 1DPC, the incident light is diffracted into several diffraction orders ($m = \pm 1, \pm 2, \dots$). These diffraction orders from the grating can provide the additional momentum for the incident light required to couple to the BSWs as given by

$$k_m = k_{inc} \pm mG \quad m = \pm 1, \pm 2, \dots, \quad (3)$$

where k_m is the wave number of the diffracted beam, $k_{inc} = k_0 \sin(\theta_{inc})$ is the parallel component of the incident wave number, m is the diffraction order, and $G = 2\pi/\Lambda_y$ is the grating wave number, Λ_y being the grating period. When k_m , with the appropriate additional momentum supplied by the grating, equals k_{BSW} , BSW can be excited. If we know the parallel wavevector component (k_{BSW}) where the BSW can be generated, the required angle of incidence for the incident wave can be obtained by $\theta_{inc} = \sin^{-1}((k_{BSW} - G)/k_0)$ for $m = 1$.

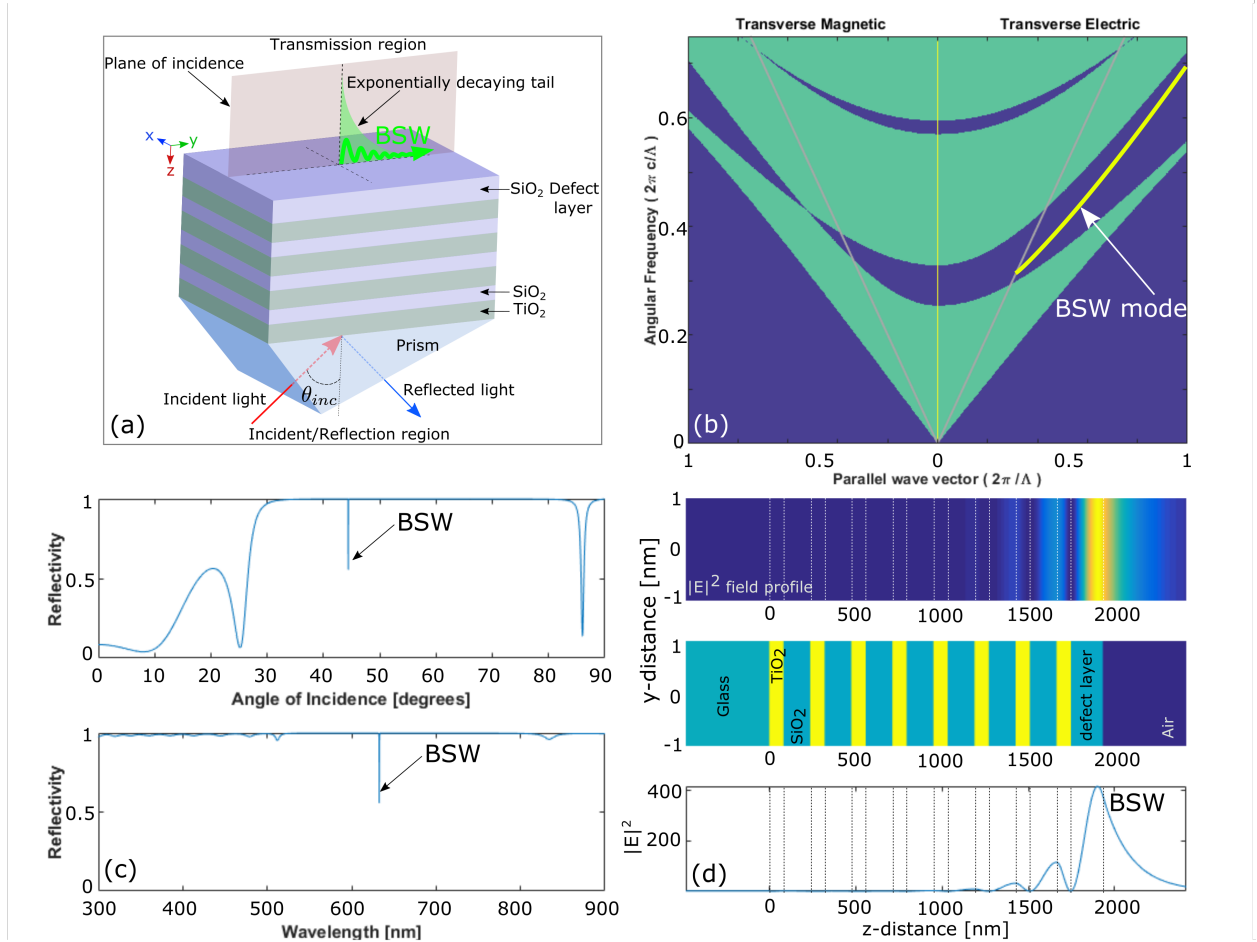


Figure 4: (a) Prism configuration for exciting BSW (b) Band structure of a 16-layered TiO_2 - SiO_2 multilayer (c-top) Reflectivity versus angle for light coupled to BSW in the multilayer at $\lambda = 632.8$ nm (c-bottom) Reflectivity versus wavelength for light coupled to BSW in the multilayer at $\theta_{inc} = 44.4^\circ$ (d-top) $|E|^2$ field profile of the BSW in the multilayer at $\theta_{inc} = 44.4^\circ$ and $\lambda = 632.8$ nm (d-middle) Cross-sectional view of a 16-layered TiO_2 - SiO_2 multilayer with the top defect layer on a glass substrate (d-bottom) $|E|^2$ amplitude of the BSW in the multilayer at $\theta_{inc} = 44.4^\circ$ and $\lambda = 632.8$ nm.

Figure 4 shows a general picture of BSW, its excitation in a 1DPC and its properties. The 1DPC that we employ here is a stack of TiO_2 ($\epsilon_{\text{TiO}_2} = 4.8400 - 0.0007i$) and SiO_2

($\epsilon_{SiO_2} = 2.1316 - 0.0001i$) on a glass substrate ($\epsilon = 2.25$). The thicknesses of TiO_2 and SiO_2 are 82.8 nm and 154.9 nm respectively and the defect layer is 185 nm. The BSW excitation shown in Figure 4 (a), as explained earlier, can only be excited at certain wavelengths of light. This can be clearly seen in Figure 4 (b), which shows the band structure of a 16-layered 1DPC for both TE and TM mode. The green region indicates the allowed wavelengths of the EM waves that can propagate in the 1DPC and the blue region indicates the forbidden wavelengths or the forbidden band-gap. The slanted gray lines are the light-lines in air; the region to the left of the light line in the TE mode and right of the TM mode are the wavelengths of EM waves allowed in air. The yellow stripe in the forbidden band-gap in the TE mode is the BSW mode. It lies to the right of the air light-line and thus cannot be accessed directly through air.

Every point that lies on the yellow stripe indicates a specific pair of wavevector at a specific angle of incidence (θ) and wavelength (λ) where the BSW can be excited. The reflectivity at one such pair ($\theta = 44.4^\circ$, $\lambda = 632.8$ nm) is shown in 4 (c). The sharp dips that we observe on both the reflectivity curves is due to the transfer of energy from the incident EM wave to the BSW that propagates along the interface of the crystal and air. The electric field profile and amplitude of the BSW at the incidence angle-wavelength pair is illustrated in Figure 4 (d).

BSW extends slightly into the air side and creates a tightly confined EM field which decays exponentially. This property has been used extensively by many researchers for bio-sensing applications [14–24]. For example, Figure 5 shows an example of BSW sensing due to resonant angle shift as a means of reading protein arrays without the need of fluorescent labels. The addition of external material, eg. chemical electrolyte, on the surface of the 1DPC changes the effective refractive index of the sensing medium. As a result, the BSW condition changes and the reflectivity dips shift to the left or right of the previous reflectivity dip position on either the reflectivity versus wavelength or reflectivity versus angle. The angular or spectral change between the dips help analyze the electrolyte and detect the changes in it.

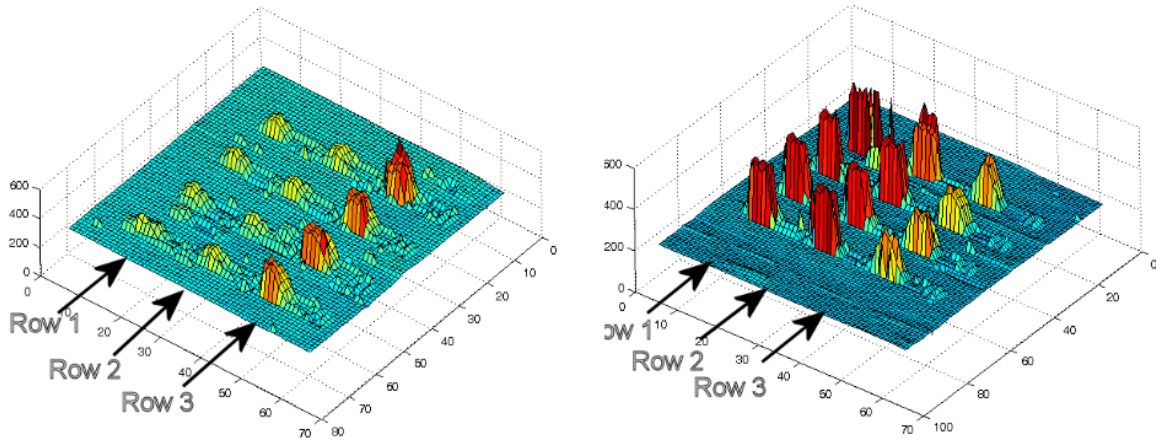


Figure 5: Experimental BSW resonance array scan showing eight spots of Bovine Serum Albumin (BSA) (Rows 1 and 2) and four spots of Immunoglobulin G (IgG) (Row 3) before (left plot) and after (right plot) exposure to anti-BSA.

Another application of the BSW is to achieve slow light [26]. The incident light is temporarily stored on the surface of the 1DPC in the form of BSW before being transmitted which can be extracted with the assistance of a prism at the transmission side. The ability of 1DPC can be utilized to make slow light devices such as optical buffers and switches. Other applications of BSW include focusing and extraction of light mediated by BSW [27], designing platform concep-based flat lens [28], and exciting surface-enhanced Raman scattering [29, 30].

1.3 Bloch Waves and Band Structures

The properties of a 1DPC can be understood from their dispersion relation, which explains the relation between the wavelength and the wavevector of light in the structure [31]. To study the dispersion relation, consider an infinite stack of alternating high and low refractive index materials as shown in Figure 6. The refractive index profile of a unit cell is given by

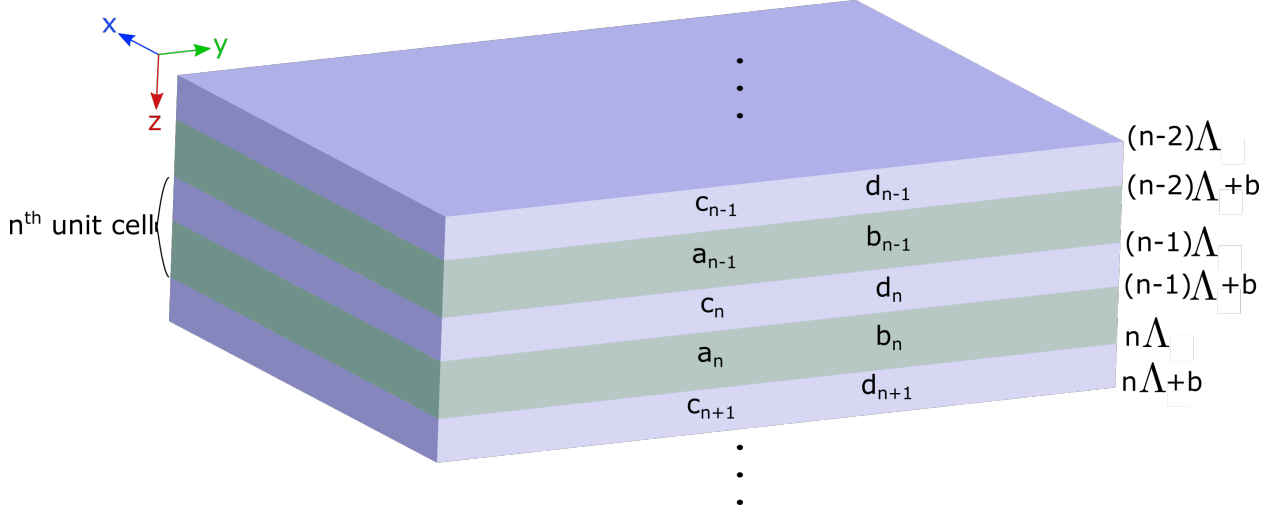


Figure 6: An illustration of infinitely periodic multilayer dielectric structure with plane wave amplitudes associated with the n^{th} unit cell and its neighboring cells.

$$n(z) = \begin{cases} n_2 & 0 < z < b, \\ n_1 & b < z < \Lambda \end{cases} \quad (4)$$

with $n(z + \Lambda) = n(z)$, where the z axis is normal to the interfaces and Λ is the period of the unit cell. The electric field in such structure is of the form

$$\mathbf{E}(z, x) = \mathbf{E}(z)e^{i\beta x}. \quad (5)$$

The electric field within each homogeneous layer, say layer α , is a sum of forward and backward propagating plane waves with amplitudes $a_n^{(\alpha)}$ and $b_n^{(\alpha)}$ respectively and can be written as

$$\mathbf{E}(z, x) = (a_n^{(\alpha)} e^{ik_{\alpha z}(z-n\Lambda)} + b_n^{(\alpha)} e^{-ik_{\alpha z}(z-n\Lambda)}) e^{i\beta x}, \quad (6)$$

with

$$k_{\alpha z} = \sqrt{\{[(\omega/c)n_{\alpha}]^2 - \beta^2\}}, \quad \alpha = 1, 2. \quad (7)$$

Imposing the continuity of \mathbf{E} and $\partial\mathbf{E}/\partial z$ at the interfaces for transverse electric (TE) mode, we get

$$\begin{aligned}
a_{n-1} + b_{n-1} &= e^{-ik_{2z}\Lambda}c_n + e^{ik_{2z}\Lambda}d_n, \\
ik_{1z}(a_{n-1} - b_{n-1}) &= ik_{2z}(e^{-ik_{2z}\Lambda}c_n - e^{ik_{2z}\Lambda}d_n), \\
e^{-ik_{2z}a}c_n + e^{ik_{2z}a}d_n &= e^{-ik_{1z}a}a_n + e^{ik_{1z}a}b_n, \\
ik_{2z}(e^{-ik_{2z}a}c_n - e^{ik_{2z}a}d_n) &= ik_{1z}(e^{-ik_{1z}a}a_n - e^{ik_{1z}a}b_n).
\end{aligned} \tag{8}$$

Eliminating c_n and d_n in Eqn. (8) and doing some algebra, we can put them in a matrix form as

$$\begin{bmatrix} a_{n-1} \\ b_{n-1} \end{bmatrix} = \begin{bmatrix} A & B \\ C & D \end{bmatrix} \begin{bmatrix} a_n \\ b_n \end{bmatrix}. \tag{9}$$

The matrix elements are

$$A = e^{-ik_{1z}a} \left[\cos(k_{2z}b) - \frac{1}{2}i \left(\frac{k_{2z}}{k_{1z}} + \frac{k_{1z}}{k_{2z}} \right) \sin(k_{2z}b) \right], \tag{10}$$

$$B = e^{ik_{1z}a} \left[-\frac{1}{2}i \left(\frac{k_{2z}}{k_{1z}} - \frac{k_{1z}}{k_{2z}} \right) \sin(k_{2z}b) \right], \tag{11}$$

$$C = e^{-ik_{1z}a} \left[\frac{1}{2}i \left(\frac{k_{2z}}{k_{1z}} - \frac{k_{1z}}{k_{2z}} \right) \sin(k_{2z}b) \right], \tag{12}$$

$$D = e^{ik_{1z}a} \left[\cos(k_{2z}b) + \frac{1}{2}i \left(\frac{k_{2z}}{k_{1z}} + \frac{k_{1z}}{k_{2z}} \right) \sin(k_{2z}b) \right]. \tag{13}$$

The matrix in Eqn. (9) relates the amplitudes of the forward and backward wave of a layer in a unit cell to those of the equivalent layer in the next unit cell. The matrix is unimodular, which gives

$$AD - BC = 1. \tag{14}$$

The matrix elements for transverse magnetic (TM) mode are slightly different than that of the TE mode and are given by

$$A = e^{-ik_{1z}a} \left[\cos(k_{2z}b) - \frac{1}{2}i \left(\frac{n_2^2 k_{2z}}{n_1^2 k_{1z}} + \frac{n_1^2 k_{1z}}{n_2^2 k_{2z}} \right) \sin(k_{2z}b) \right], \tag{15}$$

$$B = e^{ik_{1z}a} \left[-\frac{1}{2}i \left(\frac{n_2^2 k_{2z}}{n_1^2 k_{1z}} + \frac{n_1^2 k_{1z}}{n_2^2 k_{2z}} \right) \sin(k_{2z}b) \right], \tag{16}$$

$$C = e^{-ik_{1z}a} \left[\frac{1}{2}i \left(\frac{n_2^2 k_{2z}}{n_1^2 k_{1z}} + \frac{n_1^2 k_{1z}}{n_2^2 k_{2z}} \right) \sin(k_{2z}b) \right], \quad (17)$$

$$D = e^{ik_{1z}a} \left[\cos(k_{2z}b) + \frac{1}{2}i \left(\frac{n_2^2 k_{2z}}{n_1^2 k_{1z}} + \frac{n_1^2 k_{1z}}{n_2^2 k_{2z}} \right) \sin(k_{2z}b) \right]. \quad (18)$$

According to Floquet theorem, electric field propagating in periodic structure is of the form

$$\mathbf{E}_K(z, x) = \mathbf{E}_K(z) e^{iKz} e^{i\beta x}, \quad (19)$$

where

$$\mathbf{E}_K(z + \Lambda) = \mathbf{E}_K(z). \quad (20)$$

The constant K in Eqn. (19) and (20) is known as the Bloch wave number. From Eqn. (6), the periodic condition in Eqn. (20) for the Bloch wave is

$$\begin{bmatrix} a_n \\ b_n \end{bmatrix} = e^{iK\Lambda} \begin{bmatrix} a_{n-1} \\ b_{n-1} \end{bmatrix} \quad (21)$$

and it follows from Eqn. (9) and (21), the Bloch wave satisfies from the following eigenvalue problem

$$\begin{bmatrix} A & B \\ C & D \end{bmatrix} \begin{bmatrix} a_n \\ b_n \end{bmatrix} = e^{-iK\Lambda} \begin{bmatrix} a_n \\ b_n \end{bmatrix}. \quad (22)$$

The term $e^{-iK\Lambda}$ is the eigenvalue of the ABCD matrix and is given by

$$e^{-iK\Lambda} = \frac{1}{2}(A + D) \pm \sqrt{\left\{ \left[\frac{1}{2}(A + D) \right]^2 - 1 \right\}} \quad (23)$$

and its eigenvectors are

$$\begin{bmatrix} a_0 \\ b_0 \end{bmatrix} = \begin{bmatrix} B \\ e^{-K\Lambda} - A \end{bmatrix} \quad (24)$$

times an arbitrary constant. Eqn. (23) gives the dispersion relation between ω , β , and K for the Bloch wave function

$$K(\beta, \omega) = \frac{1}{\Lambda} \cos^{-1} \left[\frac{1}{2}(A + D) \right]. \quad (25)$$

Eqn. (25) is an important equation for understanding Bloch waves and band structures. The regions of β and ω where $|\frac{1}{2}(A + D)| < 1$ corresponds to real K , which gives the propagating Bloch waves. The regions where $|\frac{1}{2}(A + D)| > 1$, $K = m\pi/\Lambda + iK_i$. The Bloch wave number

in this region has an imaginary part K_i , which means the Bloch wave is evanescent. Such regions are the forbidden bands of the periodic structure, where the Bloch surface waves (BSW) can exist. The regime where $|\frac{1}{2}(A + D)| = 1$ gives the band edges. An example of band structures of a 1DPC is shown in Figure 4(b). The green regions are the allowed regions where EM waves can propagate, and the blue regions are the forbidden regions, also known as photonic bandgaps, where no EM waves can propagate. The defect modes however, can exist in such photonic bandgaps. Finally, from Eqn. (6) and (21), the Bloch wave in the n_1 layer of the n^{th} unit cell is given by

$$\mathbf{E}_K(z)e^{-iKz} = [(a_0e^{ik_{1z}(z-n\Lambda)} + b_0e^{-ik_{1z}(z-n\Lambda)})e^{-iK(z-n\Lambda)}]e^{iKz}. \quad (26)$$

The terms a_0 and b_0 in the above equation can be computed from Eqn. (24). Eqn. (26) can then be used iteratively to compute the electric field profile in all the layers of periodic multilayer structures.

CHAPTER 2

NUMERICAL TECHNIQUES

At the present time, numerical techniques have become one of the most important tools in research. The advantages of numerical techniques are many-folds. First, they help us solve complex problems for which analytical solutions cannot be obtained. Second, they assist in studying the effects of changing various problem parameters and achieve optimized solutions. Third, they are comparatively cheaper and less time consuming than building the real structures and then testing and retesting them. In this chapter, we introduce several numerical techniques that are commonly used for studying the properties and uses of 1DPC. We present their mathematical background in brief and also give their pros and cons.

2.1 Transfer Matrix Method using Scattering Matrices

Transfer matrix method (TMM) using scattering matrices [32–34] for 1D multilayer structure described below is a rigorous semi-analytical method. We assume that the 1D multilayer structure is homogeneous in x - y plane, but not in z -direction, i.e., material with different properties are stacked along the z -direction. We further assume that the propagation direction of the plane wave is the positive z -direction. The plane wave has the form

$$\mathbf{E}(\mathbf{r}) = \mathbf{E}_0 e^{-j\mathbf{k}\cdot\mathbf{r}} = \mathbf{E}_0 e^{-jk_x x} e^{-jk_y y} e^{-jk_z z} \quad (27)$$

$$\tilde{\mathbf{H}}(\mathbf{r}) = \tilde{\mathbf{H}}_0 e^{-j\mathbf{k}\cdot\mathbf{r}} = \tilde{\mathbf{H}}_0 e^{-jk_x x} e^{-jk_y y} e^{-jk_z z} \quad (28)$$

We start with Maxwell's equations describing the fields inside a single linear, homogeneous, and isotropic layer of the device which are given below

$$\nabla \times \mathbf{E} = k_0 \mu_r \tilde{\mathbf{H}} \quad (29)$$

$$\nabla \times \tilde{\mathbf{H}} = k_0 \epsilon_r \mathbf{E} \quad (30)$$

The term $\tilde{\mathbf{H}}$ is the normalized magnetic field which is equal to $-j\eta_0 \mathbf{H}$, where $j = \sqrt{-1}$ and η_0 is the impedance of free space, k_0 is the free space wave number and is equal to

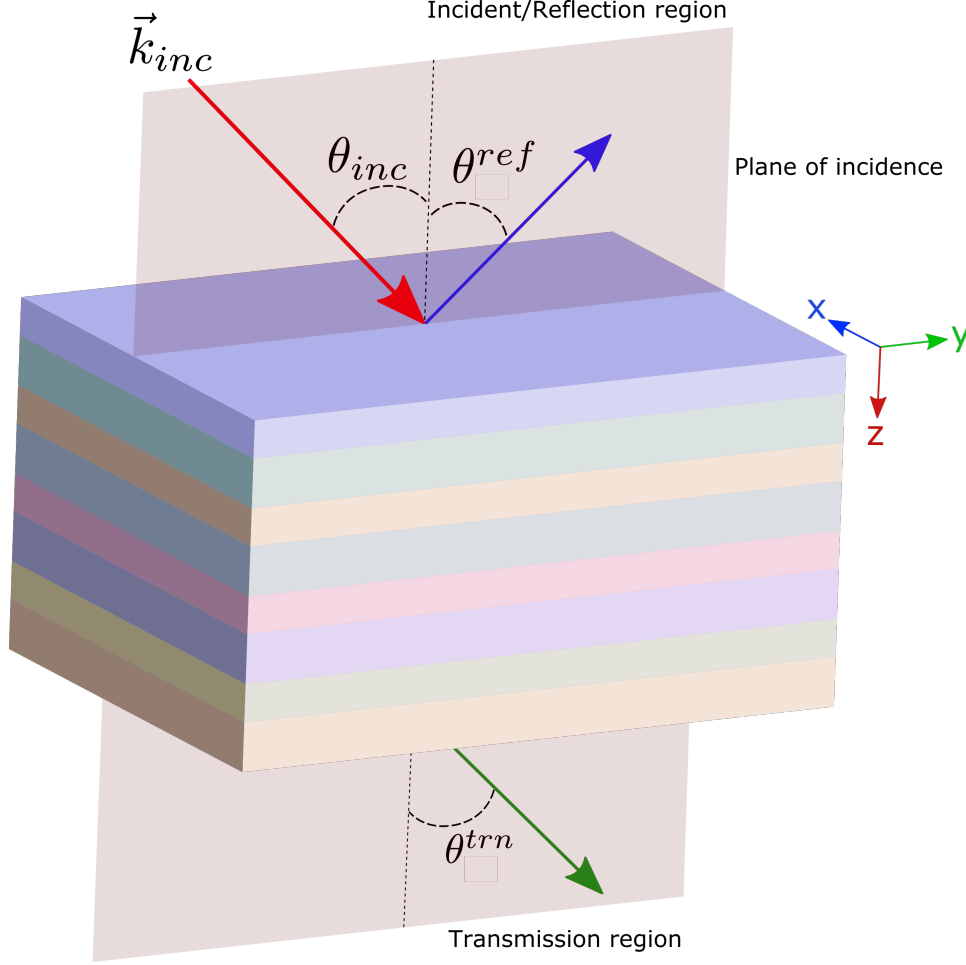


Figure 7: A schematic of a 1D multilayer structure.

$2\pi/\lambda_0$, where λ_0 is the free space wavelength, and μ_r and ϵ_r are relative permeability and permittivity of the material respectively. Eqn. (27) and (28) can be expanded into a set of six coupled partial differential equations as follows

$$\frac{\partial E_z}{\partial y} - \frac{\partial E_y}{\partial z} = k_0 \mu_r \tilde{H}_x \quad (31)$$

$$\frac{\partial E_y}{\partial x} - \frac{\partial E_x}{\partial y} = k_0 \mu_r \tilde{H}_z \quad (32)$$

$$\frac{\partial E_x}{\partial z} - \frac{\partial E_z}{\partial x} = k_0 \mu_r \tilde{H}_y \quad (33)$$

$$\frac{\partial \tilde{H}_z}{\partial y} - \frac{\partial \tilde{H}_y}{\partial z} = k_0 \epsilon_r E_x \quad (34)$$

$$\frac{\partial \tilde{H}_x}{\partial z} - \frac{\partial \tilde{H}_z}{\partial x} = k_0 \epsilon_r E_y \quad (35)$$

$$\frac{\partial \tilde{H}_y}{\partial x} - \frac{\partial \tilde{H}_x}{\partial y} = k_0 \epsilon_r E_z. \quad (36)$$

Since the 1D multilayer structure is homogeneous in the x - y plane, $\frac{\partial}{\partial x}$ and $\frac{\partial}{\partial y}$ in the above equations can be replaced by $-jk_x$ and $-jk_y$ respective. Therefore, the Maxwell's equations reduce to

$$-jk_y E_z - \frac{\partial E_y}{\partial z} = k_0 \mu_r \tilde{H}_x \quad (37)$$

$$\frac{\partial E_x}{\partial z} + jk_x E_z = k_0 \mu_r \tilde{H}_y \quad (38)$$

$$-jk_x E_y + jk_y E_x = k_0 \mu_r \tilde{H}_z \quad (39)$$

$$-jk_y \tilde{H}_z - \frac{\partial \tilde{H}_y}{\partial z} = k_0 \epsilon_r E_x \quad (40)$$

$$\frac{\partial \tilde{H}_x}{\partial z} + jk_x \tilde{H}_z = k_0 \epsilon_r E_y \quad (41)$$

$$-jk_x \tilde{H}_y + jk_y \tilde{H}_x = k_0 \epsilon_r E_z \quad (42)$$

Normalizing z and wave vectors k_x , k_y , and k_z as $z' = k_0 z$, $\tilde{k}_x = k_x/k_0$, $\tilde{k}_y = k_y/k_0$, and $\tilde{k}_z = k_z/k_0$, and finally eliminating longitudinal components E_z and \tilde{H}_z by backsubstitution, we get

$$\frac{\partial E_x}{\partial z'} = \frac{\tilde{k}_x \tilde{k}_y}{\epsilon_r} \tilde{H}_x + \left(\mu_r - \frac{\tilde{k}_x^2}{\epsilon_r} \right) \tilde{H}_y \quad (43)$$

$$\frac{\partial E_y}{\partial z'} = \left(\frac{\tilde{k}_y^2}{\epsilon_r} - \mu_r \right) \tilde{H}_x - \frac{\tilde{k}_x \tilde{k}_y}{\epsilon_r} \tilde{H}_y \quad (44)$$

$$\frac{\partial \tilde{H}_y}{\partial z'} = \frac{\tilde{k}_x \tilde{k}_y}{\mu_r} E_x + \left(\epsilon_r - \frac{\tilde{k}_x^2}{\mu_r} \right) E_y \quad (45)$$

$$\frac{\partial \tilde{H}_x}{\partial z'} = \left(\frac{\tilde{k}_y^2}{\mu_r} - \epsilon_r \right) E_x - \frac{\tilde{k}_x \tilde{k}_y}{\mu_r} E_y \quad (46)$$

These equations can be compactly written in matrix forms as follows

$$\frac{d}{dz'} \begin{bmatrix} E_x \\ E_y \end{bmatrix} = \mathbf{P} \begin{bmatrix} \tilde{H}_x \\ \tilde{H}_y \end{bmatrix} \quad (47)$$

$$\frac{d}{dz'} \begin{bmatrix} \tilde{H}_x \\ \tilde{H}_y \end{bmatrix} = \mathbf{Q} \begin{bmatrix} E_x \\ E_y \end{bmatrix}, \quad (48)$$

where

$$\mathbf{P} = \frac{1}{\epsilon_r} \begin{bmatrix} \tilde{k}_x \tilde{k}_y & \mu_r \epsilon_r - \tilde{k}_x^2 \\ \tilde{k}_y^2 - \mu_r \epsilon_r & -\tilde{k}_x \tilde{k}_y \end{bmatrix} \quad (49)$$

$$\mathbf{Q} = \frac{1}{\mu_r} \begin{bmatrix} \tilde{k}_x \tilde{k}_y & \mu_r \epsilon_r - \tilde{k}_x^2 \\ \tilde{k}_y^2 - \mu_r \epsilon_r & -\tilde{k}_x \tilde{k}_y \end{bmatrix} \quad (50)$$

Taking the derivative of eqn. (47) w.r.t. z' and then substituting eqn. (48) in the result, we get

$$\frac{d^2}{dz'^2} \begin{bmatrix} E_x \\ E_y \end{bmatrix} = \mathbf{\Omega}^2 \begin{bmatrix} E_x \\ E_y \end{bmatrix}, \quad (51)$$

where $\mathbf{\Omega}^2 = \mathbf{PQ}$. Eqn. (51) is the second order wave equation in matrix form. It has a general solution of the form

$$\begin{bmatrix} E_x(z') \\ E_y(z') \end{bmatrix} = e^{-\mathbf{\Omega}z'} \mathbf{a}^+ + e^{\mathbf{\Omega}z'} \mathbf{a}^-. \quad (52)$$

\mathbf{a}^+ , and \mathbf{a}^- are column vectors of proportionality constants for forward and backward waves respectively. The terms $e^{-\mathbf{\Omega}z'}$ and $e^{\mathbf{\Omega}z'}$ have a matrix as their exponents. These matrix exponentials can be computed using the eigen-vectors and eigen-values of the matrix $\mathbf{\Omega}$. Letting \mathbf{W} and λ^2 as the eigen-vector and eigen-value matrix of $\mathbf{\Omega}^2$, we can compute the matrix exponentials as

$$e^{-\mathbf{\Omega}z'} = \mathbf{W} e^{-\lambda z'} \mathbf{W}^{-1} \quad (53)$$

$$e^{\mathbf{\Omega}z'} = \mathbf{W} e^{\lambda z'} \mathbf{W}^{-1}, \quad (54)$$

where $e^{\pm \lambda z'} = \text{diag}(e^{\pm \lambda_1^2 z'}, e^{\pm \lambda_2^2 z'}, \dots, e^{\pm \lambda_N^2 z'})$. Therefore, the solution can be written as

$$\begin{bmatrix} E_x(z') \\ E_y(z') \end{bmatrix} = \mathbf{W} e^{-\lambda z'} \mathbf{W}^{-1} \mathbf{a}^+ + \mathbf{W} e^{\lambda z'} \mathbf{W}^{-1} \mathbf{a}^-. \quad (55)$$

Finally, letting $\mathbf{W}^{-1} \mathbf{a}^+ \equiv \mathbf{c}^+$ and $\mathbf{W}^{-1} \mathbf{a}^- \equiv \mathbf{c}^-$, which are column vectors of amplitude coefficients of the eigen-modes in the forward and backward directions respectively, we can rewrite eqn. (55) as

$$\begin{bmatrix} E_x(z') \\ E_y(z') \end{bmatrix} = \mathbf{W} e^{-\lambda z'} \mathbf{c}^+ + \mathbf{W} e^{\lambda z'} \mathbf{c}^- \quad (56)$$

The matrix $\mathbf{W} = \begin{bmatrix} 1 & 0 \\ 0 & 1 \end{bmatrix} = I$ and $e^{\pm\lambda z'} = \begin{bmatrix} e^{\pm j\tilde{k}_z z'} & 0 \\ 0 & e^{\pm j\tilde{k}_z z'} \end{bmatrix}$. The magnetic field has a similar solution given below

$$\begin{bmatrix} \tilde{H}_x(z') \\ \tilde{H}_y(z') \end{bmatrix} = -\mathbf{V}e^{-\lambda z'} \mathbf{c}^+ + \mathbf{V}e^{\lambda z'} \mathbf{c}^- \quad (57)$$

To compute \mathbf{V} , eqn. (48) is differentiated w.r.t. z' .

$$\frac{d}{dz'} \begin{bmatrix} \tilde{H}_x(z') \\ \tilde{H}_y(z') \end{bmatrix} = \mathbf{V}\lambda e^{-\lambda z'} \mathbf{c}^+ + \mathbf{V}\lambda e^{\lambda z'} \mathbf{c}^- \quad (58)$$

Combining eqn. (48) and (56) gives $\mathbf{V} = \mathbf{Q}\mathbf{W}\lambda^{-1}$. Combining the solutions of electric (eqn. (56)) and magnetic (eqn. (57)) fields into one matrix, we get,

$$\Psi(z') = \begin{bmatrix} E_x(z') \\ E_y(z') \\ \tilde{H}_x(z') \\ \tilde{H}_y(z') \end{bmatrix} = \begin{bmatrix} \mathbf{W} & \mathbf{W} \\ -\mathbf{V} & \mathbf{V} \end{bmatrix} \begin{bmatrix} e^{-\lambda z'} & \mathbf{0} \\ \mathbf{0} & e^{\lambda z'} \end{bmatrix} \begin{bmatrix} \mathbf{c}^+ \\ \mathbf{c}^- \end{bmatrix} \quad (59)$$

Eqn. (59) represents electric and magnetic field in a layer of linear, homogeneous, and isotropic material.

2.1.1 Scattering Matrix for a Layer

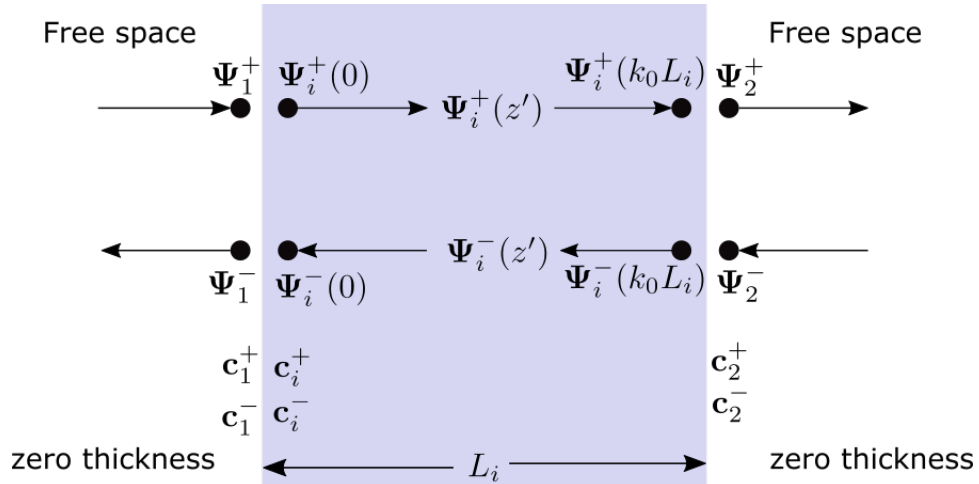


Figure 8: Field representations in the i^{th} layer of a 1D multilayer.

A 1D multilayer device has a stack of multiple layers of different material. Thus, for a

certain i^{th} layer in such a device, the solutions can be represented as

$$\Psi_i(z'_i) = \begin{bmatrix} E_{x,i}(z'_i) \\ E_{y,i}(z'_i) \\ \tilde{H}_{x,i}(z'_i) \\ \tilde{H}_{y,i}(z'_i) \end{bmatrix} = \begin{bmatrix} \mathbf{W}_i & \mathbf{W}_i \\ -\mathbf{V}_i & \mathbf{V}_i \end{bmatrix} \begin{bmatrix} e^{-\lambda_i z'_i} & \mathbf{0} \\ \mathbf{0} & e^{\lambda_i z'_i} \end{bmatrix} \begin{bmatrix} \mathbf{c}_i^+ \\ \mathbf{c}_i^- \end{bmatrix} \quad (60)$$

Each layer has two interfaces with corresponding boundary conditions. Here, we considering each layer separately; thus, medium 1 (left region) and medium 2 (right region) do not strictly need to be layers of the 1D device in consideration. In fact, for the sake of numerical efficiency, we let both medium 1 and 2 to be free space of zero thicknesses. The boundary condition at the first (left) interface is

$$\Psi_1 = \Psi_i(0) \quad (61)$$

$$\begin{bmatrix} \mathbf{W}_1 & \mathbf{W}_1 \\ -\mathbf{V}_1 & \mathbf{V}_1 \end{bmatrix} \begin{bmatrix} \mathbf{c}_1^+ \\ \mathbf{c}_1^- \end{bmatrix} = \begin{bmatrix} \mathbf{W}_i & \mathbf{W}_i \\ -\mathbf{V}_i & \mathbf{V}_i \end{bmatrix} \begin{bmatrix} \mathbf{c}_i^+ \\ \mathbf{c}_i^- \end{bmatrix} \quad (62)$$

The boundary condition at the second (right) interface is

$$\Psi_i(k_0 L_i) = \Psi_2 \quad (63)$$

$$\begin{bmatrix} \mathbf{W}_i & \mathbf{W}_i \\ -\mathbf{V}_i & \mathbf{V}_i \end{bmatrix} \begin{bmatrix} e^{-\lambda_i k_0 L_i} & \mathbf{0} \\ \mathbf{0} & e^{\lambda_i k_0 L_i} \end{bmatrix} \begin{bmatrix} \mathbf{c}_i^+ \\ \mathbf{c}_i^- \end{bmatrix} = \begin{bmatrix} \mathbf{W}_2 & \mathbf{W}_2 \\ -\mathbf{V}_2 & \mathbf{V}_2 \end{bmatrix} \begin{bmatrix} \mathbf{c}_2^+ \\ \mathbf{c}_2^- \end{bmatrix} \quad (64)$$

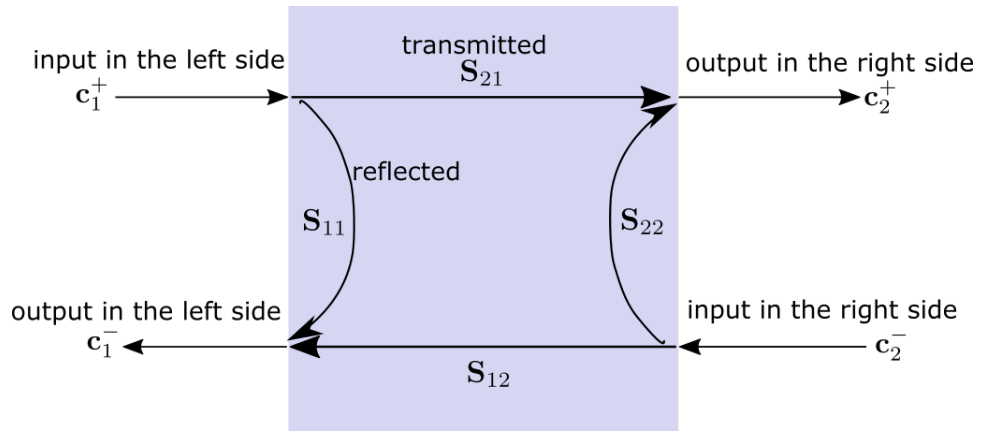


Figure 9: Representation of the scattering matrix of a single layer.

After some manipulations of eqn. (62) and (64), we can reduce them to a system of the following form

$$\begin{bmatrix} \mathbf{c}_1^- \\ \mathbf{c}_2^+ \end{bmatrix} = \mathbf{S}^{(i)} \begin{bmatrix} \mathbf{c}_1^+ \\ \mathbf{c}_2^- \end{bmatrix}, \quad (65)$$

where

$$\mathbf{S}^{(i)} = \begin{bmatrix} \mathbf{S}_{11}^{(i)} & \mathbf{S}_{12}^{(i)} \\ \mathbf{S}_{21}^{(i)} & \mathbf{S}_{22}^{(i)} \end{bmatrix}. \quad (66)$$

The element of matrix $\mathbf{S}^{(i)}$ are calculated as

$$\mathbf{S}_{11}^{(i)} = (\mathbf{A}_i - \mathbf{X}_i \mathbf{B}_i \mathbf{A}_i^{-1} \mathbf{X}_i \mathbf{B}_i)^{-1} (\mathbf{X}_i \mathbf{B}_i \mathbf{A}_i^{-1} \mathbf{X}_i \mathbf{A}_i - \mathbf{B}_i) \quad (67)$$

$$\mathbf{S}_{12}^{(i)} = (\mathbf{A}_i - \mathbf{X}_i \mathbf{B}_i \mathbf{A}_i^{-1} \mathbf{X}_i \mathbf{B}_i)^{-1} \mathbf{X}_i (\mathbf{A}_i - \mathbf{B}_i \mathbf{A}_i^{-1} \mathbf{B}_i) \quad (68)$$

$$\mathbf{S}_{21}^{(i)} = \mathbf{S}_{12}^{(i)} \quad (69)$$

$$\mathbf{S}_{22}^{(i)} = \mathbf{S}_{11}^{(i)} \quad (70)$$

The matrices \mathbf{A}_i , \mathbf{B}_i , and \mathbf{X}_i are computed as

$$\mathbf{A}_i = \mathbf{W}_i^{-1} \mathbf{W}_0 + \mathbf{V}_i^{-1} \mathbf{V}_0 \quad (71)$$

$$\mathbf{B}_i = \mathbf{W}_i^{-1} \mathbf{W}_0 - \mathbf{V}_i^{-1} \mathbf{V}_0 \quad (72)$$

$$\mathbf{X}_i = e^{-\lambda_i k_0 L_i}. \quad (73)$$

The matrix $\mathbf{S}^{(i)}$ is the **scattering matrix** of the i^{th} layer. It relates the input field to the output field. The elements $\mathbf{S}_{11}^{(i)}$, and $\mathbf{S}_{21}^{(i)}$ give reflection and transmission coefficients respectively. Because each layer is surrounded by free space in our formulation, the scattering matrices are symmetric. Thus only two of the matrix components have to be calculated for each layer.

2.1.2 Redheffer Star Product

In order to model a device with multiple layers, we need to combine multiple scattering matrices into a single scattering matrix. However, the scattering matrices cannot be combined directly by applying matrix multiplication. Also, the combined scattering matrix is not symmetric as the scattering matrix for a single layer so it becomes necessary to compute and store all four components of the combined scattering matrix. Two scattering matrices

can be combined using the Redheffer star product [32, 35]. The Redheffer star product of two scattering matrices $\mathbf{S}^{(A)} = \begin{bmatrix} \mathbf{S}_{11}^{(A)} & \mathbf{S}_{12}^{(A)} \\ \mathbf{S}_{21}^{(A)} & \mathbf{S}_{22}^{(A)} \end{bmatrix}$ and $\mathbf{S}^{(B)} = \begin{bmatrix} \mathbf{S}_{11}^{(B)} & \mathbf{S}_{12}^{(B)} \\ \mathbf{S}_{21}^{(B)} & \mathbf{S}_{22}^{(B)} \end{bmatrix}$ is defined as

$$\mathbf{S}^{(AB)} = \begin{bmatrix} \mathbf{S}_{11}^{(AB)} & \mathbf{S}_{12}^{(AB)} \\ \mathbf{S}_{21}^{(AB)} & \mathbf{S}_{22}^{(AB)} \end{bmatrix}, \quad (74)$$

where

$$\mathbf{S}_{11}^{(AB)} = \mathbf{S}_{11}^{(A)} + \mathbf{S}_{12}^{(A)} [\mathbf{I} - \mathbf{S}_{12}^{(B)} \mathbf{S}_{22}^{(A)}]^{-1} \mathbf{S}_{11}^{(B)} \mathbf{S}_{21}^{(A)} \quad (75)$$

$$\mathbf{S}_{12}^{(AB)} = \mathbf{S}_{12}^{(A)} [\mathbf{I} - \mathbf{S}_{12}^{(B)} \mathbf{S}_{22}^{(A)}]^{-1} \mathbf{S}_{12}^{(B)} \quad (76)$$

$$\mathbf{S}_{21}^{(AB)} = \mathbf{S}_{21}^{(B)} [\mathbf{I} - \mathbf{S}_{22}^{(A)} \mathbf{S}_{11}^{(B)}]^{-1} \mathbf{S}_{21}^{(A)} \quad (77)$$

$$\mathbf{S}_{22}^{(AB)} = \mathbf{S}_{22}^{(B)} + \mathbf{S}_{21}^{(B)} [\mathbf{I} - \mathbf{S}_{22}^{(A)} \mathbf{S}_{11}^{(B)}]^{-1} \mathbf{S}_{22}^{(A)} \mathbf{S}_{12}^{(B)} \quad (78)$$

2.1.3 Global Scattering Matrix

The scattering matrix of a 1D multilayer with N layers can be computed by taking Redheffer star product of the scattering matrices of each layer.

$$\mathbf{S}^{(Device)} = \mathbf{S}^{(1)} \otimes \mathbf{S}^{(2)} \otimes \dots \otimes \mathbf{S}^{(N-1)} \otimes \mathbf{S}^{(N)} \quad (79)$$

The multilayer device is surrounded by the reflection region and transmission region at its two ends. It is connected to these external materials by ‘‘connection’’ scattering matrices that have zero-thicknesses. The global scattering matrix finally combines all the scattering matrices into a single matrix as

$$\mathbf{S}^{(Global)} = \mathbf{S}^{(Ref)} \otimes \mathbf{S}^{(Device)} \otimes \mathbf{S}^{(Trn)} \quad (80)$$

The matrices $\mathbf{S}^{(Ref)}$ and $\mathbf{S}^{(Trn)}$ are the reflection and transmission region scattering matrices.

$$\mathbf{S}^{(Ref)} = \begin{bmatrix} \mathbf{S}_{11}^{(Ref)} & \mathbf{S}_{12}^{(Ref)} \\ \mathbf{S}_{21}^{(Ref)} & \mathbf{S}_{22}^{(Ref)} \end{bmatrix}, \quad (81)$$

where

$$\mathbf{S}_{11}^{(Ref)} = -\mathbf{A}_{Ref}^{-1} \mathbf{B}_{Ref} \quad (82)$$

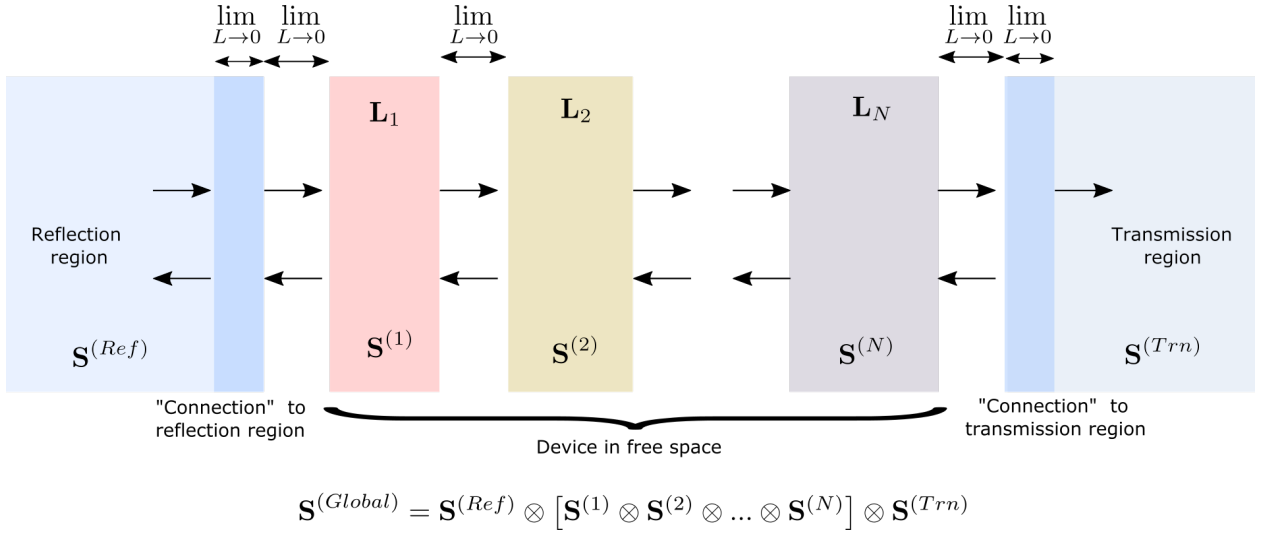


Figure 10: Representation of global scattering matrix.

$$\mathbf{S}_{12}^{(Ref)} = 2\mathbf{A}_{Ref}^{-1} \quad (83)$$

$$\mathbf{S}_{21}^{(Ref)} = 0.5(\mathbf{A}_{Ref} - \mathbf{B}_{Ref}\mathbf{A}_{Ref}^{-1}\mathbf{B}_{Ref}) \quad (84)$$

$$\mathbf{S}_{22}^{(Ref)} = -\mathbf{B}_{Ref}\mathbf{A}_{Ref}^{-1}, \quad (85)$$

with

$$\mathbf{A}_{Ref} = \mathbf{W}_0^{-1}\mathbf{W}_{Ref} + \mathbf{V}_0^{-1}\mathbf{V}_{Ref} \quad (86)$$

$$\mathbf{B}_{Ref} = \mathbf{W}_0^{-1}\mathbf{W}_{Ref} - \mathbf{V}_0^{-1}\mathbf{V}_{Ref} \quad (87)$$

And

$$\mathbf{S}^{(Trn)} = \begin{bmatrix} \mathbf{S}_{11}^{(Trn)} & \mathbf{S}_{12}^{(Trn)} \\ \mathbf{S}_{21}^{(Trn)} & \mathbf{S}_{22}^{(Trn)} \end{bmatrix}, \quad (88)$$

where

$$\mathbf{S}_{11}^{(Trn)} = -\mathbf{B}_{Trn}\mathbf{A}_{Trn}^{-1} \quad (89)$$

$$\mathbf{S}_{12}^{(Trn)} = 0.5(\mathbf{A}_{Trn} - \mathbf{B}_{Trn}\mathbf{A}_{Trn}^{-1}\mathbf{B}_{Trn}) \quad (90)$$

$$\mathbf{S}_{21}^{(Trn)} = 2\mathbf{A}_{Trn}^{-1} \quad (91)$$

$$\mathbf{S}_{22}^{(Trn)} = -\mathbf{A}_{Trn}^{-1}\mathbf{B}_{Trn}, \quad (92)$$

with

$$\mathbf{A}_{Trn} = \mathbf{W}_0^{-1} \mathbf{W}_{Trn} + \mathbf{V}_0^{-1} \mathbf{V}_{Trn} \quad (93)$$

$$\mathbf{B}_{Trn} = \mathbf{W}_0^{-1} \mathbf{W}_{Trn} - \mathbf{V}_0^{-1} \mathbf{V}_{Trn}. \quad (94)$$

2.1.4 Calculating Transmitted and Reflected Electric Field

The global scattering matrix connects the input from the reflection region to the output at the transmission region

$$\begin{bmatrix} \mathbf{c}_{Ref} \\ \mathbf{c}_{Trn} \end{bmatrix} = \begin{bmatrix} \mathbf{S}_{11}^{(Global)} & \mathbf{S}_{12}^{(Global)} \\ \mathbf{S}_{21}^{(Global)} & \mathbf{S}_{22}^{(Global)} \end{bmatrix} \begin{bmatrix} \mathbf{c}_{inc} \\ \mathbf{0} \end{bmatrix}, \quad (95)$$

where

$$\mathbf{c}_{inc} = \begin{bmatrix} E_{x,inc} \\ E_{y,inc} \end{bmatrix} \quad (96)$$

The terms $E_{x,inc}$ and $E_{y,inc}$ are known quantities. From eqn. (95) we get

$$\mathbf{c}_{Ref} = \mathbf{S}_{11}^{(Global)} \mathbf{c}_{inc} \quad (97)$$

$$\mathbf{c}_{Trn} = \mathbf{S}_{21}^{(Global)} \mathbf{c}_{inc} \quad (98)$$

We can finally compute the reflected and transmitted electric field as

$$\begin{bmatrix} E_x^{Ref} \\ E_y^{Ref} \end{bmatrix} = \mathbf{W}_{Ref} \mathbf{c}_{Ref} = \mathbf{W}_{Ref} \mathbf{S}_{11}^{(Global)} \mathbf{c}_{inc} = \mathbf{W}_{Ref} \mathbf{S}_{11}^{(Global)} \mathbf{W}_{Ref}^{-1} \begin{bmatrix} E_{x,inc} \\ E_{y,inc} \end{bmatrix} \quad (99)$$

$$\begin{bmatrix} E_x^{Trn} \\ E_y^{Trn} \end{bmatrix} = \mathbf{W}_{Trn} \mathbf{c}_{Trn} = \mathbf{W}_{Trn} \mathbf{S}_{21}^{(Global)} \mathbf{c}_{inc} = \mathbf{W}_{Trn} \mathbf{S}_{21}^{(Global)} \mathbf{W}_{Ref}^{-1} \begin{bmatrix} E_{x,inc} \\ E_{y,inc} \end{bmatrix}, \quad (100)$$

and

$$E_z^{Ref} = -\frac{\tilde{k}_x E_x^{Ref} + \tilde{k}_y E_y^{Ref}}{\tilde{k}_z^{Ref}} \quad (101)$$

$$E_z^{Trn} = -\frac{\tilde{k}_x E_x^{Trn} + \tilde{k}_y E_y^{Trn}}{\tilde{k}_z^{Trn}} \quad (102)$$

2.1.5 Calculating Transmittance and Reflectance

With the knowledge of reflected and transmitted electric fields, we can compute the reflectance and transmittance as

$$R = \frac{|\mathbf{E}_{Ref}|^2}{|\mathbf{E}_{inc}|^2}, \quad (103)$$

and

$$T = \frac{|\mathbf{E}_{Trn}|^2}{|\mathbf{E}_{inc}|^2} \Re \left[\frac{\mu_{r,Ref} k_{z,trn}}{\mu_{r,Trn} k_{z,inc}} \right], \quad (104)$$

with

$$|\mathbf{E}|^2 = |E_x|^2 + |E_y|^2 + |E_z|^2. \quad (105)$$

2.2 Rigorous Coupled Wave Analysis

The TMM described in section 2.2 is capable of handling 1D multilayer structures with different material in z-direction, but it cannot be used for structures having variations in x-y plane. For instance, the field distribution and the reflection and transmission responses from a 1D multilayer structure with grating on the top layer (see Figure 11) cannot be calculated with the TMM. Rigorous coupled wave analysis (RCWA) [36–42], as suggested by its name, is a more general formulation of Maxwell's equation for structures with material variation in x-y plane as well. The assumption here is that the medium may be inhomogeneous in x-y plane, but it must be uniform in the z-direction for each layer. The formulation of RCWA presented here is very similar to that of TMM in section 2.2. The main difference is the representation of fields and material properties in the Fourier representation. Once the matrices \mathbf{P} and \mathbf{Q} are obtained, all the remaining steps are exactly the same as in TMM.

We begin the formulation of RCWA starting from eqn. (31)-(36). For RCWA, ϵ_r and μ_r are represented in terms of Fourier transforms along the x and y direction, the z-parameter remains analytical and unchanged.

$$\nabla \times \mathbf{E} = k_0 \mu_r \tilde{\mathbf{H}} \quad (106)$$

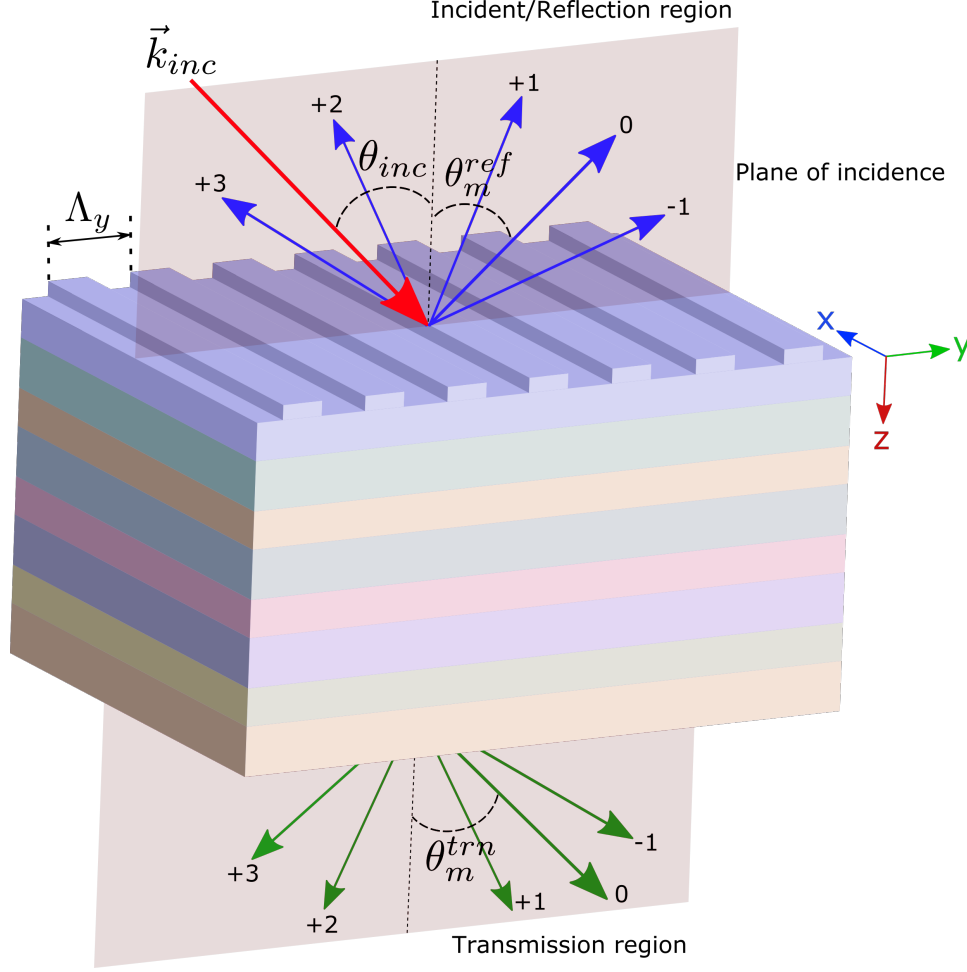


Figure 11: A schematic of a 1D multilayer structure with a grating on the top layer.

$$\nabla \times \tilde{\mathbf{H}} = k_0 \epsilon_r \mathbf{E} \quad (107)$$

The term $\tilde{\mathbf{H}}$ is the normalized magnetic field which is equal to $-j\eta_0 \mathbf{H}$, where $j = \sqrt{-1}$ and η_0 is the impedance of free space, k_0 is the free space wave number and is equal to $2\pi/\lambda_0$, where λ_0 is the free space wavelength, and μ_r and ϵ_r are relative permeability and permittivity of the material respectively. Eqn. (106) and (107) can be expanded into a set of six coupled partial differential equations as follows

$$\frac{\partial E_z}{\partial y} - \frac{\partial E_y}{\partial z} = k_0 \mu_r \tilde{H}_x \quad (108)$$

$$\frac{\partial E_y}{\partial x} - \frac{\partial E_x}{\partial y} = k_0 \mu_r \tilde{H}_z \quad (109)$$

$$\frac{\partial E_x}{\partial z} - \frac{\partial E_z}{\partial x} = k_0 \mu_r \tilde{H}_y \quad (110)$$

$$\frac{\partial \tilde{H}_z}{\partial y} - \frac{\partial \tilde{H}_y}{\partial z} = k_0 \epsilon_r E_x \quad (111)$$

$$\frac{\partial \tilde{H}_x}{\partial z} - \frac{\partial \tilde{H}_z}{\partial x} = k_0 \epsilon_r E_y \quad (112)$$

$$\frac{\partial \tilde{H}_y}{\partial x} - \frac{\partial \tilde{H}_x}{\partial y} = k_0 \epsilon_r E_z. \quad (113)$$

For RCWA, ϵ_r and μ_r are represented in terms of Fourier transforms along the x and y direction, the z -parameter remains analytical and unchanged.

$$\epsilon_r(x, y) = \sum_{m=-\infty}^{\infty} \sum_{n=-\infty}^{\infty} a_{m,n} e^{j\left(\frac{2\pi m x}{\Lambda_x} + \frac{2\pi n y}{\Lambda_y}\right)} \quad (114)$$

$$\mu_r(x, y) = \sum_{m=-\infty}^{\infty} \sum_{n=-\infty}^{\infty} b_{m,n} e^{j\left(\frac{2\pi m x}{\Lambda_x} + \frac{2\pi n y}{\Lambda_y}\right)} \quad (115)$$

The coefficients $a_{m,n}$ and $b_{m,n}$ are given as

$$a_{m,n} = \frac{1}{\Lambda_x \Lambda_y} \int_{-\frac{\Lambda_x}{2}}^{\frac{\Lambda_x}{2}} \int_{-\frac{\Lambda_y}{2}}^{\frac{\Lambda_y}{2}} \epsilon_r(x, y) e^{-j\left(\frac{2\pi m x}{\Lambda_x} + \frac{2\pi n y}{\Lambda_y}\right)} dx dy. \quad (116)$$

The terms Λ_x and Λ_y are the periods in x and y directions respectively.

$$b_{m,n} = \frac{1}{\Lambda_x \Lambda_y} \int_{-\frac{\Lambda_x}{2}}^{\frac{\Lambda_x}{2}} \int_{-\frac{\Lambda_y}{2}}^{\frac{\Lambda_y}{2}} \mu_r(x, y) e^{-j\left(\frac{2\pi m x}{\Lambda_x} + \frac{2\pi n y}{\Lambda_y}\right)} dx dy \quad (117)$$

The Fourier expansion of the fields are

$$E_x(x, y, z) = \sum_{m=-\infty}^{\infty} \sum_{n=-\infty}^{\infty} S_{x,m,n}(z) e^{-j(k_x m x + k_y n y)} \quad (118)$$

$$E_y(x, y, z) = \sum_{m=-\infty}^{\infty} \sum_{n=-\infty}^{\infty} S_{y,m,n}(z) e^{-j(k_x m x + k_y n y)} \quad (119)$$

$$E_z(x, y, z) = \sum_{m=-\infty}^{\infty} \sum_{n=-\infty}^{\infty} S_{z,m,n}(z) e^{-j(k_x m x + k_y n y)} \quad (120)$$

$$H_x(x, y, z) = \sum_{m=-\infty}^{\infty} \sum_{n=-\infty}^{\infty} U_{x,m,n}(z) e^{-j(k_x m x + k_y n y)} \quad (121)$$

$$H_y(x, y, z) = \sum_{m=-\infty}^{\infty} \sum_{n=-\infty}^{\infty} U_{y,m,n}(z) e^{-j(k_x m x + k_y n y)} \quad (122)$$

$$H_z(x, y, z) = \sum_{m=-\infty}^{\infty} \sum_{n=-\infty}^{\infty} U_{z,m,n}(z) e^{-j(k_{x,m}x + k_{y,n}y)}, \quad (123)$$

where

$$k_{x,m} = k_{x,inc} - \frac{2\pi m}{\Lambda_x}, \quad m = -\infty, \dots, -2, -1, 0, 1, 2, \dots, \infty \quad (124)$$

$$k_{y,n} = k_{y,inc} - \frac{2\pi n}{\Lambda_y}, \quad n = -\infty, \dots, -2, -1, 0, 1, 2, \dots, \infty \quad (125)$$

Substituting the field expressions in eqn. (118)-(123), and doing some algebraic manipulations, the Maxwell's equations in real space can be converted to the Maxwell's equations in semi-analytical Fourier space

$$-j\tilde{k}_{y,n}S_{z,m,n}(\tilde{z}) - \frac{d}{d\tilde{z}}S_{y,m,n}(\tilde{z}) = \sum_{q=-\infty}^{\infty} \sum_{r=-\infty}^{\infty} b_{m-q,n-r}U_{x,q,r}(\tilde{z}) \quad (126)$$

$$\frac{d}{d\tilde{z}}S_{x,m,n}(\tilde{z}) + j\tilde{k}_{x,m}S_{z,m,n}(\tilde{z}) = \sum_{q=-\infty}^{\infty} \sum_{r=-\infty}^{\infty} b_{m-q,n-r}U_{y,q,r}(\tilde{z}) \quad (127)$$

$$-j\tilde{k}_{x,m}S_{y,m,n}(\tilde{z}) + jk_{y,m}S_{z,m,n}(\tilde{z}) = \sum_{q=-\infty}^{\infty} \sum_{r=-\infty}^{\infty} b_{m-q,n-r}U_{z,q,r}(\tilde{z}) \quad (128)$$

$$-j\tilde{k}_{y,n}U_{z,m,n}(\tilde{z}) - \frac{d}{d\tilde{z}}U_{y,m,n}(\tilde{z}) = \sum_{q=-\infty}^{\infty} \sum_{r=-\infty}^{\infty} a_{m-q,n-r}S_{x,q,r}(\tilde{z}) \quad (129)$$

$$\frac{d}{d\tilde{z}}U_{x,m,n}(\tilde{z}) + j\tilde{k}_{x,m}U_{z,m,n}(\tilde{z}) = \sum_{q=-\infty}^{\infty} \sum_{r=-\infty}^{\infty} a_{m-q,n-r}S_{y,q,r}(\tilde{z}) \quad (130)$$

$$-j\tilde{k}_{x,m}U_{y,m,n}(\tilde{z}) + jk_{y,m}U_{z,m,n}(\tilde{z}) = \sum_{q=-\infty}^{\infty} \sum_{r=-\infty}^{\infty} a_{m-q,n-r}S_{z,q,r}(\tilde{z}). \quad (131)$$

Expanding each of these equations for every possible combination of m and n and putting them in matrix form, they can be compactly represented as

$$-j\mathbf{K}_y\mathbf{u}_z - \frac{d}{d\tilde{z}}\mathbf{u}_y = \epsilon_r\mathbf{s}_x \quad (132)$$

$$\frac{d}{d\tilde{z}}\mathbf{u}_x + j\mathbf{K}_x\mathbf{u}_z = \epsilon_r\mathbf{s}_y \quad (133)$$

$$\mathbf{K}_x\mathbf{u}_y - \mathbf{K}_y\mathbf{u}_x = j\epsilon_r\mathbf{s}_z \quad (134)$$

$$-j\mathbf{K}_y\mathbf{s}_z - \frac{d}{d\tilde{z}}\mathbf{s}_y = \mu_r\mathbf{u}_x \quad (135)$$

$$\frac{d}{d\tilde{z}}\mathbf{s}_x + j\mathbf{K}_x\mathbf{s}_z = \mu_r\mathbf{u}_y \quad (136)$$

$$\mathbf{K}_x\mathbf{s}_y - \mathbf{K}_y\mathbf{s}_x = j\mu_r\mathbf{u}_z, \quad (137)$$

where

$$\mathbf{u}_x = \begin{bmatrix} U_{x,1,1} \\ U_{x,1,2} \\ \vdots \\ \vdots \\ U_{x,M,N} \end{bmatrix} \quad \mathbf{u}_y = \begin{bmatrix} U_{y,1,1} \\ U_{y,1,2} \\ \vdots \\ \vdots \\ U_{y,M,N} \end{bmatrix} \quad \mathbf{u}_z = \begin{bmatrix} U_{z,1,1} \\ U_{z,1,2} \\ \vdots \\ \vdots \\ U_{z,M,N} \end{bmatrix} \quad \mathbf{s}_x = \begin{bmatrix} S_{x,1,1} \\ S_{x,1,2} \\ \vdots \\ \vdots \\ S_{x,M,N} \end{bmatrix} \quad \mathbf{s}_y = \begin{bmatrix} S_{y,1,1} \\ S_{y,1,2} \\ \vdots \\ \vdots \\ S_{y,M,N} \end{bmatrix} \quad \mathbf{s}_z = \begin{bmatrix} S_{z,1,1} \\ S_{z,1,2} \\ \vdots \\ \vdots \\ S_{z,M,N} \end{bmatrix}$$

$$\mathbf{K}_x = \begin{pmatrix} \tilde{k}_{x,1,1} & & & & \\ & \tilde{k}_{x,1,2} & & & \\ & & \ddots & & \\ & & & \ddots & \\ & 0 & & & \tilde{k}_{x,M,N} \end{pmatrix} \quad \mathbf{K}_y = \begin{pmatrix} \tilde{k}_{y,1,1} & & & & \\ & \tilde{k}_{y,1,2} & & & \\ & & \ddots & & \\ & & & \ddots & \\ & 0 & & & \tilde{k}_{y,M,N} \end{pmatrix}$$

$$\epsilon_r = \begin{bmatrix} \text{Toeplitz Convolution matrix} \end{bmatrix} \quad \mu_r = \begin{bmatrix} \text{Toeplitz Convolution matrix} \end{bmatrix}.$$

Eliminating the longitudinal components \mathbf{s}_z and \mathbf{u}_z by back-substitution and rearranging them, eqn. (132)-(137) can be further reduced down to

$$\frac{d}{d\tilde{z}}\mathbf{u}_x = \mathbf{K}_x\mu_r^{-1}\mathbf{K}_y\mathbf{s}_x + (\epsilon_r - \mathbf{K}_x\mu_r^{-1}\mathbf{K}_x)\mathbf{s}_y \quad (138)$$

$$\frac{d}{d\tilde{z}}\mathbf{u}_y = (\mathbf{K}_y\mu_r^{-1}\mathbf{K}_y - \epsilon_r)\mathbf{s}_x - \mathbf{K}_y\mu_r^{-1}\mathbf{K}_x\mathbf{s}_y \quad (139)$$

$$\frac{d}{d\tilde{z}}\mathbf{s}_x = \mathbf{K}_x\epsilon_r^{-1}\mathbf{K}_y\mathbf{u}_x + (\mu_r - \mathbf{K}_x\epsilon_r^{-1}\mathbf{K}_x)\mathbf{u}_y \quad (140)$$

$$\frac{d}{d\tilde{z}}\mathbf{s}_y = (\mathbf{K}_y\epsilon_r^{-1}\mathbf{K}_y - \mu_r)\mathbf{u}_x - \mathbf{K}_y\epsilon_r^{-1}\mathbf{K}_x\mathbf{u}_y \quad (141)$$

These equations can be compactly written in matrix form as follows

$$\frac{d}{d\tilde{z}} \begin{bmatrix} \mathbf{u}_x \\ \mathbf{u}_y \end{bmatrix} = \mathbf{Q} \begin{bmatrix} \mathbf{s}_x \\ \mathbf{s}_y \end{bmatrix} \quad (142)$$

$$\frac{d}{d\tilde{z}} \begin{bmatrix} \mathbf{s}_x \\ \mathbf{s}_y \end{bmatrix} = \mathbf{P} \begin{bmatrix} \mathbf{u}_x \\ \mathbf{u}_y \end{bmatrix}, \quad (143)$$

where

$$\mathbf{Q} = \begin{bmatrix} \mathbf{K}_x \mu_r^{-1} \mathbf{K}_y & \epsilon_r - \mathbf{K}_x \mu_r^{-1} \mathbf{K}_x \\ \mathbf{K}_y \mu_r^{-1} \mathbf{K}_y - \epsilon_r & -\mathbf{K}_y \mu_r^{-1} \mathbf{K}_x \end{bmatrix} \quad (144)$$

$$\mathbf{P} = \begin{bmatrix} \mathbf{K}_x \epsilon_r^{-1} \mathbf{K}_y & \mu_r - \mathbf{K}_x \epsilon_r^{-1} \mathbf{K}_x \\ \mathbf{K}_y \epsilon_r^{-1} \mathbf{K}_y - \mu_r & -\mathbf{K}_y \epsilon_r^{-1} \mathbf{K}_x \end{bmatrix} \quad (145)$$

Taking the derivative of eqn. (143) w.r.t. z' and then substituting eqn. (142) in the result, we get

$$\frac{d^2}{dz'^2} \begin{bmatrix} \mathbf{s}_x \\ \mathbf{s}_y \end{bmatrix} = \Omega^2 \begin{bmatrix} \mathbf{s}_x \\ \mathbf{s}_y \end{bmatrix}, \quad (146)$$

where $\Omega^2 = \mathbf{PQ}$. Eqn. (146) is the second order wave equation in matrix form. It has a general solution of the form

$$\begin{bmatrix} \mathbf{s}_x(z') \\ \mathbf{s}_y(z') \end{bmatrix} = e^{-\Omega z'} \mathbf{s}^+(0) + e^{\Omega z'} \mathbf{s}^-(0). \quad (147)$$

The terms $\mathbf{s}^+(0)$, and $\mathbf{s}^-(0)$ are the initial values for this differential equation. The \pm superscripts indicate whether they pertain to forward propagating waves (+) or backward propagating waves (-). The terms $e^{-\Omega z'}$ and $e^{\Omega z'}$ have a matrix as their exponents. These matrix exponentials can be computed using the eigen-vectors and eigen-values of the matrix Ω . Letting \mathbf{W} and λ^2 as the eigen-vector and eigen-value matrix of Ω^2 , we can compute the matrix exponentials as

$$e^{-\Omega z'} = \mathbf{W} e^{-\lambda z'} \mathbf{W}^{-1} \quad (148)$$

$$e^{\Omega z'} = \mathbf{W} e^{\lambda z'} \mathbf{W}^{-1}, \quad (149)$$

where $e^{\pm \lambda z'} = \text{diag}(e^{\pm \lambda_1^2 z'}, e^{\pm \lambda_2^2 z'}, \dots, e^{\pm \lambda_N^2 z'})$. Therefore, the solution can be written as

$$\begin{bmatrix} \mathbf{s}_x(z') \\ \mathbf{s}_y(z') \end{bmatrix} = \mathbf{W} e^{-\lambda z'} \mathbf{W}^{-1} \mathbf{s}^+(0) + \mathbf{W} e^{\lambda z'} \mathbf{W}^{-1} \mathbf{s}^-(0). \quad (150)$$

Finally, letting $\mathbf{W}^{-1} \mathbf{s}^+(0) \equiv \mathbf{c}^+$ and $\mathbf{W}^{-1} \mathbf{s}^-(0) \equiv \mathbf{c}^-$, which are column vectors of amplitude coefficients of the eigen-modes in the forward and backward directions respectively, we can rewrite eqn. (150) as

$$\begin{bmatrix} \mathbf{s}_x(z') \\ \mathbf{s}_y(z') \end{bmatrix} = \mathbf{W} e^{-\lambda z'} \mathbf{c}^+ + \mathbf{W} e^{\lambda z'} \mathbf{c}^- \quad (151)$$

The matrix $\mathbf{W} = \begin{bmatrix} 1 & 0 \\ 0 & 1 \end{bmatrix} = I$ and $e^{\pm\lambda z'} = \begin{bmatrix} e^{\pm j\tilde{k}_z z'} & 0 \\ 0 & e^{\pm j\tilde{k}_z z'} \end{bmatrix}$. The magnetic field has a similar solution given below

$$\begin{bmatrix} \mathbf{u}_x(z') \\ \mathbf{u}_y(z') \end{bmatrix} = -\mathbf{V}e^{-\lambda z'} \mathbf{c}^+ + \mathbf{V}e^{\lambda z'} \mathbf{c}^- \quad (152)$$

To compute \mathbf{V} , eqn. (152) is differentiated w.r.t. z' .

$$\frac{d}{dz'} \begin{bmatrix} \mathbf{u}_x(z') \\ \mathbf{u}_y(z') \end{bmatrix} = \mathbf{V}\lambda e^{-\lambda z'} \mathbf{c}^+ + \mathbf{V}\lambda e^{\lambda z'} \mathbf{c}^- \quad (153)$$

Then, substituting eqn. (151) into eqn. (142), and then comparing it to eqn. (153), we get $\mathbf{V} = \mathbf{Q}\mathbf{W}\lambda^{-1}$. Combining the solutions of electric (eqn. (151)) and magnetic (eqn. (152)) fields into one matrix, we get,

$$\Psi(z') = \begin{bmatrix} \mathbf{s}_x(z') \\ \mathbf{s}_y(z') \\ \mathbf{u}_x(z') \\ \mathbf{u}_y(z') \end{bmatrix} = \begin{bmatrix} \mathbf{W} & \mathbf{W} \\ -\mathbf{V} & \mathbf{V} \end{bmatrix} \begin{bmatrix} e^{-\lambda z'} & \mathbf{0} \\ \mathbf{0} & e^{\lambda z'} \end{bmatrix} \begin{bmatrix} \mathbf{c}^+ \\ \mathbf{c}^- \end{bmatrix} \quad (154)$$

Eqn. (154) represents electric and magnetic field in a layer of linear, homogeneous, and isotropic material.

2.2.1 Scattering Matrix for a Layer

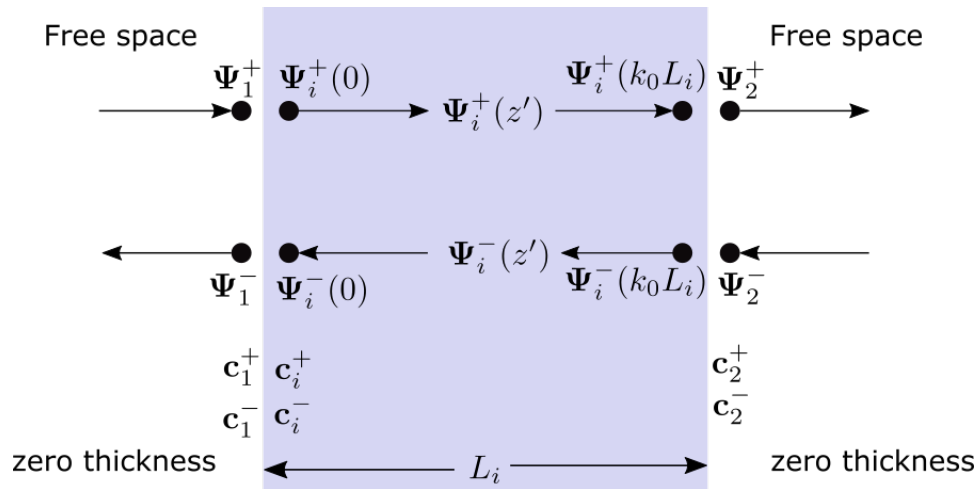


Figure 12: Field representations in the i^{th} layer of a 1D multilayer.

A 1D multilayer device has a stack of multiple layers of different material. Thus, for a certain i^{th} layer in such a device, the solutions can be represented as

$$\Psi_i(z'_i) = \begin{bmatrix} \mathbf{s}_{x,i}(z'_i) \\ \mathbf{s}_{y,i}(z'_i) \\ \mathbf{u}_{x,i}(z'_i) \\ \mathbf{u}_{y,i}(z'_i) \end{bmatrix} = \begin{bmatrix} \mathbf{W}_i & \mathbf{W}_i \\ -\mathbf{V}_i & \mathbf{V}_i \end{bmatrix} \begin{bmatrix} e^{-\lambda_i z'_i} & \mathbf{0} \\ \mathbf{0} & e^{\lambda_i z'_i} \end{bmatrix} \begin{bmatrix} \mathbf{c}_i^+ \\ \mathbf{c}_i^- \end{bmatrix} \quad (155)$$

Each layer has two interfaces with corresponding boundary conditions. Here, we considering each layer separately; thus, medium 1 (left region) and medium 2 (right region) do not strictly need to be layers of the 1D device in consideration. In fact, for the sake of numerical efficiency, we let both medium 1 and 2 to be free space of zero thicknesses. The boundary condition at the first (left) interface is

$$\Psi_1 = \Psi_i(0) \quad (156)$$

$$\begin{bmatrix} \mathbf{W}_1 & \mathbf{W}_1 \\ -\mathbf{V}_1 & \mathbf{V}_1 \end{bmatrix} \begin{bmatrix} \mathbf{c}_1^+ \\ \mathbf{c}_1^- \end{bmatrix} = \begin{bmatrix} \mathbf{W}_i & \mathbf{W}_i \\ -\mathbf{V}_i & \mathbf{V}_i \end{bmatrix} \begin{bmatrix} \mathbf{c}_i^+ \\ \mathbf{c}_i^- \end{bmatrix} \quad (157)$$

The boundary condition at the second (right) interface is

$$\Psi_i(k_0 L_i) = \Psi_2 \quad (158)$$

$$\begin{bmatrix} \mathbf{W}_i & \mathbf{W}_i \\ -\mathbf{V}_i & \mathbf{V}_i \end{bmatrix} \begin{bmatrix} e^{-\lambda_i k_0 L_i} & \mathbf{0} \\ \mathbf{0} & e^{\lambda_i k_0 L_i} \end{bmatrix} \begin{bmatrix} \mathbf{c}_i^+ \\ \mathbf{c}_i^- \end{bmatrix} = \begin{bmatrix} \mathbf{W}_2 & \mathbf{W}_2 \\ -\mathbf{V}_2 & \mathbf{V}_2 \end{bmatrix} \begin{bmatrix} \mathbf{c}_2^+ \\ \mathbf{c}_2^- \end{bmatrix} \quad (159)$$

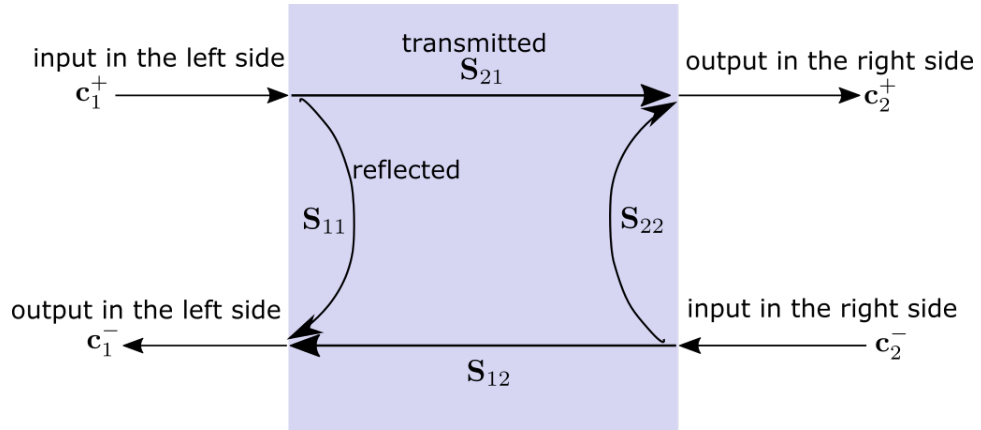


Figure 13: Representation of the scattering matrix of a single layer.

After some manipulations of eqn. (157) and (159), we can reduce them to a system of the following form

$$\begin{bmatrix} \mathbf{c}_1^- \\ \mathbf{c}_2^+ \end{bmatrix} = \mathbf{S}^{(i)} \begin{bmatrix} \mathbf{c}_1^+ \\ \mathbf{c}_2^- \end{bmatrix}, \quad (160)$$

where

$$\mathbf{S}^{(i)} = \begin{bmatrix} \mathbf{S}_{11}^{(i)} & \mathbf{S}_{12}^{(i)} \\ \mathbf{S}_{21}^{(i)} & \mathbf{S}_{22}^{(i)} \end{bmatrix}. \quad (161)$$

The element of matrix $\mathbf{S}^{(i)}$ are calculated as

$$\mathbf{S}_{11}^{(i)} = (\mathbf{A}_i - \mathbf{X}_i \mathbf{B}_i \mathbf{A}_i^{-1} \mathbf{X}_i \mathbf{B}_i)^{-1} (\mathbf{X}_i \mathbf{B}_i \mathbf{A}_i^{-1} \mathbf{X}_i \mathbf{A}_i - \mathbf{B}_i) \quad (162)$$

$$\mathbf{S}_{12}^{(i)} = (\mathbf{A}_i - \mathbf{X}_i \mathbf{B}_i \mathbf{A}_i^{-1} \mathbf{X}_i \mathbf{B}_i)^{-1} \mathbf{X}_i (\mathbf{A}_i - \mathbf{B}_i \mathbf{A}_i^{-1} \mathbf{B}_i) \quad (163)$$

$$\mathbf{S}_{21}^{(i)} = \mathbf{S}_{12}^{(i)} \quad (164)$$

$$\mathbf{S}_{22}^{(i)} = \mathbf{S}_{11}^{(i)} \quad (165)$$

The matrices \mathbf{A}_i , \mathbf{B}_i , and \mathbf{X}_i are computed as

$$\mathbf{A}_i = \mathbf{W}_i^{-1} \mathbf{W}_0 + \mathbf{V}_i^{-1} \mathbf{V}_0 \quad (166)$$

$$\mathbf{B}_i = \mathbf{W}_i^{-1} \mathbf{W}_0 - \mathbf{V}_i^{-1} \mathbf{V}_0 \quad (167)$$

$$\mathbf{X}_i = e^{-\lambda_i k_0 L_i}. \quad (168)$$

The matrix $\mathbf{S}^{(i)}$ is the **scattering matrix** of the i^{th} layer. It relates the input field to the output field. The elements $\mathbf{S}_{11}^{(i)}$, and $\mathbf{S}_{21}^{(i)}$ give reflection and transmission coefficients respectively. Because each layer is surrounded by free space in our formulation, the scattering matrices are symmetric. Thus only two of the matrix components have to be calculated for each layer.

2.2.2 Redheffer Star Product

In order to model a device with multiple layers, we need to combine multiple scattering matrices into a single scattering matrix. However, the scattering matrices cannot be combined directly by applying matrix multiplication. Also, the combined scattering matrix is

not symmetric as the scattering matrix for a single layer so it becomes necessary to compute and store all four components of the combined scattering matrix. Two scattering matrices can be combined using the Redheffer star product [32, 35]. The Redheffer star product of two scattering matrices $\mathbf{S}^{(A)} = \begin{bmatrix} \mathbf{S}_{11}^{(A)} & \mathbf{S}_{12}^{(A)} \\ \mathbf{S}_{21}^{(A)} & \mathbf{S}_{22}^{(A)} \end{bmatrix}$ and $\mathbf{S}^{(B)} = \begin{bmatrix} \mathbf{S}_{11}^{(B)} & \mathbf{S}_{12}^{(B)} \\ \mathbf{S}_{21}^{(B)} & \mathbf{S}_{22}^{(B)} \end{bmatrix}$ is defined as

$$\mathbf{S}^{(AB)} = \begin{bmatrix} \mathbf{S}_{11}^{(AB)} & \mathbf{S}_{12}^{(AB)} \\ \mathbf{S}_{21}^{(AB)} & \mathbf{S}_{22}^{(AB)} \end{bmatrix}, \quad (169)$$

where

$$\mathbf{S}_{11}^{(AB)} = \mathbf{S}_{11}^{(A)} + \mathbf{S}_{12}^{(A)} [\mathbf{I} - \mathbf{S}_{12}^{(B)} \mathbf{S}_{22}^{(A)}]^{-1} \mathbf{S}_{11}^{(B)} \mathbf{S}_{21}^{(A)} \quad (170)$$

$$\mathbf{S}_{12}^{(AB)} = \mathbf{S}_{12}^{(A)} [\mathbf{I} - \mathbf{S}_{12}^{(B)} \mathbf{S}_{22}^{(A)}]^{-1} \mathbf{S}_{12}^{(B)} \quad (171)$$

$$\mathbf{S}_{21}^{(AB)} = \mathbf{S}_{21}^{(B)} [\mathbf{I} - \mathbf{S}_{22}^{(A)} \mathbf{S}_{11}^{(B)}]^{-1} \mathbf{S}_{21}^{(A)} \quad (172)$$

$$\mathbf{S}_{22}^{(AB)} = \mathbf{S}_{22}^{(B)} + \mathbf{S}_{21}^{(B)} [\mathbf{I} - \mathbf{S}_{22}^{(A)} \mathbf{S}_{11}^{(B)}]^{-1} \mathbf{S}_{22}^{(A)} \mathbf{S}_{12}^{(B)} \quad (173)$$

2.2.3 Global Scattering Matrix

The scattering matrix of a 1D multilayer with N layers can be computed by taking Redheffer star product of the scattering matrices of each layer.

$$\mathbf{S}^{(Device)} = \mathbf{S}^{(1)} \otimes \mathbf{S}^{(2)} \otimes \dots \otimes \mathbf{S}^{(N-1)} \otimes \mathbf{S}^{(N)} \quad (174)$$

The multilayer device is surrounded by the reflection region and transmission region at its two ends. It is connected to these external materials by “connection” scattering matrices that have zero-thicknesses. The global scattering matrix finally combines all the scattering matrices into a single matrix as

$$\mathbf{S}^{(Global)} = \mathbf{S}^{(Ref)} \otimes \mathbf{S}^{(Device)} \otimes \mathbf{S}^{(Trn)} \quad (175)$$

The matrices $\mathbf{S}^{(Ref)}$ and $\mathbf{S}^{(Trn)}$ are the reflection and transmission region scattering matrices.

$$\mathbf{S}^{(Ref)} = \begin{bmatrix} \mathbf{S}_{11}^{(Ref)} & \mathbf{S}_{12}^{(Ref)} \\ \mathbf{S}_{21}^{(Ref)} & \mathbf{S}_{22}^{(Ref)} \end{bmatrix}, \quad (176)$$

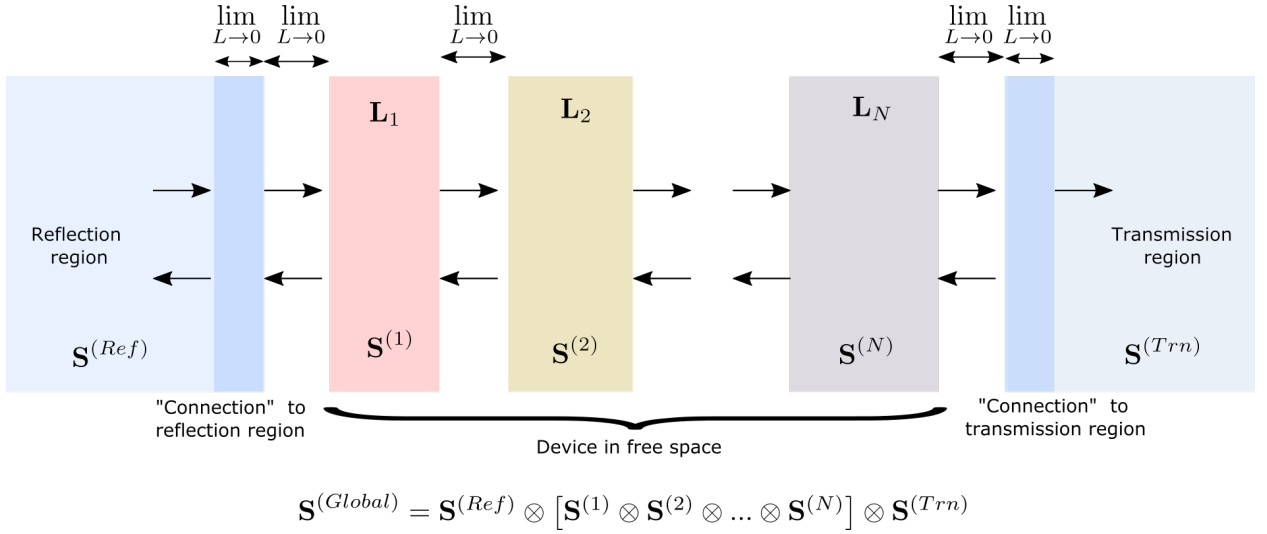


Figure 14: Representation of global scattering matrix.

where

$$\mathbf{S}_{11}^{(Ref)} = -\mathbf{A}_{Ref}^{-1} \mathbf{B}_{Ref} \quad (177)$$

$$\mathbf{S}_{12}^{(Ref)} = 2\mathbf{A}_{Ref}^{-1} \quad (178)$$

$$\mathbf{S}_{21}^{(Ref)} = 0.5(\mathbf{A}_{Ref} - \mathbf{B}_{Ref} \mathbf{A}_{Ref}^{-1} \mathbf{B}_{Ref}) \quad (179)$$

$$\mathbf{S}_{22}^{(Ref)} = -\mathbf{B}_{Ref} \mathbf{A}_{Ref}^{-1}, \quad (180)$$

with

$$\mathbf{A}_{Ref} = \mathbf{W}_0^{-1} \mathbf{W}_{Ref} + \mathbf{V}_0^{-1} \mathbf{V}_{Ref} \quad (181)$$

$$\mathbf{B}_{Ref} = \mathbf{W}_0^{-1} \mathbf{W}_{Ref} - \mathbf{V}_0^{-1} \mathbf{V}_{Ref} \quad (182)$$

And

$$\mathbf{S}^{(Trn)} = \begin{bmatrix} \mathbf{S}_{11}^{(Trn)} & \mathbf{S}_{12}^{(Trn)} \\ \mathbf{S}_{21}^{(Trn)} & \mathbf{S}_{22}^{(Trn)} \end{bmatrix}, \quad (183)$$

where

$$\mathbf{S}_{11}^{(Trn)} = -\mathbf{B}_{Trn} \mathbf{A}_{Trn}^{-1} \quad (184)$$

$$\mathbf{S}_{12}^{(Trn)} = 0.5(\mathbf{A}_{Trn} - \mathbf{B}_{Trn} \mathbf{A}_{Trn}^{-1} \mathbf{B}_{Trn}) \quad (185)$$

$$\mathbf{S}_{21}^{(Trn)} = 2\mathbf{A}_{Trn}^{-1} \quad (186)$$

$$\mathbf{S}_{22}^{(Trn)} = -\mathbf{A}_{Trn}^{-1} \mathbf{B}_{Trn}, \quad (187)$$

with

$$\mathbf{A}_{Trn} = \mathbf{W}_0^{-1} \mathbf{W}_{Trn} + \mathbf{V}_0^{-1} \mathbf{V}_{Trn} \quad (188)$$

$$\mathbf{B}_{Trn} = \mathbf{W}_0^{-1} \mathbf{W}_{Trn} - \mathbf{V}_0^{-1} \mathbf{V}_{Trn}. \quad (189)$$

2.2.4 Calculating Transmitted and Reflected Electric Field

The global scattering matrix connects the input from the reflection region to the output at the transmission region

$$\begin{bmatrix} \mathbf{c}_{Ref} \\ \mathbf{c}_{Trn} \end{bmatrix} = \begin{bmatrix} \mathbf{S}_{11}^{(Global)} & \mathbf{S}_{12}^{(Global)} \\ \mathbf{S}_{21}^{(Global)} & \mathbf{S}_{22}^{(Global)} \end{bmatrix} \begin{bmatrix} \mathbf{c}_{inc} \\ \mathbf{0} \end{bmatrix}, \quad (190)$$

where

$$\mathbf{c}_{inc} = \mathbf{W}_{Ref}^{-1} \mathbf{s}_T^{inc} \quad (191)$$

The term \mathbf{s}_T^{inc} is the electric field source defined as

$$\mathbf{s}_T^{inc} = \begin{bmatrix} p_x \delta_{0,pq} \\ p_y \delta_{0,pq} \end{bmatrix}, \quad (192)$$

where p_x and p_y are the x and y components of a unit amplitude polarization vector \mathbf{P} . The delta function ($\delta_{0,pq}$) is defined as $\delta_{0,pq} = [0, 0, \dots, 1, \dots, 0, 0]^T$. The coefficients for the reflected and transmitted fields can be computed from eqn. (190) as

$$\mathbf{c}_{Ref} = \mathbf{S}_{11}^{(Global)} \mathbf{c}_{inc} \quad (193)$$

$$\mathbf{c}_{Trn} = \mathbf{S}_{21}^{(Global)} \mathbf{c}_{inc} \quad (194)$$

The transverse components of the reflected and transmitted fields are then

$$\begin{bmatrix} \mathbf{r}_x \\ \mathbf{r}_y \end{bmatrix} = \mathbf{W}_{Ref} \mathbf{c}_{Ref} = \mathbf{W}_{Ref} \mathbf{S}_{11}^{(Global)} \mathbf{c}_{inc} \quad (195)$$

$$\begin{bmatrix} \mathbf{t}_x \\ \mathbf{t}_y \end{bmatrix} = \mathbf{W}_{Trn} \mathbf{c}_{Trn} = \mathbf{W}_{Trn} \mathbf{S}_{21}^{(Global)} \mathbf{c}_{inc}. \quad (196)$$

The longitudinal field components are calculated from the transverse components using the divergence equation and are given as

$$\mathbf{r}_z = -\mathbf{K}_{z,Ref}^{-1}(\mathbf{K}_x \mathbf{r}_x + \mathbf{K}_y \mathbf{r}_y), \quad (197)$$

and

$$\mathbf{t}_z = -\mathbf{K}_{z,Trn}^{-1}(\mathbf{K}_x \mathbf{t}_x + \mathbf{K}_y \mathbf{t}_y), \quad (198)$$

where $\mathbf{K}_{z,Ref} = -(\sqrt{\mu_{r,Ref}\epsilon_{r,Ref}\mathbf{I} - \mathbf{K}_x^2 - \mathbf{K}_y^2})^*$ and $\mathbf{K}_{z,Trn} = (\sqrt{\mu_{r,Trn}\epsilon_{r,Trn}\mathbf{I} - \mathbf{K}_x^2 - \mathbf{K}_y^2})^*$.

2.2.5 Calculating Diffraction Efficiencies

The diffraction efficiencies \mathbf{R} and \mathbf{T} are computed as

$$\mathbf{R} = \mathbb{R} \left[\frac{-\mathbf{K}_{z,Ref}}{k_{z,inc}} \right] \cdot |\mathbf{r}|^2, \quad (199)$$

and

$$\mathbf{T} = \mathbb{R} \left[\frac{\mu_{r,Ref} \mathbf{K}_{z,Trn}}{\mu_{r,Trn} k_{z,inc}} \right] \cdot |\mathbf{t}|^2, \quad (200)$$

where

$$|\mathbf{r}|^2 = |\mathbf{r}_x|^2 + |\mathbf{r}_y|^2 + |\mathbf{r}_z|^2, \quad (201)$$

and

$$|\mathbf{t}|^2 = |\mathbf{t}_x|^2 + |\mathbf{t}_y|^2 + |\mathbf{t}_z|^2. \quad (202)$$

2.2.6 Calculating Overall Reflectance and Transmittance

Finally, the overall reflectance R and transmittance T can be calculated by adding all of the diffraction efficiencies as

$$R = \sum \mathbf{R}, \quad (203)$$

and

$$T = \sum \mathbf{T}. \quad (204)$$

2.3 Finite-Difference Time-Domain Method

The finite-difference time-domain (FDTD) method [43–46] is one of the most widely used numerical technique for solving problems in electromagnetism. This method works by iterating Maxwell’s curl equation in a Yee grid (Figure 15) over time. The TMM and RCWA methods described in the previous sections are frequency domain solvers, whereas the FDTD method is a time domain solver; it is thus significant when the transient response of the structure is required. This method is also especially useful when the materials in the structure possess nonlinearity.

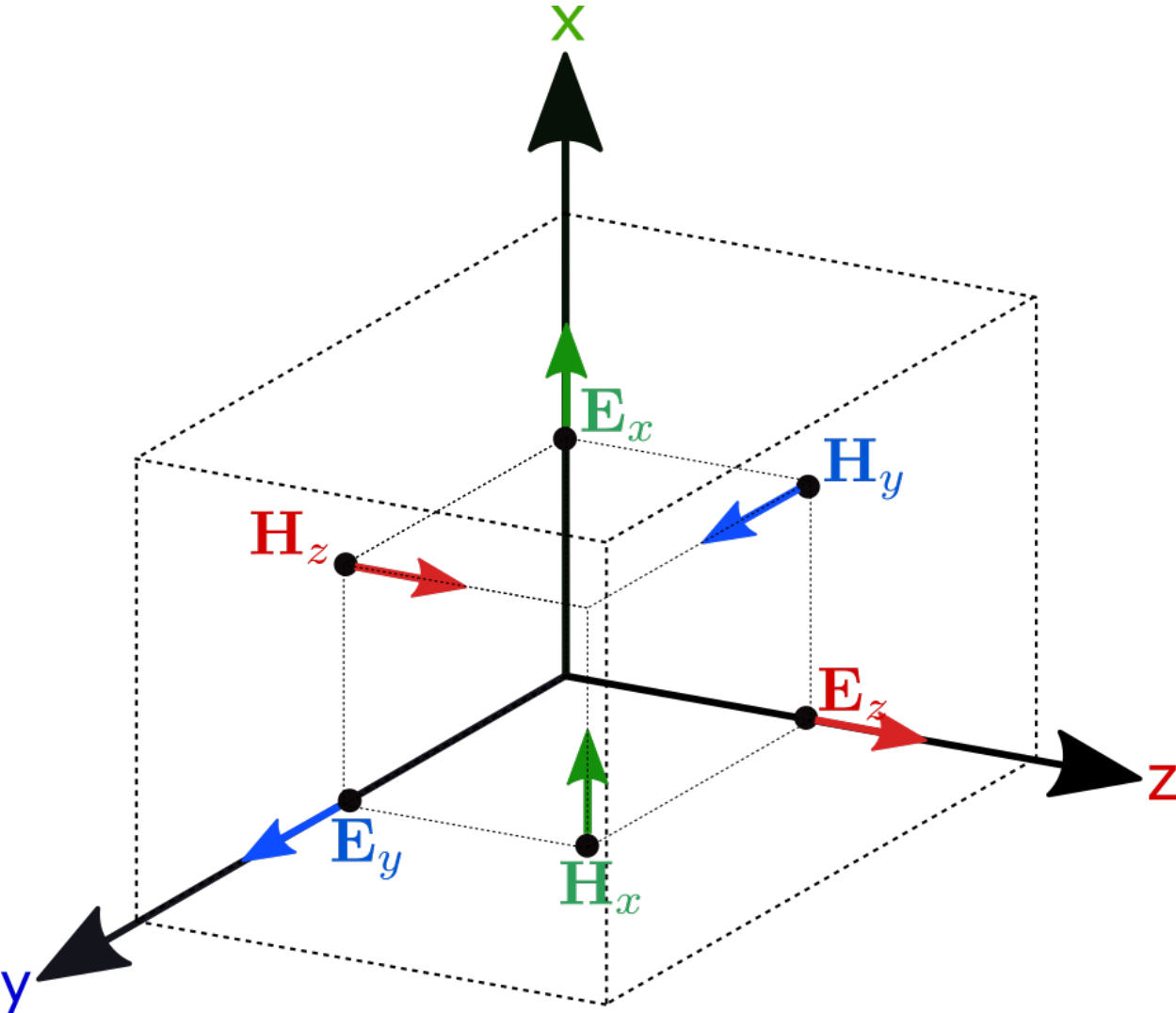


Figure 15: 3D FDTD Yee grid.

The formulation of FDTD method begins from Maxwell's equations as well. The normalized time-dependent Maxwell's curl equations for materials with diagonal permittivity tensor are

$$\nabla \times \mathbf{E} = -\frac{[\mu_{\mathbf{r}}]}{c_0} \frac{\partial \tilde{\mathbf{H}}}{\partial t} \quad (205)$$

$$\nabla \times \tilde{\mathbf{H}} = \frac{[\epsilon_{\mathbf{r}}]}{c_0} \frac{\partial \mathbf{E}}{\partial t}. \quad (206)$$

Eqn. (205) and (206) when expanded into their component forms give the final form of Maxwell's equations for the FDTD method.

$$\frac{\partial E_z}{\partial y} - \frac{\partial E_y}{\partial z} = -\frac{\mu_{xx}}{c_0} \frac{\partial \tilde{H}_x}{\partial t} \quad (207)$$

$$\frac{\partial E_x}{\partial z} - \frac{\partial E_z}{\partial x} = -\frac{\mu_{yy}}{c_0} \frac{\partial \tilde{H}_y}{\partial t} \quad (208)$$

$$\frac{\partial E_y}{\partial x} - \frac{\partial E_x}{\partial y} = -\frac{\mu_{zz}}{c_0} \frac{\partial \tilde{H}_z}{\partial t} \quad (209)$$

$$\frac{\partial \tilde{H}_z}{\partial y} - \frac{\partial \tilde{H}_y}{\partial z} = \frac{\epsilon_{xx}}{c_0} \frac{\partial E_x}{\partial t} \quad (210)$$

$$\frac{\partial \tilde{H}_x}{\partial z} - \frac{\partial \tilde{H}_z}{\partial x} = \frac{\epsilon_{yy}}{c_0} \frac{\partial E_y}{\partial t} \quad (211)$$

$$\frac{\partial \tilde{H}_y}{\partial x} - \frac{\partial \tilde{H}_x}{\partial y} = \frac{\epsilon_{zz}}{c_0} \frac{\partial E_z}{\partial t} \quad (212)$$

The above equations are approximated using finite difference techniques and then iteratively solved until the simulation is finished. The finite difference approximations for are as follows

$$\frac{E_z^{i,j+1,k}|_t - E_z^{i,j,k}|_t}{\Delta y} - \frac{E_y^{i,j,k+1}|_t - E_y^{i,j,k}|_t}{\Delta z} = -\frac{\mu_{xx}^{i,j,k}}{c_0} \frac{\tilde{H}_x^{i,j,k}|_{t+\frac{\Delta t}{2}} - \tilde{H}_x^{i,j,k}|_{t-\frac{\Delta t}{2}}}{\Delta t} \quad (213)$$

$$\frac{E_x^{i,j,k+1}|_t - E_x^{i,j,k}|_t}{\Delta z} - \frac{E_z^{i+1,j,k}|_t - E_z^{i,j,k}|_t}{\Delta x} = -\frac{\mu_{yy}^{i,j,k}}{c_0} \frac{\tilde{H}_y^{i,j,k}|_{t+\frac{\Delta t}{2}} - \tilde{H}_y^{i,j,k}|_{t-\frac{\Delta t}{2}}}{\Delta t} \quad (214)$$

$$\frac{E_y^{i+1,j,k}|_t - E_y^{i,j,k}|_t}{\Delta x} - \frac{E_x^{i,j+1,k}|_t - E_x^{i,j,k}|_t}{\Delta y} = -\frac{\mu_{zz}^{i,j,k}}{c_0} \frac{\tilde{H}_z^{i,j,k}|_{t+\frac{\Delta t}{2}} - \tilde{H}_z^{i,j,k}|_{t-\frac{\Delta t}{2}}}{\Delta t} \quad (215)$$

$$\frac{\tilde{H}_z^{i,j,k}|_{t+\frac{\Delta t}{2}} - \tilde{H}_z^{i,j-1,k}|_{t+\frac{\Delta t}{2}}}{\Delta y} - \frac{\tilde{H}_y^{i,j,k}|_{t+\frac{\Delta t}{2}} - \tilde{H}_y^{i,j,k-1}|_{t+\frac{\Delta t}{2}}}{\Delta z} = \frac{\epsilon_{xx}^{i,j,k}}{c_0} \frac{E_x^{i,j,k}|_{t+\Delta t} - E_x^{i,j,k}|_t}{\Delta t} \quad (216)$$

$$\frac{\tilde{H}_x^{i,j,k}|_{t+\frac{\Delta t}{2}} - \tilde{H}_x^{i,j,k-1}|_{t+\frac{\Delta t}{2}}}{\Delta y} - \frac{\tilde{H}_z^{i,j,k}|_{t+\frac{\Delta t}{2}} - \tilde{H}_z^{i-1,j,k}|_{t+\frac{\Delta t}{2}}}{\Delta z} = \frac{\epsilon_{yy}^{i,j,k}}{c_0} \frac{E_y^{i,j,k}|_{t+\Delta t} - E_y^{i,j,k}|_t}{\Delta t} \quad (217)$$

$$\frac{\tilde{H}_y^{i,j,k}|_{t+\frac{\Delta t}{2}} - \tilde{H}_y^{i-1,j,k}|_{t+\frac{\Delta t}{2}}}{\Delta x} - \frac{\tilde{H}_x^{i,j,k}|_{t+\frac{\Delta t}{2}} - \tilde{H}_x^{i,j-1,k}|_{t+\frac{\Delta t}{2}}}{\Delta y} = \frac{\epsilon_{zz}^{i,j,k}}{c_0} \frac{E_z^{i,j,k}|_{t+\Delta t} - E_z^{i,j,k}|_t}{\Delta t}. \quad (218)$$

The indices i , j , and k indicate the grid positions in x , y , and z directions, Δx , Δy , Δz , and Δt are step sizes in x , y , z , and forward time directions respectively. For numerical stability, the time step should satisfy the Courant stability condition [44]

$$\Delta t \leq \frac{n_{min}}{c_0 \sqrt{\frac{1}{\Delta x^2} + \frac{1}{\Delta y^2} + \frac{1}{\Delta z^2}}}, \quad (219)$$

where n_{min} is the lowest refractive index of any structure in the device or computational domain.

For the present work, we use an open-source implementation of FDTD method known as Meep [47] by MIT. It is one of the most widely used and cited FDTD tools available. It uses a rectangular, Cartesian style mesh, for discretization of the computational space and time domain and solves for electric and magnetic fields on those grids. The field components within a Yee cell are computed at a slightly different locations as shown in Figure 15; the fields at all other positions can be computed by interpolating the results from its neighboring grid solutions. The computational domains can be terminated using perfectly matched layer (PML). It supports different types of input sources such as a total-field scattered-field (TFSF) source, plane waves, beams, point dipoles, and a guided-mode source.

2.4 Finite Element Method

The finite element method (FEM) is one of the most powerful techniques for solving general partial differential equations (PDE). For electromagnetic problems, although it can be used for transient problems, it is mostly used for frequency domain problems. The real power of the FEM comes when the structures have irregular shapes. The TMM is useful only for planar structures with periodicity in one dimension and the RCWA method can be used for structures with periodicity in all three dimensions. Although the FDTD method can be used for more complex structures, it requires very fine meshing for such structures and

hence requires a significant amount of time. The FEM, on the other hand, is best suited for structures with complex and irregular shapes.

For electromagnetic problems, the FEM starts from Maxwell's curl equations [48–51], which we write here in slightly different form than in eqn. (29) and (30) as

$$\nabla \times \mathbf{E} = -j\omega\mu_0\mu_r\mathbf{H} \quad (220)$$

$$\nabla \times \mathbf{H} = j\omega\epsilon_0\epsilon_r\mathbf{E}, \quad (221)$$

where ϵ_0 and μ_0 are the vacuum permittivity and permeability, ϵ_r and μ_r are the relative permittivity and permeability respectively. Eqn. (220) and (221) can be combined into one equation by taking the curl of eqn. (221), and then substituting Eqn. (220) into the resulting equation as

$$\nabla \times \frac{1}{\epsilon_r} \nabla \times \mathbf{H} - \omega^2 \epsilon_0 \mu_0 \mu_r \mathbf{H} = \mathbf{0} \quad (222)$$

Decomposing eqn. (222) into its transverse and longitudinal components, we get

$$\nabla_T \times \frac{1}{\epsilon_r} \nabla_T \times \mathbf{H}_T - j\beta \frac{1}{\epsilon_r} (\nabla_T H_z + j\beta \mathbf{H}_t) - \omega^2 \epsilon_0 \mu_0 \mu_r \mathbf{H}_T = \mathbf{0} \quad (223)$$

$$\nabla_T \times \frac{1}{\epsilon_r} (\nabla_T H_z + j\beta \mathbf{H}_T) \times \mathbf{z} - \omega^2 \epsilon_0 \mu_0 \mu_r H_z \mathbf{z} = \mathbf{0}, \quad (224)$$

where for simplicity $\frac{\partial}{\partial z}$ is replaced by $-j\beta$; β is the phase constant. The subscript “ T ” and “ z ” indicate the transverse and longitudinal components respectively. We now introduce a variable transformation [48] to find the eigen value β ,

$$\mathbf{h}_T = \beta \mathbf{H}_T \quad (225)$$

$$h_z \mathbf{z} = -jk_0 H_z \mathbf{z}. \quad (226)$$

Substituting eqn. (225) and (226) in eqn. (223) and (224) give

$$\nabla_T \times \frac{1}{\epsilon_r} \nabla_T \times \mathbf{h}_T - k_0^2 \mu_r \mathbf{h}_T = -\frac{\beta^2}{\epsilon_r} \left(\nabla_T \frac{h_z}{k_0} + \mathbf{h}_T \right) \quad (227)$$

and

$$\beta^2 \left[\frac{1}{k_0} \nabla_T \cdot \frac{1}{\epsilon_r} \left(\nabla_T \frac{h_z}{k_0} + \mathbf{h}_z \right) + \mu_r h_z \right] = \mathbf{0} \quad (228)$$

respectively. The above two coupled differential equations with the appropriate boundary conditions can now be solved for β^2 . The boundary conditions on perfect magnetic conductors (PMC) are

$$\mathbf{n} \times \mathbf{h}_T = \mathbf{0} \quad (229)$$

$$h_z = 0. \quad (230)$$

Similarly, for perfect electric conductors (PEC), the boundary conditions are

$$(\nabla_T h_z + \mathbf{h}_T) \cdot \mathbf{n} = \mathbf{0} \quad (231)$$

$$\nabla_T \times \mathbf{h}_T = 0. \quad (232)$$

2.4.1 Weak Formulation

The FEM for electromagnetics uses a weak formulation of eqn. (227) and (228) subject to the boundary conditions in eqn. (229)-(232). To obtain the weak formulation, we multiply each of the equations by a test function, and integrate the resulting equations over the waveguide cross-sectional area. Multiplying (dot product) eqn. (227) by a test function \mathbf{h}_T^* , and then integrating by parts, we get

$$\int_s \mathbf{h}_T^* \cdot \left[\nabla_T \times \frac{1}{\epsilon_r} \nabla_T \times \mathbf{h}_T - k_0^2 \mu_r \mathbf{h}_T \right] ds = \int_s \left[-\mathbf{h}_T^* \cdot \left(\frac{\beta^2}{\epsilon_r} \left(\nabla_T \frac{h_z}{k_0} + \mathbf{h}_T \right) \right) \right] ds \quad (233)$$

Similarly, we multiply eqn. (228) by a test function h_z^* and get

$$\int_s h_z^* \beta^2 \left[\frac{1}{k_0} \nabla_T \cdot \frac{1}{\epsilon_r} \left(\nabla_T \frac{h_z}{k_0} + \mathbf{h}_T \right) + \mu_r h_z \right] ds = \mathbf{0}. \quad (234)$$

Eqn. (233) and (234) can be further simplified by integrating the equations by part and applying Green's theorem [50],

$$\int_s \left[\nabla_T \times \mathbf{h}_T^* \cdot \frac{1}{\epsilon_r} \nabla_T \times \mathbf{h}_T \right] ds - \int_s k_0^2 \mu_r \mathbf{h}_T^* \cdot \mathbf{h}_T ds = \int_s \left[-\mathbf{h}_T^* \cdot \left(\frac{\beta^2}{\epsilon_r} \left(\nabla_T \frac{h_z}{k_0} + \mathbf{h}_T \right) \right) \right] ds \quad (235)$$

$$- \int_s \frac{\beta^2}{\epsilon_r} \left[\left(\nabla_T \frac{h_z^*}{k_0} \right) \cdot \left(\nabla_T \frac{h_z}{k_0} \right) \right] ds - \int_s \frac{\beta^2}{\epsilon_r} \left[\left(\nabla_T \frac{h_z^*}{k_0} \right) \cdot \mathbf{h}_T \right] ds + \int_s \mu_r \beta^2 h_z h_z^* ds = \mathbf{0}. \quad (236)$$

Finally, combining these equations we get a full vectorial weak form as

$$\begin{aligned} & \int_s \left[\nabla_T \times \mathbf{h}_T^* \cdot \frac{1}{\epsilon_r} \nabla_T \times \mathbf{h}_T \right] ds - \int_s k_0^2 \mu_r \mathbf{h}_T^* \cdot \mathbf{h}_T ds \\ &= -\beta^2 \int_s \left[\left(\nabla_T \frac{h_z}{k_0} + \mathbf{h}_T \right) \cdot \frac{1}{\epsilon_r} \left(\nabla_T \frac{h_z^*}{k_0} + \mathbf{h}_T^* \right) - \mu_T h_z h_z^* \right] ds \end{aligned} \quad (237)$$

A similar expression for electric field can also be obtained in a similar manner. In this work, we use COMSOL Multiphysics [52], a commercial implementation of the FEM, which is a computational tool for general PDEs. For problems in electromagnetism, it solves equation similar to eqn. (237) subject to the appropriate boundary conditions.

CHAPTER 3

SLOW LIGHT BY BLOCH SURFACE WAVE TUNNELING

3.1 Introduction

Interest in slow light began after the research group led by Hau et al. [53] slowed down the speed of light to 17 meters per second using the technique of electromagnetically induced transparency (EIT) in a Bose-Einstein condensate. In a recent experiment [54], light has been stopped and used for image storage by EIT up to a time of one minute, setting a new benchmark for EIT-based light stopping. Although the recent experiment uses a doped $\text{Pr}^{3+}:\text{Y}_2\text{SiO}_5$ crystal instead of atomic gas, it still requires temperatures lower than 4K for its operation, which limits the adoption of the technique in real-world applications. A more practical way to achieve slow light is through the use of photonic band gap materials (PBGs), which operate at room temperature [55–60]. Significant reduction in the speed of light in PBGs is mainly attributed to photonic band-structure effects due to a spatially periodic dielectric function, rather than from material dispersion [61]. Theoretically and numerically, using loss-less PC waveguides, researchers have been able to completely stop light at the vicinity of band gap edges by dynamically tuning the properties of the material while the light is still in the material [62,63]. With no dynamic tuning, the authors of ref. [64] claim three orders of magnitude reduction in the speed of light ($v_g \sim 0.0008c$). However, due to leaky modes, out of plane radiation, material absorption, and structural distortion, even the three orders of magnitude reduction is not realizable in practice. These effects inherently imposes limits on the maximum achievable slow down factor in PBGs. Such imperfections can partially be accounted for in simulations by adding a small imaginary part to the otherwise real-valued refractive indices of the materials used in PBGs.

Slowing down the speed of light is of significance for many practical applications. Slow light in optical devices can be used to make optical buffers which temporarily store light

[65, 66]. Contrary to its name, it can actually increase the speed of telecommunications and data transfer in photonic crystal waveguides [67, 68]. Higher density of modes and enhanced light-matter interaction assisted by slow light in PBGMs can in turn enhance light amplification [69], nonlinear phase sensitivity [70], nonlinearities in the material response [71], and stimulated Raman scattering [73]. Recently, applications in sensing have also been proposed based on slow light in photonic crystal waveguides [74, 75].

In this paper, we introduce a new configuration that can reduce the speed of light by a factor of up to 400 in a prism tunneling configuration using the Bloch surface wave (BSW) on a one dimensional photonic bandgap $\text{TiO}_2\text{-SiO}_2$ multilayer as an intermediate excitation. BSWs [10, 31] are propagating non-radiative, surface-bound electromagnetic waves that exist within the forbidden band gap of the multilayer. The frequency of BSWs can be located anywhere within the band gap by adjusting the thickness of the termination layer of the photonic multilayer. For the simulations presented here we chose an operating optical wavelength (632.8 nm) tuned to the BSW mode. To our knowledge, this technique of generating slow light assisted by BSW of a one-dimensional PBGM has not been reported in the literature; the traditional approach has been slow light generation at the bandgap edges.

3.2 Simulation Approach

The optical configuration for the generation of slow light using BSW on a one-dimensional PBGM is shown in Figure 16. The set up consists of two prisms separated by an air gap. One prism has a PBGM multilayer structure deposited on its reflecting face such that when light is incident at the appropriate phase matching angle, BSWs are excited at the multilayer-air interface. Excitation of BSWs is indicated by a sharp drop in the reflected light. BSW is a surface bound excitation with evanescent fields that penetrate both into the multilayer and the air. The second prism permits the evanescent BSW field in the air to become a radiative wave that is transmitted out of the prism as shown. The process is similar to the frustrated total internal reflection, a configuration much explored in previous work on group velocity

manipulation [76]. For the simulation, a collimated optical beam with a Gaussian temporal pulse profile is incident through the prism at θ_{res} , the resonant angle for BSW excitation. The Gaussian pulse is described by

$$y(t) = A \sin(\omega_0 t) \exp\left(-\frac{(t - t_0)^2}{2\sigma^2}\right), \quad (238)$$

where A is the amplitude of the pulse, t is time, t_0 is the center of the pulse, and σ is the pulse envelope width.

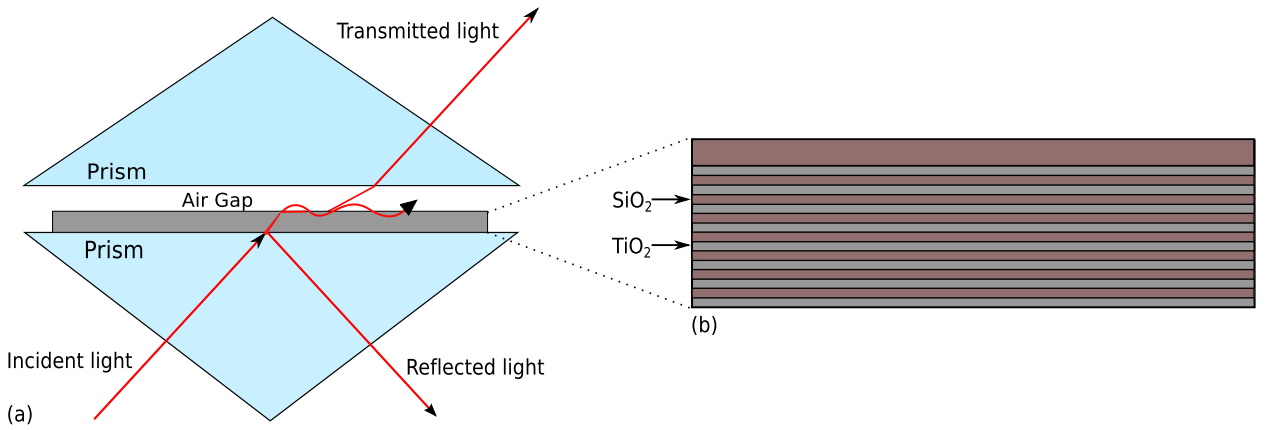


Figure 16: A schematic diagram of the configuration for slow light generation using BSW as an intermediate excitation.

Using the 2×2 matrix formulation for a layered medium [31], transmittance coefficients of each frequency present in the pulse are computed. These transmittance coefficients are complex numbers, containing both the amplitude and phase information of transmitted light as a function of frequency. To determine the effect of this transmittance function on our Gaussian pulse, we form the Fast Fourier Transform (FFT) of the pulse and multiply each frequency component by the corresponding complex transmittance value. The result is the spectrum of the transmitted pulse in the frequency domain. An inverse FFT is then used to recover the transmitted pulse as a function of time. The difference between the peaks of the input and transmitted pulses is called the group-delay (τ_g), which can be computed using

the phase information of the transmittance function and is given by

$$\tau_g = -\frac{d\phi(\omega)}{d\omega}, \quad (239)$$

where ϕ is the phase of the pulse at a given frequency ω . The group velocity (v_g) is consequently given by

$$v_g = \frac{z}{\tau_g}, \quad (240)$$

where z is the total propagation distance of the pulse. The group index (n_g), which is a slow-down factor from the velocity c [66] is

$$n_g = \frac{c}{v_g}. \quad (241)$$

3.3 Results and Discussions

The results represented here are based upon a one-dimensional PBGM which consists of a multilayer composed of eight bilayers of TiO_2 (refractive index = $(4.84 + i0.0007)^{1/2}$) and SiO_2 (refractive index = $(2.1316 + i0.0001)^{1/2}$), with thicknesses of 82.8 nm and 154.9 nm respectively. The termination layer has a thickness of 185 nm which results in a BSW mode near the center of the bandgap. The band structure of the multilayer (see Figure 16(b)) is shown in Figure 17. The vertical axis represents normalized frequency and the horizontal axis the wave vector component parallel to the plane of the multilayer. The BSW, as a surface bound wave, has its wave vector entirely in this plane. The dispersion diagram shows regions in which light is radiative into the multilayer (green shaded) and regions in which it is non-radiative into the multilayer (blue shaded). The band of blue that rises from left to right in the figure represents the photonic band gap in the multilayer. The plot also shows the limiting light line as the red dashed line. This line is the dispersion for light incident at grazing incidence along the multilayer surface. For light at other angles of incidence in air the parallel component will be smaller, thus the entire region to the left of the limiting light line is radiative into the air side of the multilayer. BSWs exist in a region in which the mode

is not radiative into either the air or the multilayer. This region is shown as the narrow strip to the right of the light line and within the photonic band gap. Given this dispersion relation we set the wavelength of light for our simulation to be 632.8nm ($\omega = 0.3756 [2\pi c/\Lambda]$) and $\theta_{res} = 44.39^\circ$ ($\beta = 0.3838 [2\pi/\Lambda]$), corresponding to the narrow defect mode region in Figure 17.

Reduction in the speed of light in the defect mode of the multilayer can be attributed to the generation of the BSW at the resonance frequency. The light is stored temporarily on the surface of the multilayer in the form of the BSW before being transmitted to the second prism through the air gap. The thickness of the air gap determines the strength of coupling between the BSW and the second prism and hence establishes the lifetime of the BSW before it becomes radiative. The air gap can be adjusted appropriately to obtain the maximum time delay possible. Figure 18(a) shows the maximum time delays gained at different air gap thickness for a eight bilayered TiO₂-SiO₂ multilayer. An optimum time delay of 4.209 ps ($n_g \sim 350$) was achieved with air gap thickness of 1600 nm, which can also be clearly seen in Figure 18(b). The transmitted (red) pulse is shifted to the right compared to the incident (blue) pulse, meaning that the pulse takes a longer time to travel the same distance when the multilayer is present on its way compared to the situation when there is a glass-slab of equal thickness in place of the multilayer. To observe the optimum group-delay, however, a sufficiently long-enough pulse is required. This is important because the frequency bandwidth of the pulse has to lie within the narrow transmission bandwidth of the multilayer to observe slow light. In our simulation, this was ensured by requiring the FFT spectrum of the incident pulse to completely lie within the transmittance region. Moreover, the transmission bandwidth of the multilayer becomes narrower with the increase in the number of bilayers. So, an even longer pulse is required for multilayers with a higher number of bilayers.

To exhibit the behavior of the group index (slow-down factor) and transmittance with respect to increasing air-gap thickness, a plot is presented in Figure 19(a) with the multilayer

of 8 bilayers. At smaller air-gap thickness, higher transmittance is observed but the group index is low, and vice-versa. Adjusting these properties, a required group delay with some acceptable transmittance can be easily acquired. The plot also shows that increasing the air-gap thickness after a certain level does not further increase the group index. In fact, the group index starts decreasing, owing to the fact that increasing the air-gap thickness decreases the transmittance significantly. The transmitted pulse tunnels through the air-gap in the form of an evanescent wave which is a very short-range wave. Thus, with increasing air-gap thickness, only a small amount of input light is tunneled across the air-gap which eventually starts decreasing the group index.

A similar behavior is also seen with the increase in the number of bilayers in the multilayer (Figure 19(b)). Increasing the number of bilayers and setting an appropriate air gap thickness initially increases the group index, but after reaching a certain limiting number of bilayers, improvement in the group index is not seen. Adding more bilayers increases internal reflections, absorption, and scattering which limits the amount of transmitted light resulting in the low transmittance and group index.

3.4 Summary

Our study shows that a simple one-dimensional PBG multilayer structure in a prism-coupled BSW configuration can reduce the speed of light by about a factor of up to 400 when operated at its narrow defect mode transmission region. This finding is remarkable, keeping in mind that losses due to material absorption are not ignored. The slow-down factor depends greatly on the number of bilayers in the multilayer and on the air gap thickness. Further improvement in the slow down factor is possible by wisely choosing materials with higher refractive index contrast for the multilayers.

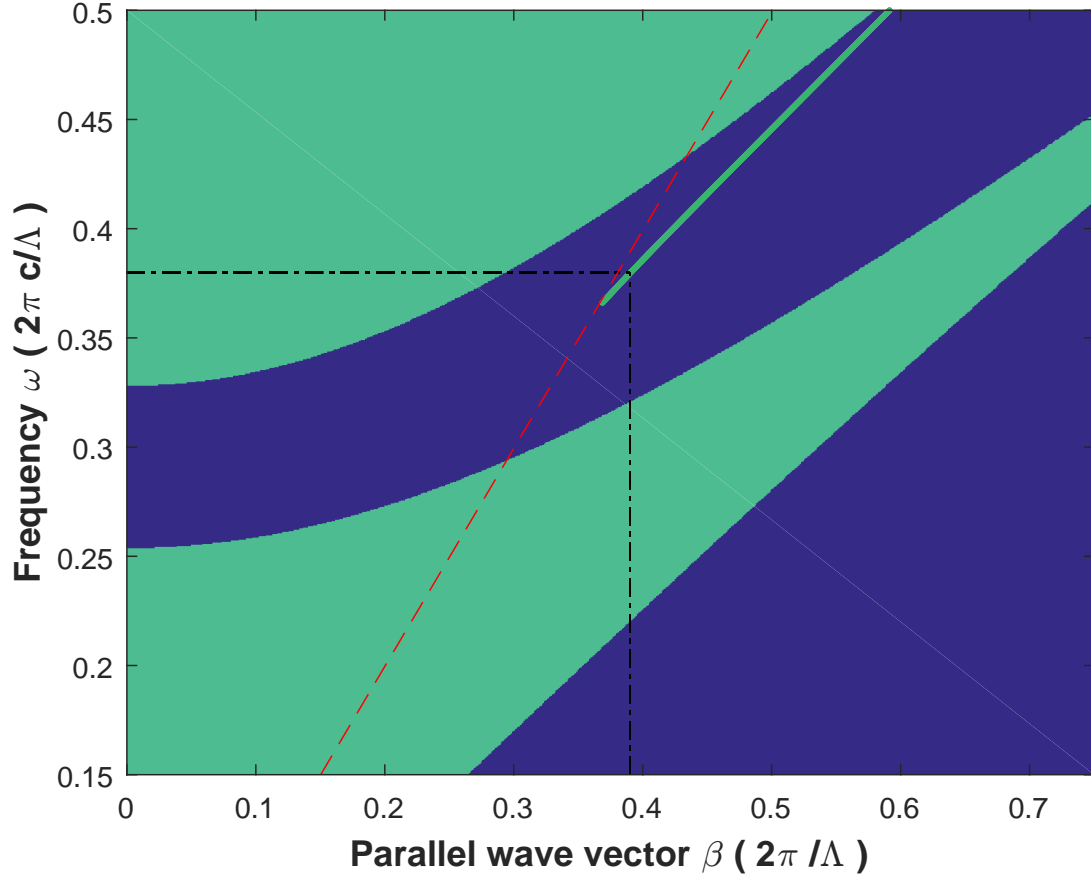


Figure 17: Surface dispersion diagram for an 8 bilayer multilayer $\text{TiO}_2\text{-SiO}_2$ PBGM used in the simulations. The red dashed line represents the limiting lightline in air. The green and blue shaded areas represent radiative and non-radiative regions respectively into the multilayer. The plot units are in reduced angular frequency ($2\pi c/\Lambda$) and wavevector ($2\pi/\Lambda$) where Λ is the periodicity of the multilayer.

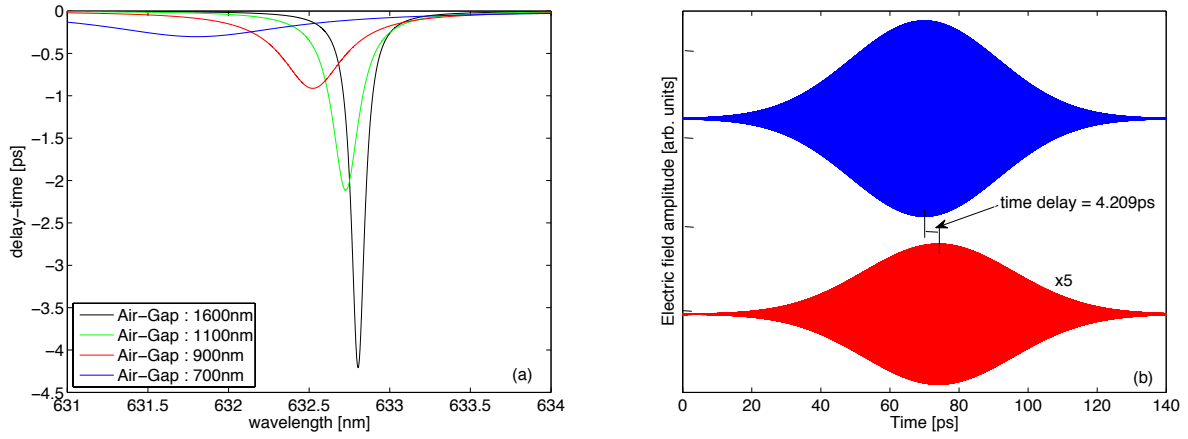


Figure 18: (a) Delay time as a function of wavelength for four different air gap values. (b) Incident (top) and transmitted (bottom) pulses showing 4.209 ps delay.

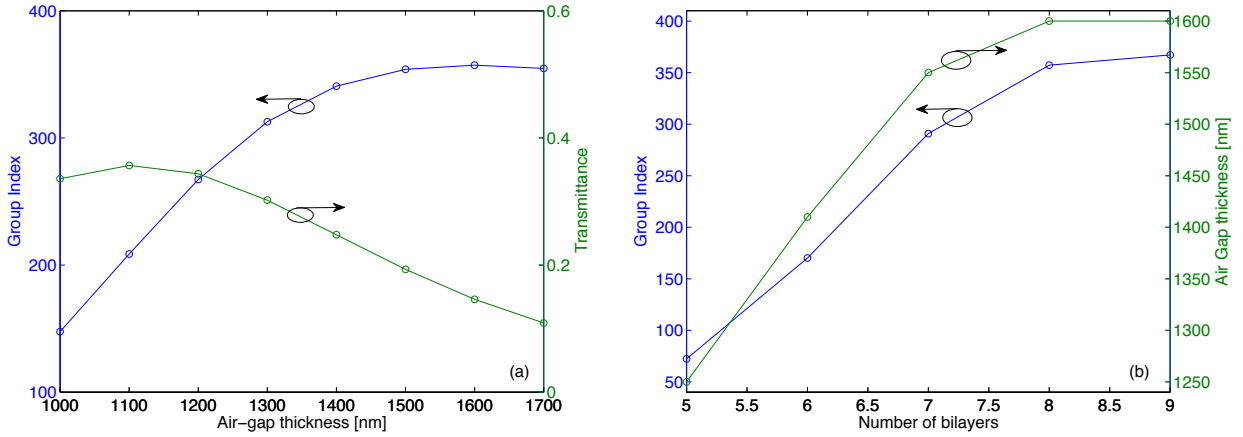


Figure 19: (a) Group Index (blue) and corresponding transmittance (green) as a function of air-gap thickness with the number of $\text{TiO}_2\text{-SiO}_2$ bilayers = 8. (b) Group Index (blue) and Air Gap thickness (green) as a function of number of bilayers.

CHAPTER 4

EXCITATION OF BLOCH-LIKE SURFACE WAVES IN QUASI-CRYSTALS AND APERIODIC DIELECTRIC MULTILAYERS

4.1 Introduction

Bloch surface waves (BSWs) are electromagnetic modes propagating at the interface of truncated dielectric multilayer structures and a homogeneous dielectric medium. BSWs were first predicted by Meade et al. [7], and later experimentally observed in photonic crystals by Robertson et al. [8]. Recently BSWs have also been studied and experimentally observed in various configurations [9, 10, 25]. In all of the studies however, the photonic crystals under consideration were periodic in nature, i.e., alternating layers of high and low refractive index materials, with a surface defect. This preference towards periodic crystals for excitation of BSWs is largely due to the establishment of their robust and well-understood theoretical background, which makes it easier to model and predict the behavior to BSWs in such structures. It is also easy to fabricate periodic crystals for real experiments and applications. On the other hand, despite the significant interest in optical characteristics of quasi-crystals and aperiodic photonic crystals, it has not been recognized that such structures also support Bloch-like surface waves (BLSWs). Other optical properties of these aperiodic systems such as dispersion and bandgaps [77, 78], perfect transmission [79, 81], propagation [82, 84] and localization [85, 86] of light have been extensively studied. It is observed that when compared to their periodic counterparts, quasi-crystals and aperiodic multilayers exhibit enhanced optical properties and also add significant flexibility in optical engineering [87]. Recognizing this fact, we recently showed via numerical simulation that BLSWs can exist in a 34 layered Fibonacci quasi-crystal (FQC) and a 32 layered Thue-Morse aperiodic dielectric multilayer (TMADM) structure [88]. In this paper, we extend our study of BLSWs in quasi-crystals and aperiodic dielectric multilayers to different generations of FQCs and TMADMs. Moreover,

we look into their applicability for making biosensors.

The advantage of FQCs and TMADMs over conventional periodic dielectric multilayers (PDMs) is two fold. First, the electric field (E-field) intensity at the surface due to BLSWs in FQCs and TMADMs is significantly improved compared to their periodic counterparts. This improved surface field intensity can be utilized for engineering optical slow-light devices [26], slow-light enhanced nonlinear effects [71,72], surface-enhanced Raman spectroscopy [29,30], label-free biosensing based on enhanced diffraction [24,99,100], spectral and angular resonance shift [18,23], and fluorescence-based detection [14,15,20]. Second, the penetration depth (PD) of the exponentially decaying BLSW in the homogeneous medium is increased. The extended PD results in a higher interaction with the homogeneous medium and consequently higher sensitivity to refractive index change in that medium. This feature, together with the improved surface field intensity of FQCs and TMADMs can be exploited to make sensitivity enhanced biosensors.

4.2 Materials and Computational Method

FQCs are one-dimensional quasi-crystals, first proposed by Kohmoto et. al. [90]. They can be constructed using a simple substitution rule $A \rightarrow AB$, $B \rightarrow A$. On the other hand, TMADMs are aperiodic multilayers [91,92] designed using the inflation rule $A \rightarrow AB$, and $B \rightarrow BA$. The first five generations of FQCs and TMADMs, assuming the first generation (S_0) to be A , are given in Tab. 1

Table 1: First four generations of FQCs and TMADMs

Generation (S_j)	FQC	TMADM
S_0	A	A
S_1	AB	AB
S_2	ABA	$ABBA$
S_3	$ABAAB$	$ABBABAAB$
S_4	$ABAABABA$	$ABBABAABBAABABBA$

The schematic of the theoretical model consisting of prism–FQC/TMADM–air is shown in Figure 20(a). Although BSW/BLSW modes are intrinsically present at dielectric-air interfaces, they cannot be directly excited by light incident from the air side due to their non-radiative and evanescent nature. The use of a prism mitigates this inability by providing an additional momentum to the free-space wave vector required to satisfy the phase matching condition with the BSW/BLSW wave vector. The coupling of the free-space wave vector into the BLSW wave vector can be realized by observing sharp dips in the reflection maps. For any particular wavelength, at incident angles above the critical angle, the dips in the reflectivity curve represent light coupling either into BLSW modes or inner guided modes. These modes can be distinguished by their characteristic E-field profiles. Knowing the angle of incidence at which BLSW is excited, the field profile can be computed by solving for the E-field iteratively in the multilayer structure imposing the continuity of E-field and its derivative at the interfaces. The BLSW modes have highly confined E-field at the surface layer and exponentially decaying field profile in the homogeneous superstrate layer.

For our FQC/TMADM, we use TiO_2 (A) and SiO_2 (B) as the high and low refractive index materials. We consider wavelength (λ) dependent refractive index of both TiO_2 [101] and SiO_2 [102] over the range of $0.43 \mu\text{m}$ to $0.8 \mu\text{m}$ given by

$$n_{\text{TiO}_2}^2 = 5.913 + \frac{0.2441}{\lambda^2 - 0.0803}, \quad (242)$$

and

$$n_{\text{SiO}_2}^2 = 1 + \frac{0.6961663\lambda^2}{\lambda^2 - 0.0684043^2} + \frac{0.4079462\lambda^2}{\lambda^2 - 0.1162414^2} + \frac{0.8974794\lambda^2}{\lambda^2 - 9.896161^2} \quad (243)$$

respectively. We note that the λ in Eqn. 242 and 243 is in the units of μm ; in the rest of the paper however, λ is given in nm. We also introduce small losses in these materials through the imaginary parts of their refractive indices. The values used here, 0.00016 and 0.000034 for TiO_2 and SiO_2 respectively, are based on the published sources [103, 104] and are selected to match with experimental investigations of BSWs [10, 18, 23]. We use a 34 layered FQC ($j = 7$) and a 32 layered TMADM ($j = 5$) with the thicknesses of 71.9 nm and 108.4 nm for the

TiO₂ and SiO₂ layers respectively. These layer thicknesses correspond to quarter wave stacks at the wavelength 632.8 nm for normal incidence, taking the refractive indices of TiO₂ and SiO₂ to be 2.2 and 1.46 respectively. Similar periodic systems have been extensively studied numerically and experimentally [9, 10, 18, 23]. However, since the structures studied in this Letter are not periodic, the choice is arbitrary; the freedom to choose essentially any values for layer thicknesses create an enormous parameter space in designing new applications. The number of layers, layer thicknesses, materials, and the superstrate refractive index are parameters that can be varied. Exploration of these parameter spaces is only amenable via numerical computation. This paper provides a roadmap for discovering and characterizing surface modes in these systems.

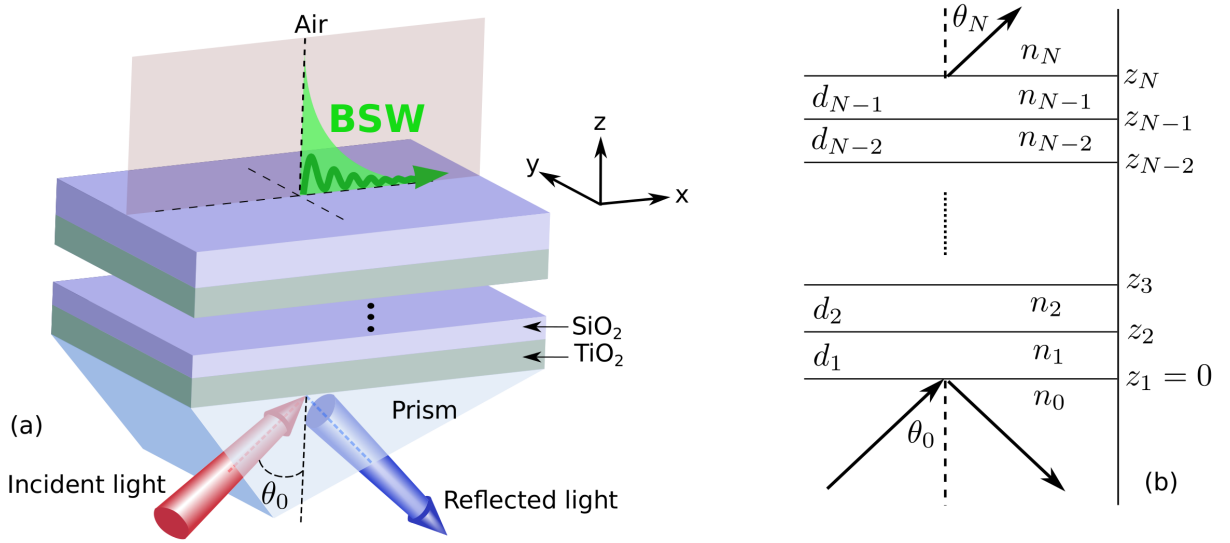


Figure 20: (a) A schematic of the prism coupling technique to excite Bloch-like surface wave in a dielectric multilayer. (b) A 2D schematic with the system parameters.

Because FQCs and TMADMs are not periodic, we consider a general plane wave incident of a stack of $N - 1$ layers as shown in Figure 20(b), with a total of N interfaces. The refractive indices and thicknesses of the layers are denoted by n_j and d_j respectively. The FQCs and TMADMs in this paper are all dielectric in nature; thus, we only consider transverse-electric

(TE) mode. For TE wave, $E_x = E_z = 0$ and $H_y = 0$. The remaining electric and magnetic field in each layer is of the form [105, 106]

$$\begin{aligned} E_{yj}(x, z, t) &= E_{yj}(z)\exp\{i(k_0\alpha_j x - \omega t)\}, \\ H_{xj}(x, z, t) &= H_{xj}(z)\exp\{i(k_0\alpha_j x - \omega t)\}, \\ H_{zj}(x, z, t) &= H_{zj}(z)\exp\{i(k_0\alpha_j x - \omega t)\}, \end{aligned} \quad (244)$$

where $E_{yj}(z)$, $H_{xj}(z)$, and $H_{zj}(z)$ are the complex amplitudes of appropriate fields in layer- j , $k_0 = 2\pi/\lambda_0$, and $\alpha_j = n_0\sin(\theta_0)$. The electric and magnetic fields amplitudes at the entrance of each layer are connected to the corresponding amplitudes at a distance z inside the layer as

$$\begin{bmatrix} E_{yj}^0 \\ H_{xj}^0 \end{bmatrix} = M_j \cdot \begin{bmatrix} E_{yj}(z) \\ H_{xj}(z) \end{bmatrix}, \quad M_j = \begin{bmatrix} \cos\beta_j & -\frac{i}{p_j}\sin\beta_j \\ -ip_j\sin\beta_j & \cos\beta_j \end{bmatrix}. \quad (245)$$

E_{yj}^0 and H_{xj}^0 are the respective amplitudes of E_{yj} and H_{xj} at the appropriate boundaries z_j of layer- j , M_j is the characteristic matrix of layer- j , $\beta_j = k_0n_jd_j\cos\theta_j$, and $p_j = \sqrt{(\epsilon_j/\mu_j)}\cos\theta_j$. In a multilayered structure, as considered in this paper, the fields amplitudes at the first and the last interfaces are connected through the total characteristic matrix of the structure

$$\begin{bmatrix} E_{y1}^0 \\ H_{x1}^0 \end{bmatrix} = M_{\text{TOT}} \cdot \begin{bmatrix} E_{yN}^0 \\ H_{xN}^0 \end{bmatrix}, \quad M_{\text{TOT}} = \prod_{j=1}^{j=N-1} M_j. \quad (246)$$

The complex reflection and transmission coefficients r and t can be computed as

$$\begin{aligned} r &= \frac{E_y^{ref}}{E_y^{inc}} = \frac{(M_{11} + M_{12} \cdot p_N) \cdot p_0 - (M_{21} + M_{22} \cdot p_N)}{(M_{11} + M_{12} \cdot p_N) \cdot p_0 + (M_{21} + M_{22} \cdot p_N)}, \\ t &= \frac{E_{yN}^0}{E_y^{inc}} = \frac{2 \cdot p_0}{(M_{11} + M_{12} \cdot p_N) \cdot p_0 + (M_{21} + M_{22} \cdot p_N)}, \end{aligned} \quad (247)$$

where E_y^{inc} , E_y^{ref} , and E_{yN}^0 are the incident, reflected and the transmitted electric fields amplitudes, and M_{ij} are the elements of the total characteristic matrix M_{TOT} .

The electric and magnetic fields in the 1st layer can then be calculated as

$$\begin{bmatrix} E_{y1}(z) \\ H_{x1}(z) \end{bmatrix} = P_1(z) \cdot \begin{bmatrix} (1+r) \\ p_0(1-r) \end{bmatrix} E_y^{inc}, \quad z_1 \leq z \leq z_2, \quad (248)$$

where

$$P_1(z) = \begin{bmatrix} \cos(k_0 n_1 z \cos \theta_1) & \frac{i}{p_j} \sin(k_0 n_1 z \cos \theta_1) \\ ip_j \sin(k_0 n_1 z \cos \theta_1) & \cos(k_0 n_1 z \cos \theta_1) \end{bmatrix}, \quad (249)$$

and the incident electric field $E_y^{inc} = 1$. Finally, the field distribution in the remaining layers can be calculated as

$$\begin{bmatrix} E_{yj}(z) \\ H_{xj}(z) \end{bmatrix} = P_1(z) \cdot \left(\prod_{l=j-1}^1 P_l(z = z_l + d_l) \right) \cdot \begin{bmatrix} (1+r) \\ p_0(1-r) \end{bmatrix} E_y^{inc}, \quad z_j \leq z \leq z_{j+1}, \quad (250)$$

where $P_j(z)$, inverse of $M_j(z)$, is the propagation matrix for the layer- j given by

$$P_j(z) = \begin{bmatrix} \cos(k_0 n_j (z - z_j) \cos \theta_j) & \frac{i}{p_j} \sin(k_0 n_j (z - z_j) \cos \theta_j) \\ ip_j \sin(k_0 n_j (z - z_j) \cos \theta_j) & \cos(k_0 n_j (z - z_j) \cos \theta_j) \end{bmatrix}. \quad (251)$$

For transverse magnetic (TM) mode, $H_x = H_z = 0$ and $E_y = 0$. All the above expressions are valid for the TM mode simply by replacing $p_j = \sqrt{(\epsilon_j/\mu_j)} \cos \theta_j$ by $q_j = \sqrt{(\mu_j/\epsilon_j)} \cos \theta_j$ and the field columns $\begin{bmatrix} E_{yj} \\ H_{xj} \end{bmatrix}$ by $\begin{bmatrix} H_{yj} \\ -E_{xj} \end{bmatrix}$.

4.3 Results and Discussions

BSWs can be observed in the reflection maps of FQCs or TMADMs, provided that the structures are designed appropriately to support them. Reflection maps capture the reflectivity response of the structure at different wavelengths and angle of incidence of the incident light. They can be computed from Eqn. (252). BSWs in reflection maps are characterized by sharp and narrow dips, which result in localized electric field at the surface of the structure. Figure 21(a) shows the reflection map of a 34 layered FQC. The vertical dotted line near the left boundary denotes the light line. We observe several optical modes beyond the light line over the wavelength range of 430-800 nm; most of the modes however, are guided modes in the inner layers of the FQC. The BLSW modes are highlighted with solid black curves and are labeled BLSW₁ and BLSW₂. In a periodic multilayer, the excitation of BSWs is attributed to the surface defect. The surface defect breaks the translational symmetry of the multilayer, which facilitates additional optical modes in the otherwise forbidden bandgaps [1]. The FQC pattern for Fibonacci order j

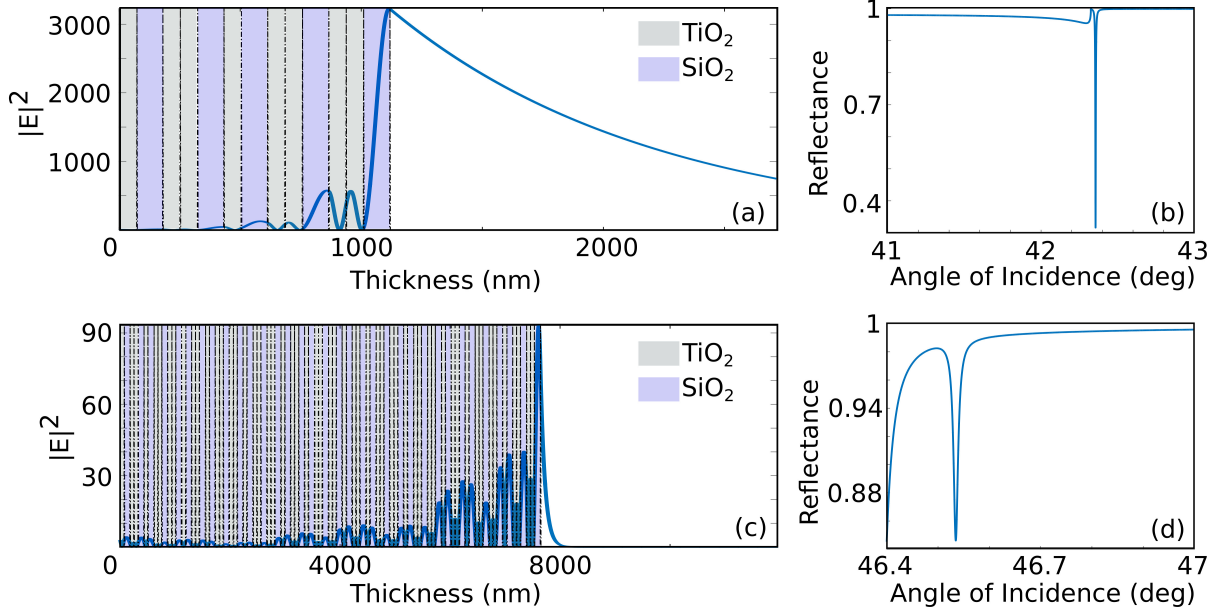


Figure 22: (a) BLSW assisted E-field intensity at the surface of a 13 layered FQC ($j = 5$) at $\lambda = 475$ nm and $\text{AoI} = 42.36^\circ$. (b) Corresponding reflectivity curve for $\lambda = 475$ nm. (c) BLSW assisted E-field intensity at the surface of a 89 layered FQC ($j = 9$) at $\lambda = 440$ nm and $\text{AoI} = 46.53^\circ$. (d) Corresponding reflectivity curve for $\lambda = 440$ nm.

axis given by

$$k_{BLSW} = \frac{2\pi}{\lambda_0} n_0 \sin(\theta_{BLSW}), \quad (252)$$

where k_{BLSW} is the parallel wave vector of BLSW, $n_0 = 1.5$ is the refractive index of the prism, and λ_0 and θ_{BLSW} are the free space wavelength and angle of incidence at the respective BLSW reflectivity minima extracted from the reflection map. We normalize the frequency axis by multiplying the angular frequency (ω) by $a/2\pi c$, where a is the thickness of a unit cell consisting of a TiO_2 and SiO_2 bilayer, and c is the speed of light. A similar normalization for the wave vector axis is accomplished by multiplying the parallel wave vector (k) by $a/2\pi$. The light green region is the radiative light cone in air, whereas the white region is the non-radiative region. The dotted vertical light line from Figure 21(a) is transformed into the solid black line that divide the radiative and non-radiative regions. It

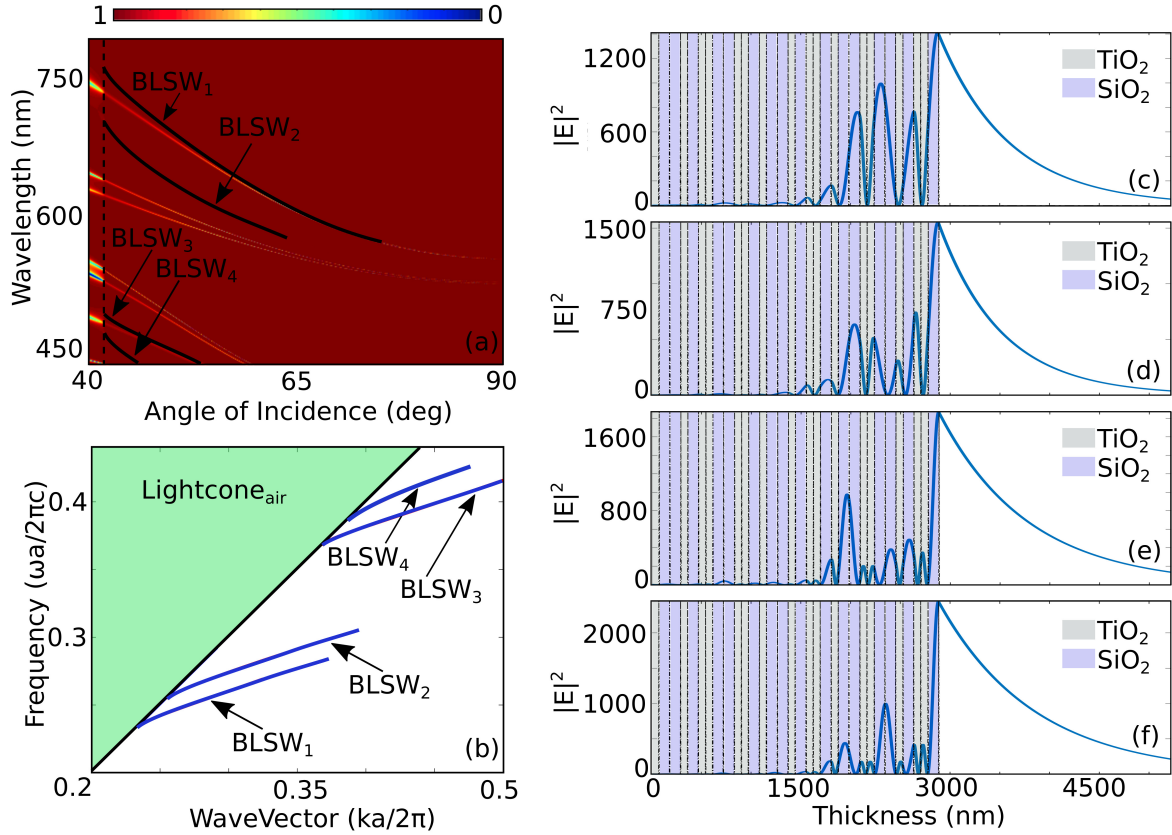


Figure 23: BLSWs in TMADM. (a) Reflection map of a 32 layered TMADM ($j = 5$) in contact with air as a function of λ and AoI. (b) Dispersion curves of BLSW₁, BLSW₂, BLSW₃ and BLSW₄. (c-f) BLSW assisted E-field intensity at the surface for (c) $\lambda = 762.4$ nm and AoI = 42° , (d) $\lambda = 701.4$ nm and AoI = 42.01° , (e) $\lambda = 488.1$ nm and AoI = 41.86° , (f) $\lambda = 465.1$ nm and AoI = 41.85° .

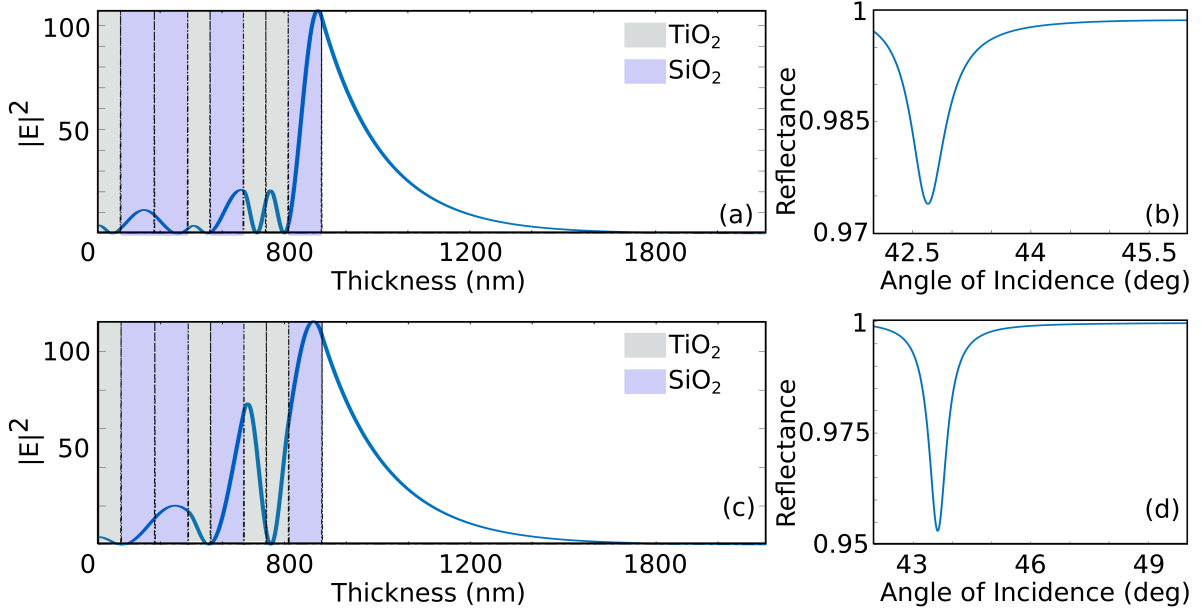


Figure 24: (a) BLSW assisted E-field intensity at the surface of a 8 layered TMADM ($j = 3$) at $\lambda = 460$ nm and $\text{AoI} = 42.46^\circ$. (b) Corresponding reflectivity curve for $\lambda = 460$ nm. (c) BLSW assisted E-field intensity at the surface of a 8 layered TMADM ($j = 3$) at $\lambda = 700$ nm and $\text{AoI} = 43.63^\circ$. (d) Corresponding reflectivity curve for $\lambda = 700$ nm.

is the dispersion line for light incident at the grazing angle along the multilayer surface in the absence of the prism. The solid blue curves represent the BLSW modes. As expected, they lie beyond the dispersion line for light. Although such modes are intrinsically present at dielectric-air interfaces, they are non-radiative in nature; their momentum is larger than the free-space wave momentum. Due to the momentum mismatch, BLSW modes cannot be excited directly by light incident from the air side. For this reason, we use a prism to couple light into the structure. The prism provides the additional momentum to the incident wave to excite BLSWs. Figure 21(c) and 21(d) show the E-field intensity ($|E|^2$) profiles, normalized to the incident E-field intensity ($|E_0|^2 = 1$), overlaid on top of their structure profiles corresponding to BLSW_2 and BLSW_1 respectively. The BLSW modes have highly confined E-field at the surface layer and exponentially decaying field profile

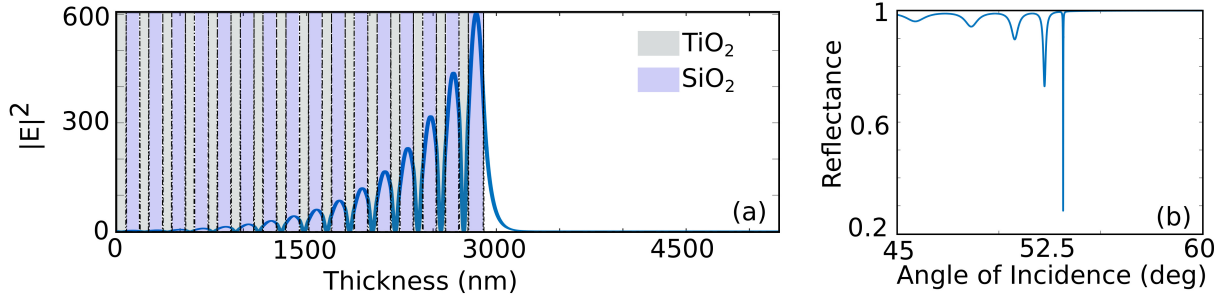


Figure 25: BSW assisted E-field intensity at the surface of a periodic counterpart (32 layers) of FQC and TMADM at wavelength 440 nm and incident angle 53.16° .

in the homogeneous analyte/superstrate layer. However, unlike the BSW modes, the field confinement of the BLSW modes inside the FQC is not necessarily tied to periodicity and thus they can have non-exponential decaying field profile inside the FQC. The E-field intensity in Figure 21(c) is observed for the incident angle of 45.67° at the wavelength 443.2 nm. The incident angle and wavelength for Figure 21(d) are 42.14° and 760 nm respectively. The plots demonstrate that the E-field intensity at the surface is magnified by $\sim 1500x$ and $\sim 100x$ for $BLSW_2$ and $BLSW_1$ respectively. Such high E-field intensity at the surface of multilayer structures is of great significance for fluorescence-based detection [14, 15, 20] and surface-enhanced Raman spectroscopy [29, 30]. Moreover, the plots also permit determination of the PD of the evanescent wave beyond the surface as 93 nm and 533 nm at the $\exp(-1)$ point. Figure 21(e) and 21(f) show the reflectivity dips for the respective BLSW excitations in Figure 21(c) and 21(d).

Figure 22 shows BLSWs in two additional generations of FQCs. Besides the number of layers, all other parameters of the FQCs are the same as in the 32 layered FQC. In Figure 22(a), we plot the BLSW assisted E-field enhancement superposed on a 13 layered ($j = 5$) FQC, and the corresponding reflectivity curve in plotted in Figure 22(b). The BLSW in this structure is excited for the wavelength 475 nm at the incident angle 42.36° . The E-field enhancement achieved for this FQC is larger than $3000x$, which is the largest field

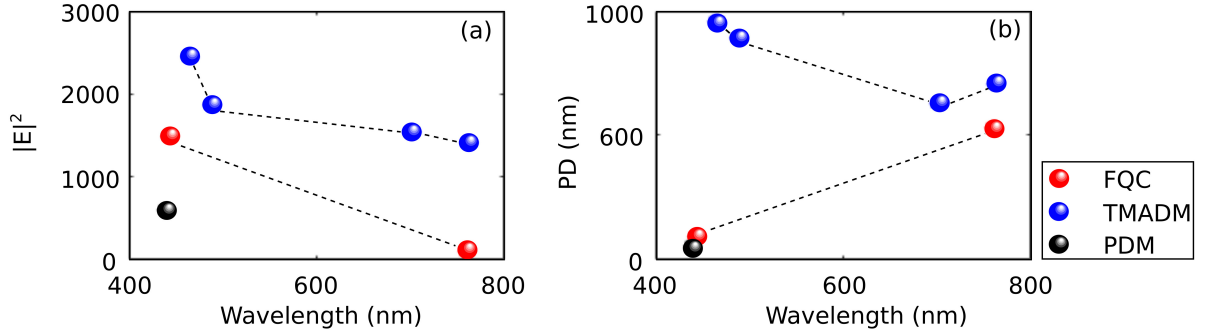


Figure 26: (a) Maximum E-field intensity at the surface of the 34 layered FQC (red circle), 32 layered TMADM (blue circle), and 32 layered PDM (black circle). (b) $\text{Exp}(-1)$ penetration depth beyond the surface of the FQC, TMADM, and PDM into the air side.

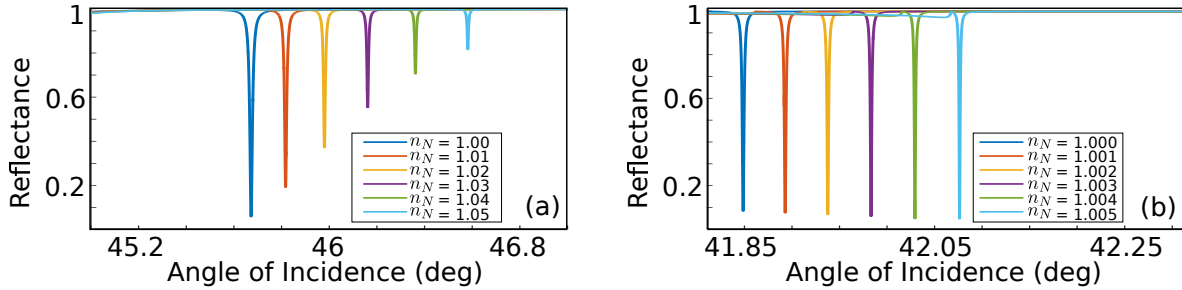


Figure 27: Reflectivity curves of (a) a FQC ($j = 7$) at $\lambda = 443.2$ nm (b) a TMADM ($j = 5$) at $\lambda = 465.1$ nm for different refractive indices n_N of superstrate layer.

enhancement that we predict in this paper. Similarly, Figure 22(c) and (d) shows the BLSW and the reflectivity curve of a 89 layered ($j = 9$) FQC respectively. The corresponding BLSW wavelength and incident angle are 440 nm and 46.53° . These results show that BLSWs can exist in different generations of FQC, ranging from lower to higher generations.

Figure 23(a) is the reflection map of a 32 layered TMADM. We observe four distinct BLSW modes, labeled as $\text{BLSW}_{1/2/3/4}$, lying beyond the light line; their dispersion curves are presented in Figure 23(b). The TMADM pattern for Thue-Morse order $j = 5$ is AB-BABAABBAABABBABAABABBAABBABAAB. The sequence can be sub-grouped in a

near-periodic form as $\mathbf{X}\mathbf{Y}\mathbf{X}\mathbf{Y}'\mathbf{X}\mathbf{Z}$, where $\mathbf{X} = \text{ABBAB}$, $\mathbf{Y} = \text{AABBAAB}$, $\mathbf{Y}' = \text{AABABBA}$, and $\mathbf{Z} = \text{AAB}$, with \mathbf{Z} acting as the surface defect. The sub-groups \mathbf{Y} and \mathbf{Y}' have the same first three components but the order of last four components are switched. The structure pattern and the $|\mathbf{E}|^2$ field profiles for the four distinct BLSW modes are shown in Figure 23(c)-23(f). The BLSW in Figure 23(c) is realized at the incident angle of 42° and wavelength 762.4 nm. The maximum E-field intensity at the surface and the $\exp(-1)$ PD obtained for this mode (BLSW₁) are $\sim 1410x$ and 710 nm respectively. The E-field intensity of $\sim 1550x$ and the PD of 630 nm are attained at the BLSW₂ mode in Figure 23(d) for the incident angle 42.01° and wavelength 701.4 nm. The E-field intensity and the PD for the BLSW₃ in Figure 23(e) at the incident angle 41.86° and wavelength 488.1 nm are $\sim 1870x$ and 894 nm respectively. Similarly, for the BLSW₄ at 41.85° and 465.1 nm [Figure 23(f)], the E-field intensity and the PD are $\sim 2450x$ and 960 nm respectively. The results presented here are based on an infinite plane wave approach. In real applications, the results will be modified because of finite beam spot size [29].

As in the case of FQCs, BLSWs only exist in different generations of TMADMs. Figure 24 shows two separate BLSW modes on a 8 layered ($j = 3$) TMADM. BLSW at the wavelength 460 nm and the incident angle 42.46° is shown in Figure 24(a), whereas the BLSW at the wavelength 700 nm and the incident angle 43.63° is shown in Figure 24(c). Their corresponding reflectivity curves are plotted in Figure 24(b) and (d) respectively.

The FQCs and TMADMs exhibit enhanced optical properties compared to their periodic counterparts [87]. To compare the surface E-field intensity and the $\exp(-1)$ PD obtained from the FQC ($j = 7$) and the TMADM ($j = 5$) with that from a PDM, we plot the $|\mathbf{E}|^2$ field profile of a 32 layered PDM in Figure 25(a), and the reflectivity curve in Figure 25(b). The PDM consists of alternating layers of TiO_2 and SiO_2 with thicknesses 71.9 nm and 108.4 nm respectively. The surface SiO_2 (defect layer) has a thickness of 120 nm. The BSW wavelength of 440 nm and the incident angle of 54.16° for Figure 25 are chosen such that the E-field intensity at the surface of the structure is the largest. For the results presented

in Figure 21, 22, and 23, we do not undergo any optimization. Optimizing the structure parameters, such as layer thicknesses, refractive indices, and number of layers can improve the results further.

The maximum surface E-field intensities of the BLSWs and the $\exp(-1)$ PD obtained for the FQC from Figure 21(c)-21(d) and from Figure 23(c)-23(f) for the TMADM, along with that for the PDM from Figure 25 are plotted in Figure 26(a) and 26(b). The PDM has only one BSW mode over the wavelength range of 430-800 nm, whereas the FQC and the TMADM have two and four BSW modes respectively, corresponding to the different number of data points for the PDM, FQC, and TMADM in Figure 26(a) and 26(b). For the PDM, the maximum E-field intensity at the surface is $\sim 600x$, which is low compared to the amplifications of up-to 1495 and 2450 obtained in the FQC and the TMADM respectively. The evanescent tail extending to the air side beyond the PDM surface has the $\exp(-1)$ PD equal to 55.45 nm, whereas the PD for the FQC and the TMADM are 533 nm and 961 nm respectively. We emphasize that this comparison is not comprehensive because we fix the number of layers and the thicknesses of the PDM to be the same as that of the TMADM, and that the structures are not optimized. The increased PD for the FQC and the TMADM results from BSW resonances near the total internal reflection (TIR) angle. The angle of incidence sets the real part of the k_{BSW} and determines the PD as given by $1/\text{PD} \sim (k_{BSW}^2 - k_{air}^2)^{1/2}$. A comparable PD for the PDM can be obtained for BSW resonances near the TIR angle, however for the PDM considered here, we do not observe BSW near the TIR angle. In general, shifting the BSW/BLSW resonance towards the TIR angle increases the PD of these resonances.

Finally, we also explore the angular sensitivity of BLSW in a 34 layered FQC and a 32 layered TMADM. We note that the sensitivity analysis presented here is in no way comprehensive; we plan to do a detailed study in our future work. Figure 27(a) shows reflectivity curves of BLSW_2 (see Figure 21) for the wavelength 443.2 nm for different refractive indices (n_N) of the superstrate/analyte layer. The maximum angular sensitivity obtained from Fig-

ure 27(a) is $22^\circ/\text{RIU}$. The angular sensitivity of biosensors is defined as the change in the angle of BSW/BLSW excitation with respect to the change in the refractive index given by

$$\text{Angular sensitivity} = \frac{\Delta\theta_{BSW/BLSW}}{\Delta n_N}, \quad (253)$$

and is measured in refractive index units (RIU). The reflectivity curves of BLSW₄ (see Figure 23) for the wavelength 465.1 nm for different n_N is shown in Figure 27(b). We observe the maximum angular sensitivity of $50^\circ/\text{RIU}$, which is typical for biosensors based on BSW.

4.4 Summary

We demonstrate the excitation of BLSWs in different generations of FQCs and TMADMs. Although these structures are not periodic, their components can be sub-grouped to obtain some superficial periodicity, which can potentially explain the excitation of BLSWs in these structures. These systems possess several advantages over the periodic counterparts. The surface E-field intensity is highly enhanced and the $\exp(-1)$ penetration depth in the air side beyond the surface is strongly extended. We envision the applications of these enhanced properties in making better slow light devices and highly sensitive BLSW assisted biosensors for antibody-antigen binding and analyte refractive index change detections, and enhanced surface non-linear optical phenomena such as Raman Spectroscopy.

CHAPTER 5

SENSITIVITY ENHANCEMENT VIA SLOW BLOCH SURFACE WAVE IN MAXIMAL LENGTH SEQUENCE MULTILAYERS

5.1 Introduction

Recently, Bloch surface waves have emerged as an attractive alternative to Surface plasmon polaritons (SPP) for biosensing applications [14,15,18,20,23–25]. Bloch surface waves (BSW) are a surface electromagnetic excitation that exists at the interface between an optically active composite and a homogeneous dielectric. BSWs are a superior choice for two related reasons. First, BSWs exist on the surface of dielectric multilayer structures, which have low loss as compared to metal used for SPP. Second, this low loss results in a BSW resonance that has a higher Q-factor than SPP resonance. This sharp resonant phenomena can be used to detect small surface variations [10]. Moreover, BSW can be excited at any wavelength by suitably changing the refractive index and thicknesses of the dielectric materials in the multilayer structure. This flexibility in the case of metals is limited.

BSWs are non-radiative electromagnetic modes [7,8], i. e., they do not exist in free space on their own. The BSW wavevector is longer compared to the free space wavevector at a given frequency. Thus, we need to provide an additional momentum to the wavevector of the incident wave so that it can satisfy the phase matching condition with the BSW wavevector. This task is usually accomplished by prism coupling technique, either using Kretschmann configuration [12] or Otto configuration [11]. In this paper, we mainly use the Kretschmann configuration, and later demonstrate that BSWs can also be excited using the Otto configuration. In the Kretschmann configuration, as shown in Figure 28(a), the multilayer structure is deposited on top of a prism, whereas in Otto configuration [see Figure 28(b)], there is an air-gap between the multilayer and the prism.

BSWs have been extensively studied. Researchers have used different variations of pe-

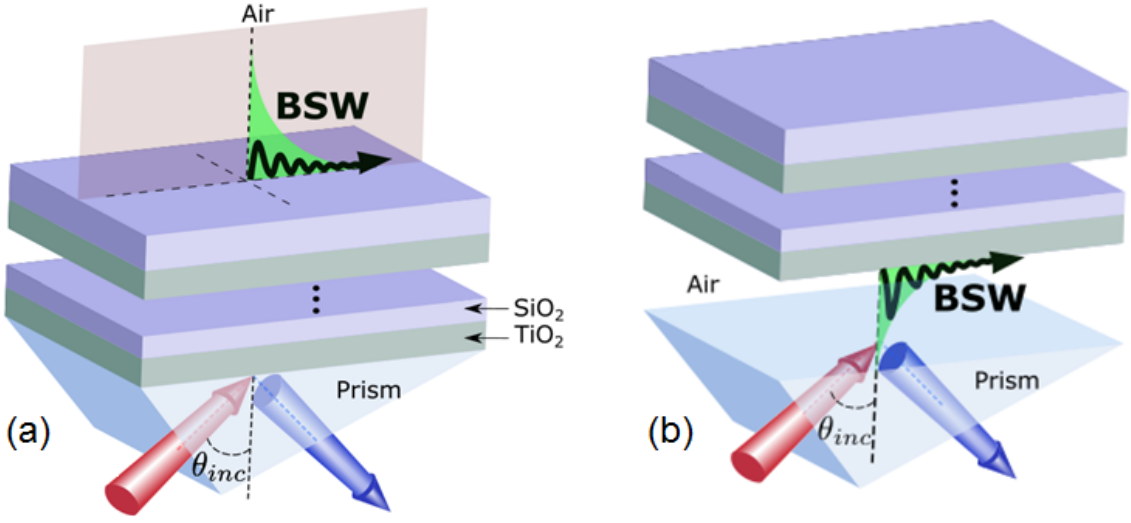


Figure 28: A schematic of a prism coupling technique (Kretschmann configuration) to excite Bloch surface wave using a dielectric multilayer.

periodic multilayers that support BSWs [99, 124, 125]. Almost all the studies however, only use perfectly periodic multilayer structures with a surface defect. In our previous study, we showed that BSWs can also be excited in Fibonacci quasi-crystals and Thue-Morse aperiodic multilayer structures [88, 89]. Using quasi-crystals and aperiodic multilayers have advantages of their own. They provide engineering design flexibility, and better performance in some cases. In this paper, we propose a new type of aperiodic multilayer structure known as Maximal-length sequence (MLS) multilayers. MLS is a pseudo random sequence, which is widely used in electrical engineering for signal processing and in acoustics to design walls that help reduce sound reflections [126]. MLS is generated using the following recursion formula

$$S_{k+3} = S_k \oplus S_{k+2}, \quad (254)$$

where \oplus denotes an XOR (modulo-2 sum) operation. Some examples of MLS are given in Table 1.

In this work we consider TiO₂ (A) and SiO₂ (B) as the high and low refractive index

Table 2: Maximal-length sequence examples

Generation (S_j)	MLS
S_3	AAABBAB
S_4	AAAABBBABBAABAB
S_5	AAAAABBBBAABAAABABABBBBABBABAABB

materials. We consider the wavelength (λ) dependent refractive index of both TiO₂ [101] and SiO₂ [102] over the range of 1.1 μm to 1.55 μm given by

$$n_{\text{TiO}_2} = \sqrt{5.913 + \frac{0.2441}{\lambda^2 - 0.0803}}, \quad (255)$$

and

$$n_{\text{SiO}_2} = \sqrt{1 + \frac{0.6961663\lambda^2}{\lambda^2 - 0.0684043^2} + \frac{0.4079462\lambda^2}{\lambda^2 - 0.1162414^2} + \frac{0.8974794\lambda^2}{\lambda^2 - 9.896161^2}} \quad (256)$$

respectively. In the rest of the paper however, λ is given in nm. We also introduce small losses in these materials through the imaginary parts of their refractive indices. The values used here, 0.00016 and 0.000034 for TiO₂ and SiO₂ respectively, are based on the published sources [103, 104] and are selected to match with experimental investigations of BSWs [10, 18, 23].

5.2 Results and Discussions

Figure 29(a)-29(f) shows reflection maps of a MLS multilayer (S_5) structure for different values of superstrate refractive index. We add one additional layer of TiO₂ with the same thickness as of the first layer. Thus, the MLS sequence used in this paper is

AAAAABBBBAABAAABABABBBBABBABAABBAAAAA. The thickness of TiO₂ (A) is 230 nm and SiO₂ (B) is 503 nm. For all superstrate refractive indices, we observe BSW-like modes at wavelengths in the range of 1100 nm - 1300 nm. The vertical dashed lines are the lightlines for their respective superstrate refractive index. For high superstrate refractive index, the lightline shifts to the higher angular position. Thus, the BSW excitation angles for any particular wavelength are larger for higher superstrate refractive index. In this paper, we only consider the reflection maps of electric field waves in transverse-electric mode. The reflection maps, along with all other results in this paper, are computed from an iterative

implementation of Fresnel's equations as a function of angle of incidence and wavelength. The electric field profile inside the multilayer structure is computed by solving for the field iteratively imposing the continuity of electric field and its derivatives at the interfaces of the multilayer structure (refer [89] for details).

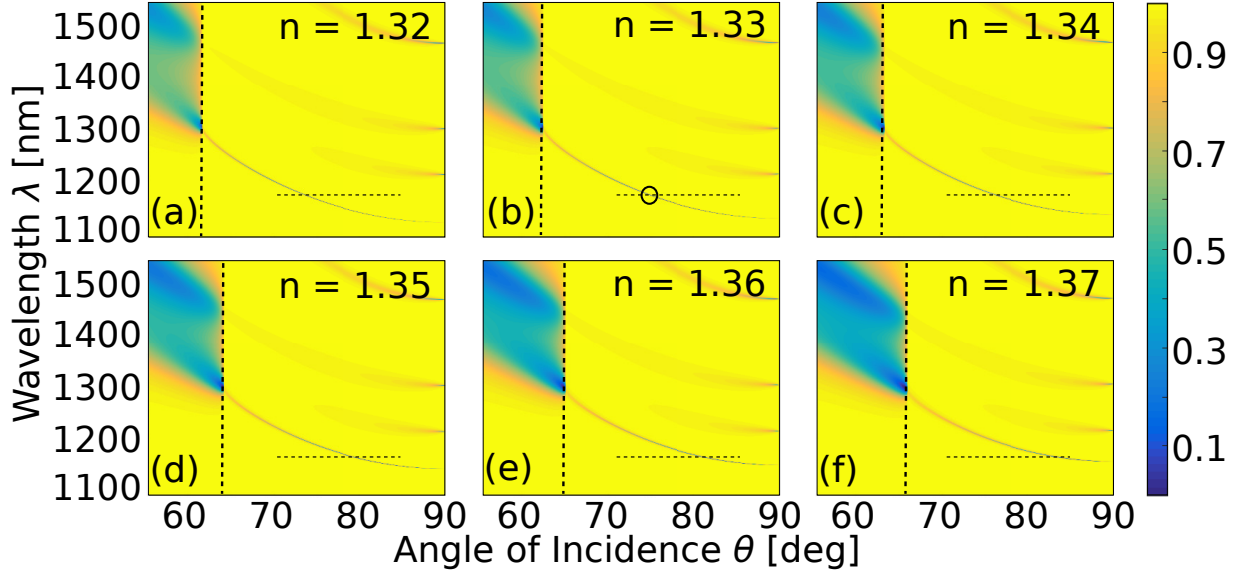


Figure 29: Reflection maps of a 36-layered maximal length sequence multilayer over a wavelength range of 1115nm-1295nm and incident angle range of 66° - 85° for superstrate indices (a) 1.32, (b) 1.33, (c) 1.34, (d) 1.35, (e) 1.36, and (f) 1.37. Shift in the BSW mode as a function of superstrate index is clearly observed. The dotted lines represent the cross-sections of the reflection map plotted in Figure 30(a), and the solid circle in (b) is the wavelength-angle pair for the field enhancement plot shown in Figure 30(b).

The dotted horizontal lines in Figure 29(a)-29(f) at the wavelength of 1159.88 nm and angular range 70° - 85° are plotted as reflectivity curves in Fig 3(a). We observe sharp and narrow BSW resonances for different values of superstrate refractive indices. One important feature that we can observe here is that as the superstrate refractive index value increases, the angular displacement between the BSW resonances increases as well. This has an important

implication in increasing the angular sensitivity of the system. The figure of merit (FOM) of the resonances however, decrease for higher superstrate refractive indices, as illustrated in Figure 30(a) with dark red solid line (right-axis). The FOM [127] of the BSW resonances are defined as

$$\text{FOM} = \frac{S_{\text{ideal}}(1 - R)}{\text{FWHM}}, \quad (257)$$

where S_{ideal} is the average angular sensitivity of the BSW resonances, R is the reflectance at θ and FWHM is the full-width of the resonance dip at half-maximum. The higher the FOM, i. e., the deeper and narrower the BSW resonances are, the higher the accuracy to detect the refractive index of analyte by the angular displacements. BSWs also create amplified electric field intensity at the surface of the multilayer structure with evanescent decaying fields on the either side of the surface. The amplified electric field intensity for the superstrate refractive index of 1.33 at the wavelength of 1159.88 nm and incident angle of 77.07° is shown in Figure 30(b). The normalized electric field intensity at the surface of the structure is 250x greater than the input incident field.

The angular sensitivity of MLS multilayer structure is illustrated in detail in Figure 31. It is defined as

$$S_\theta = \frac{\Delta\theta}{\Delta n}, \quad (258)$$

where $\Delta\theta$ is the change in angular position of BSW resonances and Δn is the change in superstrate refractive index. BSW modes as a function of θ and wavelength for different values of superstrate refractive index is shown in Figure 31(a). The range of superstrate refractive index investigated is 1.32-1.37. The angular sensitivity, as defined by Eqn. (258), is plotted in Figure 31(b). For clarity, only the greatest and least sensitivity curves are plotted. The remaining sensitivity curves lie in between these two curves. As can be seen clearly, the maximum sensitivity obtained is greater than 250 deg/RIU. The reported angular sensitivity is significantly higher than that observed in several other studies [19, 128, 129]. Typically, angular sensitivity of BSWs lie in the range of 50-150 deg/RIU. The enhanced sensitivity is achieved here by using porous TiO_2 on the top layer. Detailed explanation of

depositing porous TiO_2 is explained elsewhere [130, 131]. The use of porous TiO_2 enables us in dynamically modulating the refractive index of the corresponding layer by altering the refractive index of the superstrate layer. Here we change the refractive index of the top TiO_2 layer by 0.01 for the refractive index change of 0.01 in the superstrate layer.

Sensitivity of BSW can also be measured in terms of wavelength, as defined by

$$S_\lambda = \frac{\Delta\lambda}{\Delta n}, \quad (259)$$

where $\Delta\lambda$ is the change in spectral position of BSW resonances and Δn is the change in superstrate refractive index. To explore spectral sensitivity of the MLS multilayer structure, we plot BSW modes as a function of wavelength and incident angle as shown in Figure 32(a) for a range of superstrate refractive index values. From these curves, we can extract the spectral sensitivity using Eqn. (259), which is shown in Figure 32(b). For clarity, we only plot the results for the maximum and minimum sensitivities. We observe spectral sensitivity higher than 1600 nm/RIU, which is again a significant improvement compared to previously reported results [19, 124].

The overall improvement in sensitivity of BSWs, both in angular and spectral regimes, can also be understood by looking at their dispersion curves. BSW dispersion curves, plotted as a function of frequency and wavevector [see Figure 33(a)], shed invaluable insights on the characteristics of BSWs. We apply coordinate transformation of the incidence angle axis in Figure 29(a)-29(f) as given by

$$k_{\text{BSW}} = \frac{2\pi}{\lambda_0} n_0 \sin(\theta_{\text{BSW}}), \quad (260)$$

where k_{BSW} is the parallel wavevector of BSW, $n_0 = 1.5$ is the refractive index of the prism, and λ_0 and θ_{BSW} are the free space wavelength and angle of incidence at the respective BSW reflectivity minima. The dashed line in Figure 33(a) is the light line for the superstrate refractive index of 1.32. The corresponding dispersion curve lies beyond this light line, which indicates that BSWs are non-radiative modes. Thus, they cannot be excited directly from free space. The light line for the remaining superstrate refractive indices are not shown in

the figure but they show the same behavior as well. This is the reason we employ prism coupling technique to excite BSWs on dielectric multilayer surfaces. Moreover, dispersion curves can also be used to compute group velocity (v_g) of BSWs, which is defined as

$$v_g = \frac{\partial \omega}{\partial k}, \quad (261)$$

where ω is angular frequency and k is wavevector. Group velocities of BSW modes in Figure 33(a) are shown in Figure 33(b). We can notice a striking characteristic of BSWs looking at their group velocity. The group velocities are less than the actual speed of light in their corresponding medium. Thus, BSWs travel slower on the surface of dielectric multilayer structures, which increases their interaction time with the analyte. This increased interaction hence, enhances the sensitivity of BSWs.

The results presented so far are based on the Kretschmann configuration, which is one of the most popular and widely used techniques used to excite BSWs. However, researchers also use another technique known as the Otto configuration [see Figure 28(b)] for sensing purposes via BSWs [25]. In the remaining of this paper, we demonstrate that BSWs in MLS multilayer can be excited using the Otto configuration as well. The main difference between the Kretschmann and Otto configuration is the air-gap between the multilayer structure and the prism in the Otto configuration. We use a high refractive index prism ($n_{prism} = 2.1252$) and a 31 layered MLS given as *BBAABABBABBBBABABAAABAABBBA*. The refractive indices of the high and low index materials used here are however different than those used in previous results. The refractive index of the low (*B*) and the high (*A*) index materials are $1.36 + 0.000037i$ and $2.15 + 0.00016i$ respectively and the refractive index of the substrate layer (Silicon) is 3.5. The reason for choosing these refractive indices is their easy fabrication using porous silicon on silicon substrate [25]. The layer thicknesses of *B* and *A* are 380 and 210 nm respectively. The air gap thickness is 1000 nm. The results of BSW excitation in a 31 layered MLS multilayer are shown in Figure 34(a) and 34(b). As in the reflectivity curves from the Kretschmann configuration, we observe a sharp and narrow dip in the reflectivity curve from the Otto configuration as shown in Figure 34(a). Similarly, the

electric field intensity at the surface layer is highly amplified as well, which is a characteristic of BSWs.

5.3 Summary

We propose a new type of pseudo-random sequence based MLS multilayer structure for generating BSWs. We numerically show that it can be used for making highly sensitive biosensors to detect refractive index changes, both in angular and spectral regimes. We report angular sensitivity higher than 250 deg/RIU and spectral sensitivity higher than 1600 nm/RIU. These results are significantly better than the previously reported results in the literature. The enhancement in sensitivity is attributed to slow BSWs on the surface of MLS multilayer structure, which increases the interaction time of BSWs with the superstrate analyte. The use of porous TiO_2 as the material for the top-most layer of the structure also further aids in improving the sensitivity. Finally, we demonstrate that BSWs in MLS multilayers can also be excited using the Otto configuration.

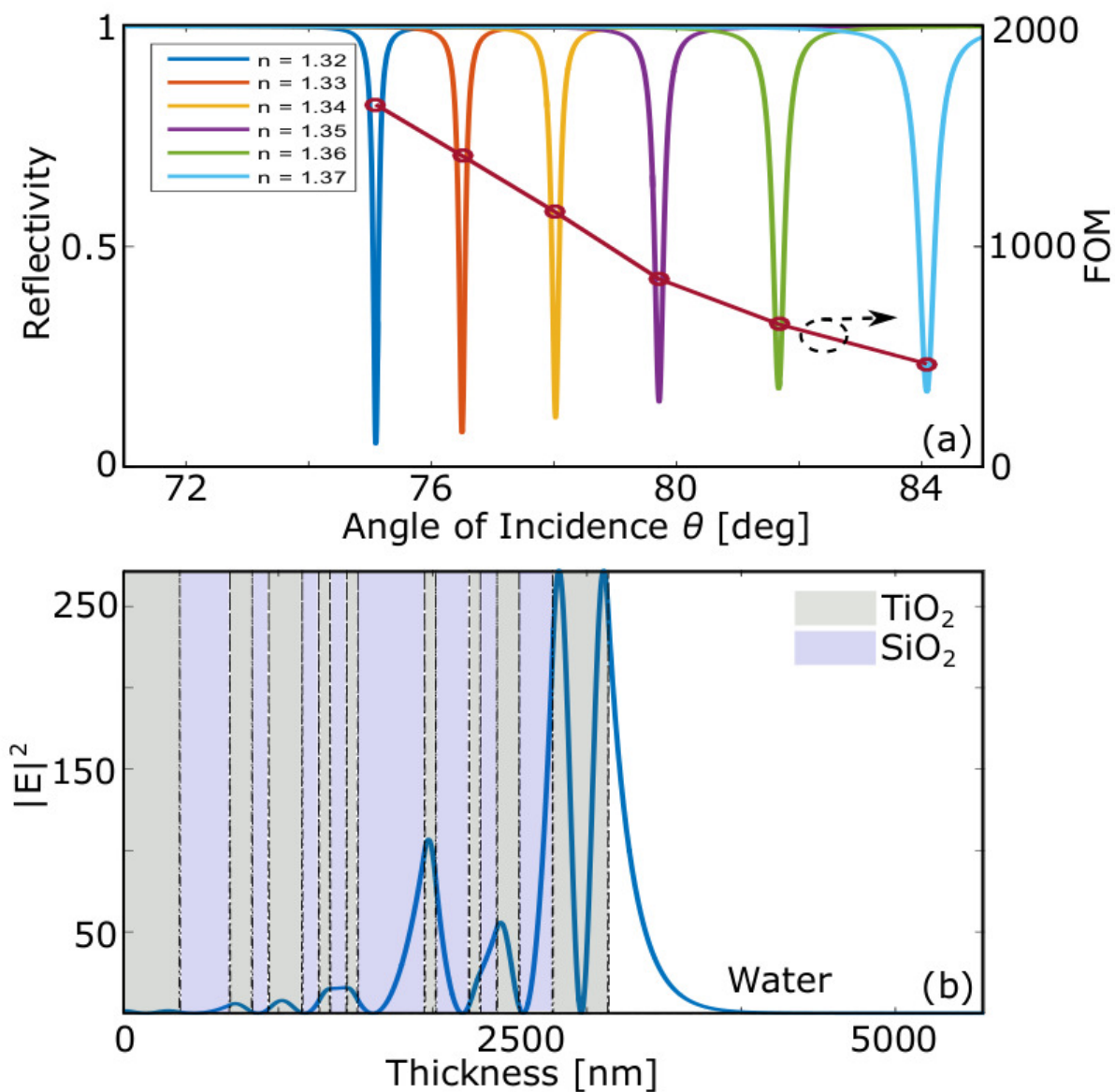


Figure 30: (a) Reflectivity curves of a 36-layered maximal length sequence multilayer at the wavelength 1159.88 nm and over the incident angle range of 72° - 85° for different superstrate indices. The red solid circles connected by solid lines represent the figure of merit for the respective BSWs. (b) Electric field enhancement at the wavelength 1159.88 nm and incident angle 77.07° .

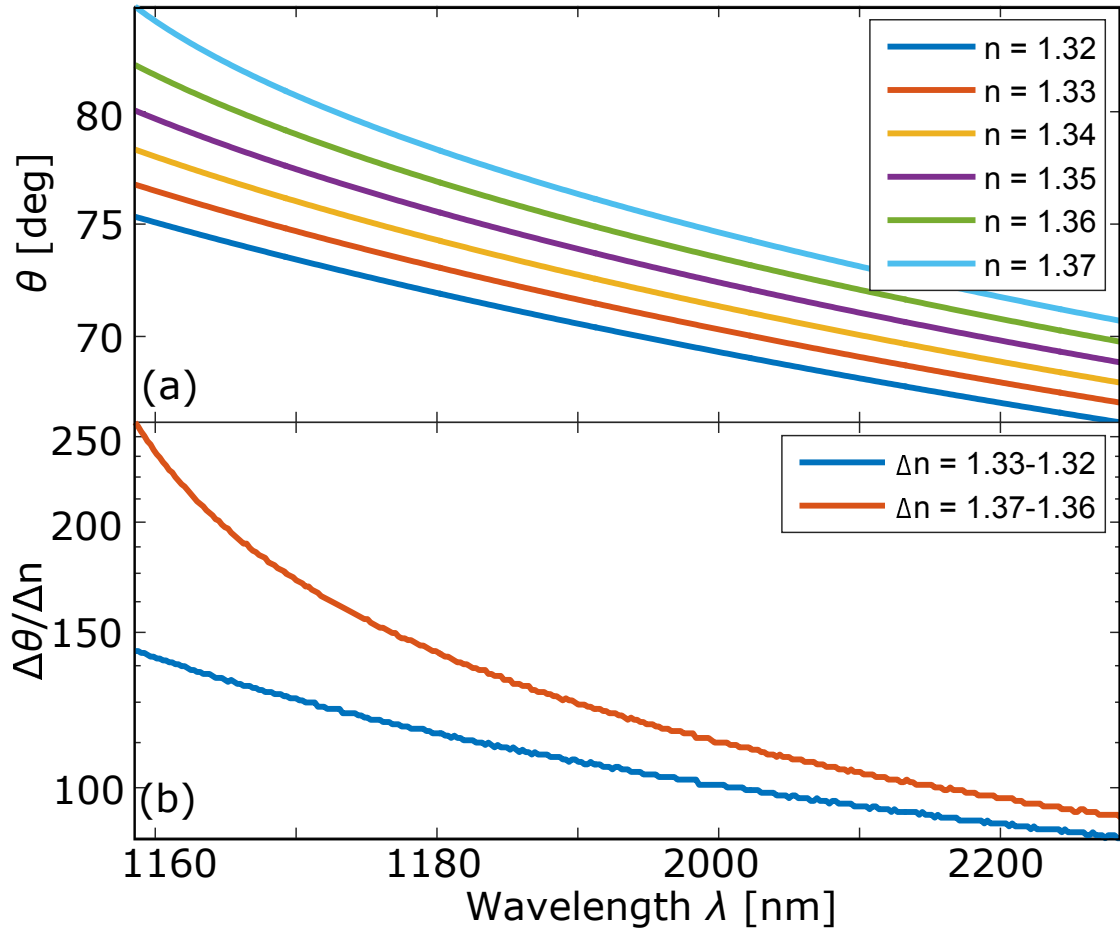


Figure 31: (a) Angular, and (b) spectral sensitivity of a 36-layered maximal length sequence multilayer for different superstrate refractive index changes.

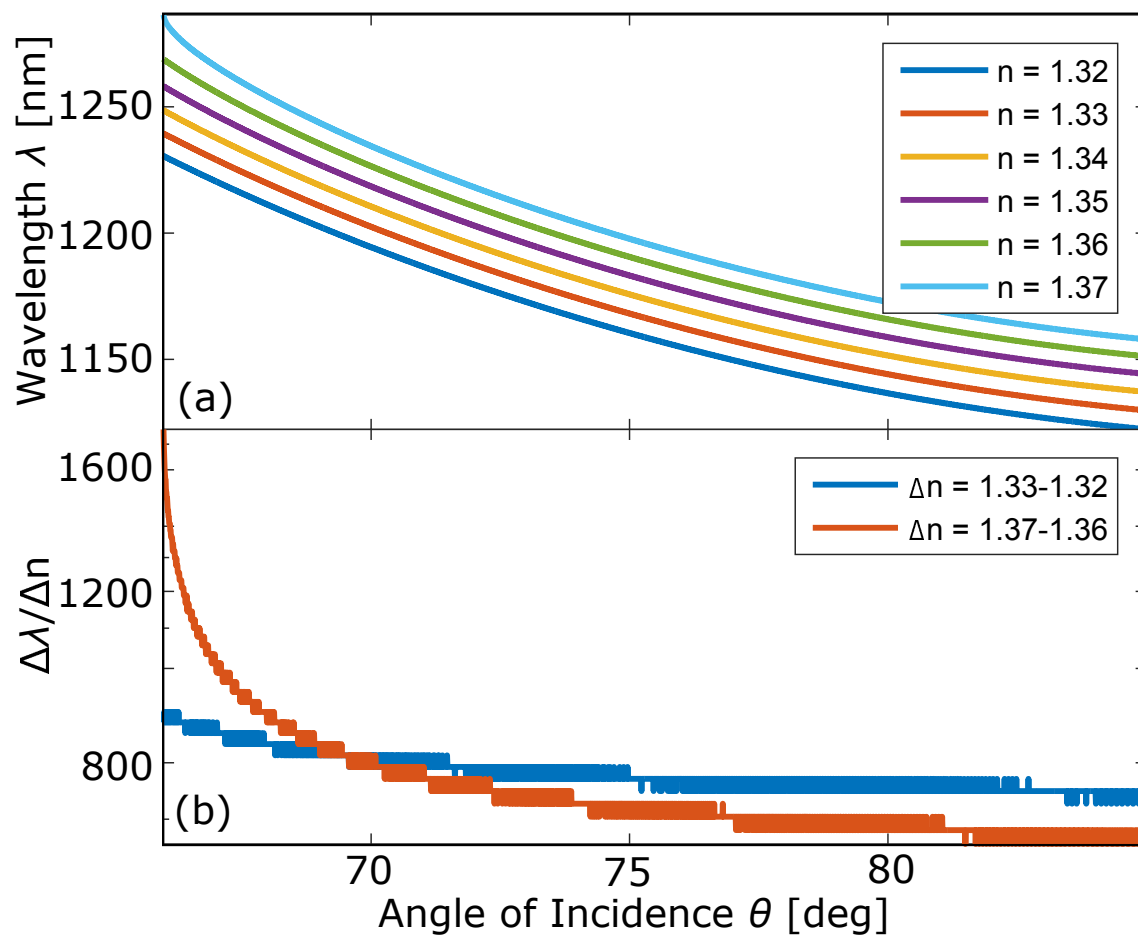


Figure 32: (a) Angular, and (b) spectral sensitivity of a 36-layered maximal length sequence multilayer for different superstrate refractive index changes.

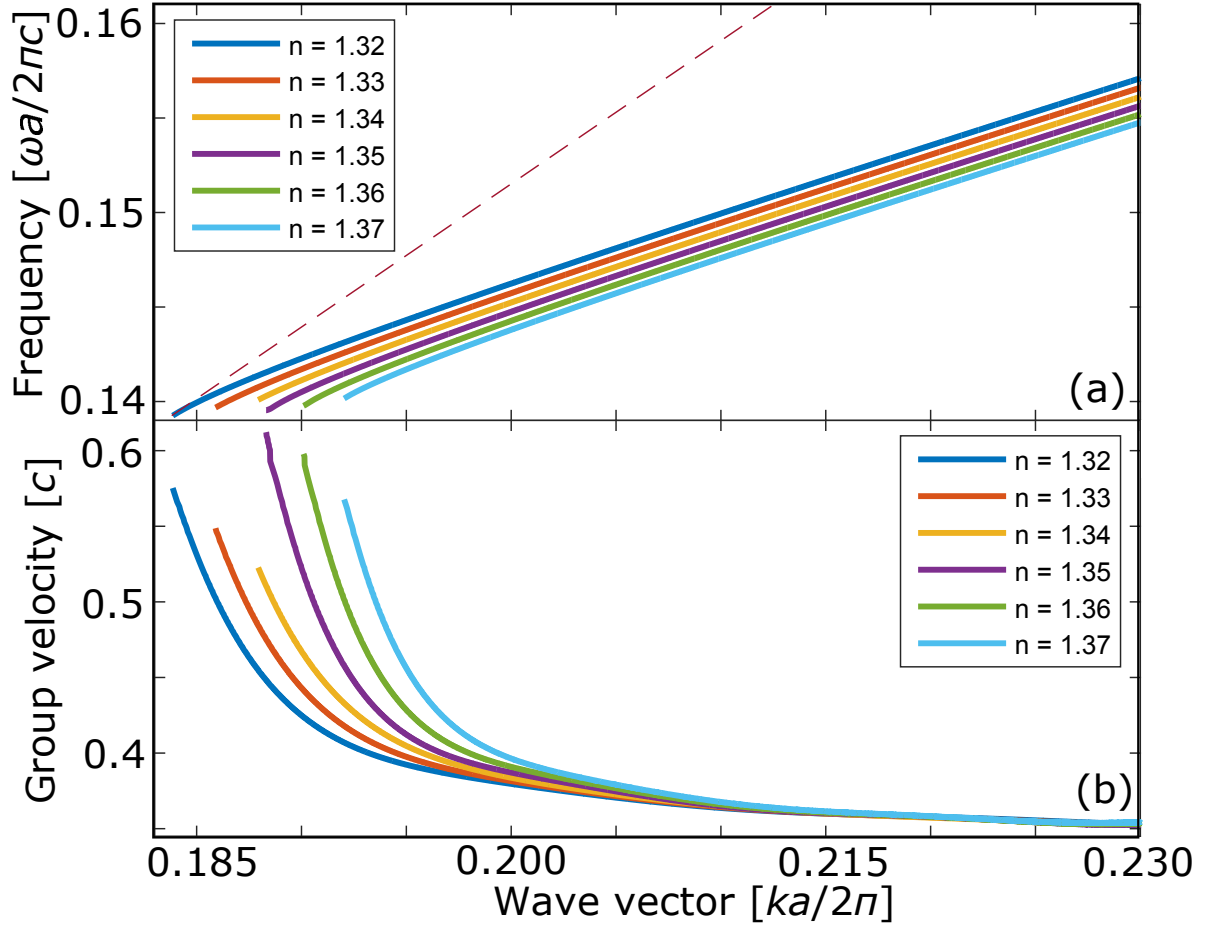


Figure 33: (a) Dispersion curves of the BSWs extracted from the reflection maps (Figure 28) using coordinate transformation of the incident angle axis to a parallel wave vector axis. The dotted lines represent the light lines for respective superstrate refractive indices. (b) Group velocities for the dispersion curves

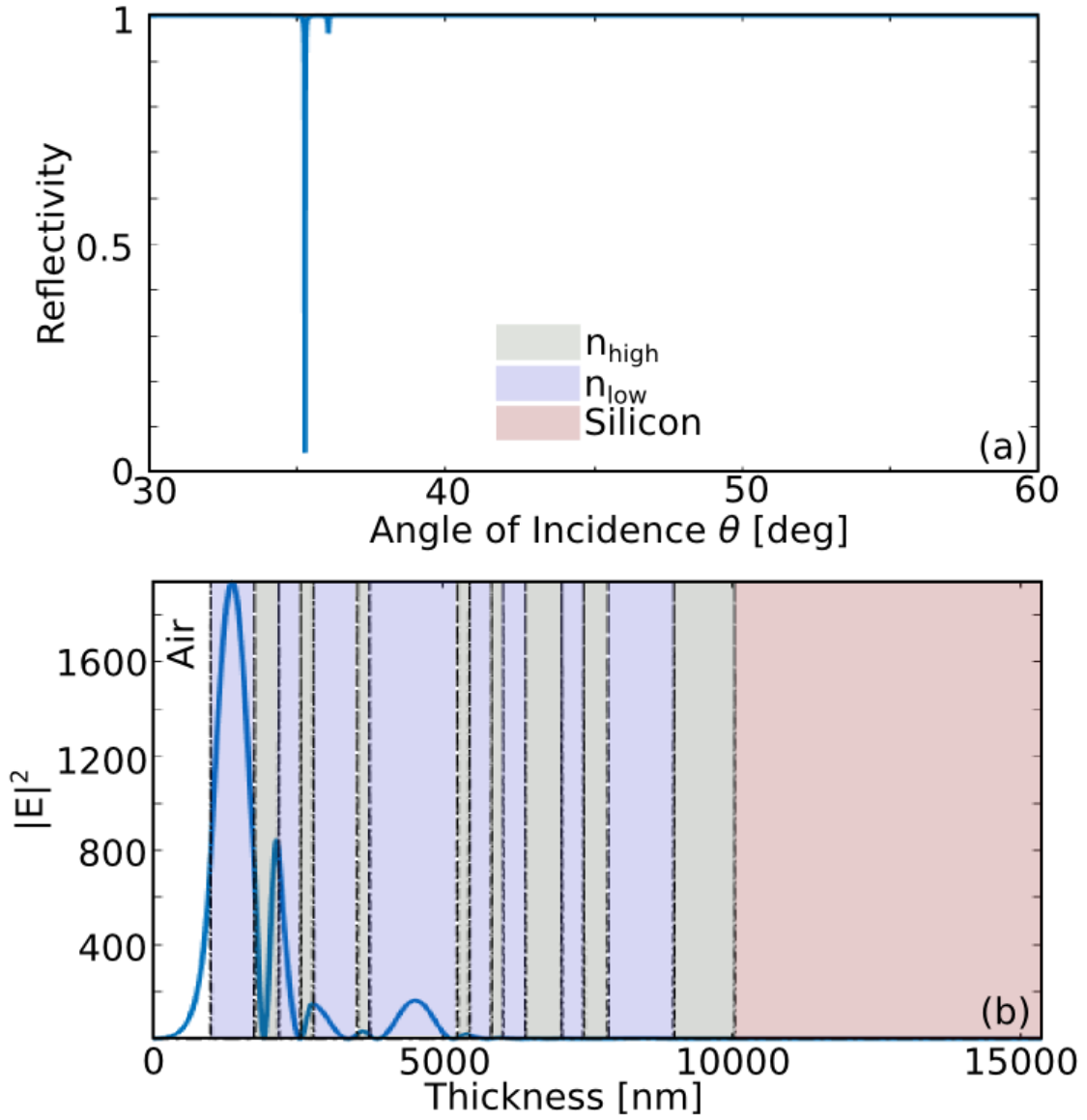


Figure 34: (a) Reflectivity curve (b) Electric field profile of a 31 layered maximal-length sequence multilayer using Otto configuration.

CHAPTER 6

**LEAKY BLOCH-LIKE SURFACE WAVES IN THE
RADIATION-CONTINUUM FOR SENSITIVITY ENHANCED
BIOSENSORS VIA AZIMUTHAL INTERROGATION**

6.1 Introduction

Bloch surface waves (BSW) are electromagnetic modes propagating at the interface of truncated dielectric multilayer structures and a homogeneous medium. The resonant generation of these modes via prism or grating coupling is an active field of research at present. Following the prediction [7] and experimental observation [8] of BSWs in photonic crystals, these modes have been studied, both theoretically and experimentally, in various configurations [9,10,25,88]. The resulting strong field/energy localization at the surface layer and the evanescently extending field in the homogeneous medium are of interest in applications such as label-free biosensing based on enhanced diffraction [24,99,100], surface-enhanced Raman spectroscopy [29,30], spectral and angular resonance shift [18,19,22,23,132], fluorescence-based detection [14,15,20], slow light enhanced nonlinear effects [71,72] and optical slow light devices and sensors [17,26]. BSWs are evanescent in nature, i.e., they are perfectly bound non-radiative states that lie below the light line of the homogeneous layer material. However, it was recently shown that if the surface layer is periodically corrugated and the dielectric constant of the dielectric medium is real, positive, and large, it can support a leaky BSW [107]. Such leaky modes still lie below the light line of the homogeneous layer material but fall above that of the dielectric multilayer material. As a result, this leaky BSW is bound to the surface in the homogeneous region but is radiative into the dielectric multilayer. Moreover, under appropriate conditions, it is possible to excite photonic surface states inside the radiation continuum [108–110]. Although these states are radiative into the homogeneous medium, they can have a long lifetime assisted by destructive interference between different

leakage channels. Such leaky-mode resonances with moderate to infinitely high Quality factor (Q) that confine freely propagating electromagnetic waves at a periodically modulated surface are of interest in applications such as lossless mirrors [111], high-performance optical filters [112], label-free biosensors [113], dielectric metasurfaces [114, 115], dielectric-based optical magnetism [116], and many others [117, 118].

In this paper, we show that moderate Q leaky BSWs on a dielectric multilayer surface with periodic corrugation can be used to significantly enhance the sensitivity of biosensors. To enhance the sensitivity we take advantage of the fact that the periodic corrugation of the surface layer allows us an additional degree of freedom over the azimuthal angle of the incident beam, which is not possible on a planar uncorrugated surface. In an experimental setup, this additional degree of freedom can be accessed by rotating the multilayer platform itself azimuthally. To our best knowledge however, little has been done in this regards [119, 120]. Previous related studies were done on surface plasmon polaritons (SPPs) – electromagnetic modes propagating at the interface of a metal and a dielectric medium – where the reflectivity is measured by fixing the azimuthal angle to a certain value followed by the conventional polar incident angle sweep. Here we propose a new technique of sensing using leaky BSWs, wherein we fix the polar incident angle to a specific value that excites a leaky BSW and then sweep over the azimuthal angle. The advantages of this technique are two fold. First, it mitigates the requirement of a bulky prism to excite BSWs and thus opens a prospect to engineer nanoscale lab-on-chip biosensors. Second, it can be used to make polarization independent biosensors, due to the fact that linear grating profile facilitates polarization conversion [121–123].

6.2 Computational Method

A schematic of the computational setup considered in this study is shown in Figure 35 We use a sixteen layered TiO_2 - SiO_2 multilayer on a SiO_2 substrate. The grating profile on the surface SiO_2 layer is SiO_2 as well. We consider wavelength (λ) dependent refractive index of

both TiO₂ [101] and SiO₂ [102] over the range of 0.43 μm to 0.8 μm given by

$$n_{\text{TiO}_2} = \left(5.913 + \frac{0.2441}{\lambda^2 - 0.0803} \right)^{\frac{1}{2}} \quad (262)$$

and

$$n_{\text{SiO}_2} = \left(1 + \frac{0.6962\lambda^2}{\lambda^2 - 0.0684^2} + \frac{0.4080\lambda^2}{\lambda^2 - 0.1162^2} + \frac{0.8975\lambda^2}{\lambda^2 - 9.8962^2} \right)^{\frac{1}{2}} \quad (263)$$

respectively. In the rest of the paper however, λ is given in nm. The thicknesses of TiO₂ and SiO₂ layers are 126.13 nm and 205.41 nm respectively. The excitation and confinement of BSWs on the surface of one dimensional (1D) photonic crystals is highly sensitive to the thickness of the surface defect layer due to the effects of multiple reflections from the periodic dielectric multilayer beneath [1]. For this reason, we set the thickness of the top SiO₂ layer to 280.03 nm. The grating height is set to 70 nm with a fill factor of $0.5a$, where a is the grating period set to 510 nm. The refractive index of the superstrate layer (n_{sup}) considered in our study is 1.26-1.4. The polar incident angle (θ_{inc}) is measured relative to the surface normal, while the azimuthal angle (ϕ) is measured with respect to the plane perpendicular to the grating profile.

We use an in-house three-dimensional (3D) scattering matrix based rigorous coupled wave analysis (SMRCWA) method to simulate the electric/magnetic field distribution in the computational domain containing the multilayer structure, the SiO₂ substrate, and the superstrate. The incident electric and magnetic field are expressed in their Fourier expansion as

$$\mathbf{E}(x, y, z) = \sum_{m=-\infty}^{\infty} \sum_{n=-\infty}^{\infty} \mathbf{S}_{m,n}(z) e^{-j(k_{x,m}x + k_{y,n}y)} \quad (264)$$

$$\mathbf{H}(x, y, z) = \sum_{m=-\infty}^{\infty} \sum_{n=-\infty}^{\infty} \mathbf{U}_{m,n}(z) e^{-j(k_{x,m}x + k_{y,n}y)}, \quad (265)$$

where

$$k_{x,m} = k_{x,\text{inc}} - \frac{2\pi m}{\Lambda_x}, \quad m = -\infty, \dots, -2, -1, 0, 1, 2, \dots, \infty \quad (266)$$

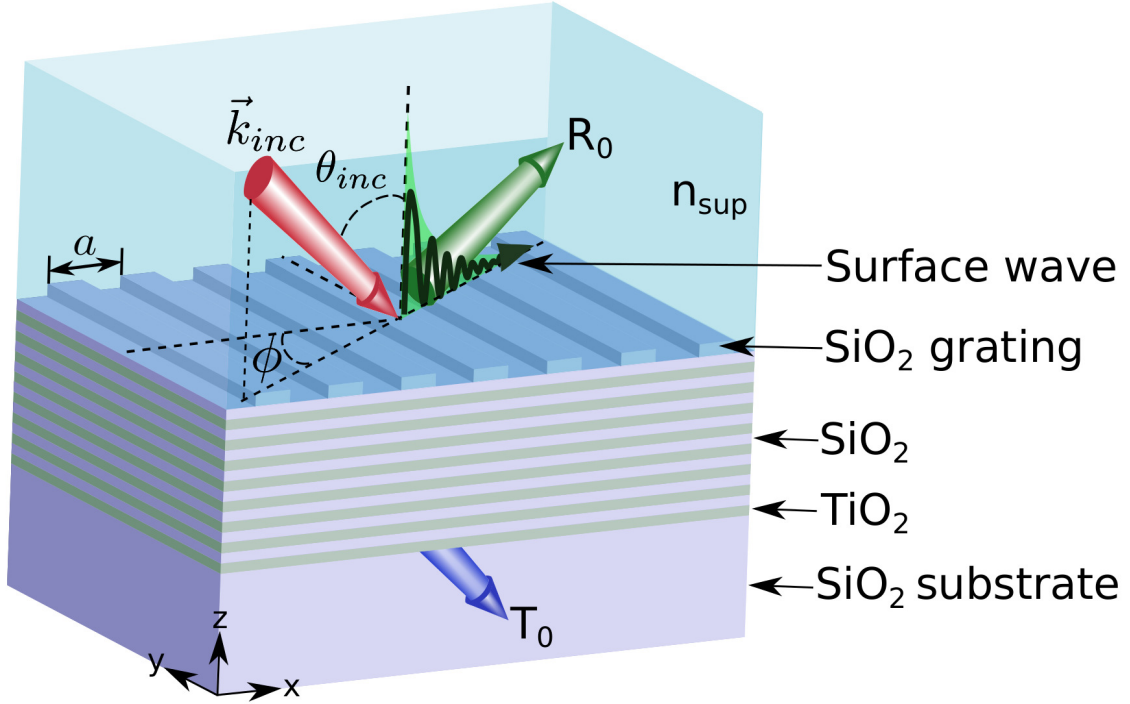


Figure 35: Schematic of a grating coupling technique to excite leaky Bloch surface waves on the surface of a dielectric multilayer.

$$k_{y,n} = k_{y,inc} - \frac{2\pi n}{\Lambda_y}, \quad n = -\infty, \dots, -2, -1, 0, 1, 2, \dots, \infty. \quad (267)$$

$k_{x,inc} = \frac{2\pi}{\lambda} n_{sup} \sin(\theta_{inc}) \cos(\phi)$ and $k_{y,inc} = \frac{2\pi}{\lambda} n_{sup} \sin(\theta_{inc}) \sin(\phi)$ are the x and y components of the \mathbf{k}_{inc} . $\Lambda_x = a$ is the grating period in the x direction. The structure considered in this paper does not have any periodicity in y direction. Thus Λ_y can be set to any value. For simplicity however, here we set $\Lambda_y = a$ as well. $\mathbf{S}_{m,n}(z)$ and $\mathbf{U}_{m,n}(z)$ in Eqn. (264) and (265) are the Fourier coefficients, which can be computed by solving Maxwell's equations in Fourier space. The method is described in detail in Chapter 2.2.

To verify the results obtained from the 3D SMRCWA method, we also do a 3D implementation of the structure in a commercial Finite Element Method software COMSOL Multiphysics. A detailed step-by-step tutorial on setting the model up in COMSOL Multi-

physics and reproducing the results of this paper is presented in Appendix A. The results from both the methods are in good agreement. Moreover, the dispersion curves and the mode profiles were verified using Meep (an open source FDTD software from MIT) as well.

6.3 Results and Discussions

The proposed method consists in taking advantage of the surface grating profile, as illustrated in Figure 35, to excite and then use BSW for biosensing via azimuthal interrogation. It is however, first crucial to realize BSW in a setting where $\phi = 0^0$. A cross-section of a one period structure for this purpose is shown in Figure 36(a). The surface grating serves as an input coupler that couples a plane wave (PW) mode into BSW mode. This BSW mode excitation is assisted by the constructive interference of PWs. At the correct incidence angle and groove spacing, a maximum coupling of the PWs to the BSW mode on the grating can be achieved, as summarized by Eqn. (268).

$$k_{BSW} = -k_0 n_{\text{sup}} \sin(\theta_{inc}) + 2\pi m/a, \quad (268)$$

where $k_0 = 2\pi/\lambda$ and k_{BSW} are the magnitudes of the free space wave vector and grating BSW wave vector respectively, n_{sup} is the refractive index of the superstrate, θ_{inc} is the incident angle, a is the grating period, and m is an integer [136].

To excite grating coupled BSW for a given incident wavelength, the grating period a is chosen such that there is at least one angle that satisfies Eqn. (268), which leads to $\lambda/a < k_{BSW}/k_0 + 1$ with the superstrate index taken as 1. In this paper, we choose $m = 1$ and $\theta_{inc} > 0$, such that $2\pi/a > k_{BSW}$. Given that $k_{BSW} > k_0$, we get $\lambda/a > k_{BSW}/k_0 > 1$. Therefore, the range of appropriate grating period can be summarized as $k_{BSW}/k_0 < \lambda/a < k_{BSW}/k_0 + 1$.

The surface mode band structures of BSW modes for the structure are shown in Figure 36(b). By terminating the surface layer with an additional thickness to act as a defect, we can create a platform for exciting BSWs, and etching a grating profile on top of it, we

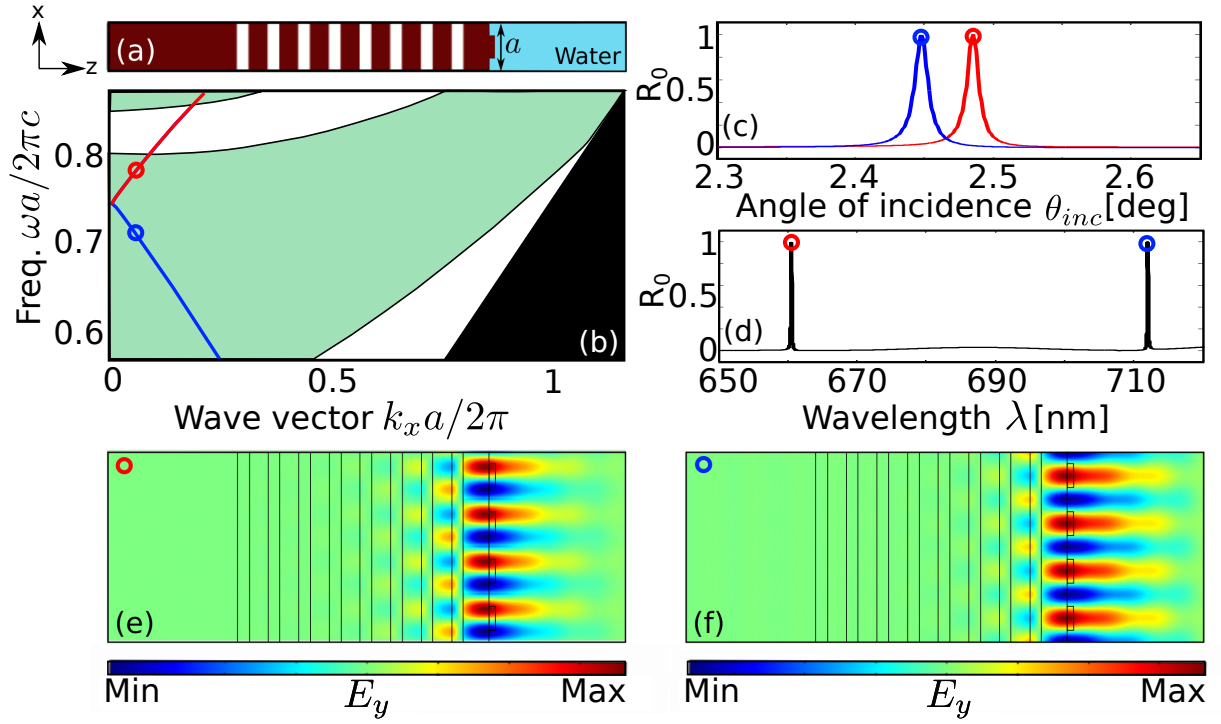


Figure 36: Leaky Bloch surface wave at $\phi = 0^\circ$. (a) TiO₂-SiO₂ multilayer with grating on the top layer. (b) Dispersion curves of the leaky BSWs supported by the structure. The green region is the radiative region (c)-(d) Reflectance of BSW as a function of incident angle and wavelength respectively. (e)-(f) Electric field profiles of BSW modes. The red and blue circles at the resonance peaks represent the reflectance at the corresponding circles in (b).

can mitigate the necessity of a prism to excite them. Periodicity on the surface plays an important role on these modes. The evanescent fields in the superstrate layer, in the presence of periodicity, can have wavevector k_x in the reciprocal lattice that are integer multiples of $2\pi/a$, resulting in BSW resonances. We observe two distinct BSW modes, highlighted in red and blue, in Figure 36(b). Reflectivity curves of these modes, as a function of angle of incidence and wavelength, are shown in Figure 36(c) and 36(d) respectively, where the colored tips correspond to their respective colored circle marks in Figure 36(b). As can be seen in these figures, these modes have sharp resonance features at their excitation both as

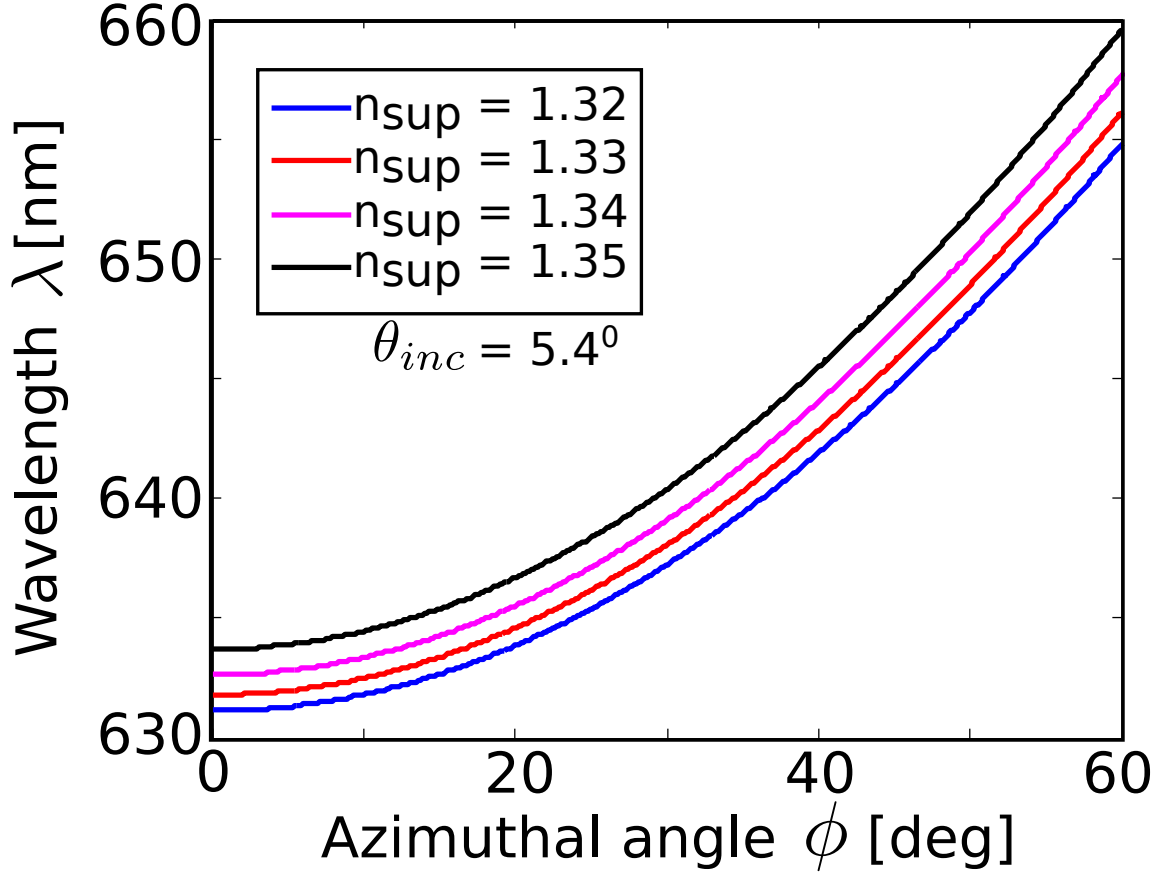


Figure 37: Azimuthal dispersion curves of BSWs for different values of superstrate refractive indices and $\theta_{inc} = 5.4^\circ$.

a function of angle and wavelength. Figure 36(e) and 36(f) show the field profile E_y of the BSW modes at the red ($\lambda = 660$ nm) and blue ($\lambda = 710$ nm) circles in Figure 36(b) at $\theta_{inc} \approx 2.5^\circ$. At these surface-parallel wavevectors near $k_{x,inc} \approx 0.04 \times 2\pi/a$, the E_y field is highly confined to the surface giving rise to the BSW modes. We can also see a slight leakage in the superstrate layer. The direction of propagation of these modes in Figure 36(d) and 36(e) are opposite however. This difference in the direction of propagation can be explained by the opposite slopes of the red and blue BSW modes in Figure 36(b). These modes are different than conventional BSW modes as they exist in the radiative region.

BSWs in general, only exist in the non-radiative region where they are perfectly bound to the surface. The BSW modes under consideration in this paper are not perfectly bound and are somewhat leaky. However, the quality factor ($Q = \omega\tau/2 = (1/Q_r) + (1/Q_{nr})$) of these modes are high enough ($Q \approx 6000$) that they can safely be used for practical applications in bio-sensing. The resonance lifetimes are extracted from the Fano features [109] by fitting the reflectivity of the grating coupled multilayer structure to be the thin-film reflectivity with the Fano features described by

$$f(\omega) = \frac{Q_r^{-1}}{2i(1 - \omega/\omega_0) + Q_r^{-1} + Q_{nr}^{-1}}(r_{slab} - t_{slab}), \quad (269)$$

where ω_0 is the resonance frequency, Q_r and Q_{nr} are the normalized radiative and non-radiative lifetimes due to leakage into the free space, r_{slab} and t_{slab} are the reflection and transmission coefficients of a homogeneous slab, respectively. We further confirmed the quality factors of these modes using finite-difference time-domain (FDTD) simulations with point sources on the surface to perform harmonic analysis to compute the lifetime τ and Q of these resonant modes.

With this understanding of BSWs for $\phi = 0^0$, we can now move to BSWs via azimuthal interrogation, i.e., $\phi \neq 0^0$. To explore this, we choose the operating wavelength of 632.8 nm and set $\theta_{inc} = 5.4^0$, which is slightly above the actual BSW excitation angle (θ_{BSW}) of 5.2^0 for $\phi = 0^0$. Setting the incident angle greater than the actual BSW excitation angle is important as indicated by $k_{x,inc} = \frac{2\pi}{\lambda} n_{sup} \sin(\theta_{inc}) \cos(\phi)$. With greater θ_{inc} , we can get $k_{x,inc} = k_{BSW}$ by changing ϕ , thus excite azimuthal BSW. Figure 37 shows the surface mode band structures of azimuthal BSW modes for different values of superstrate refractive indices. This figure indicates directly how the azimuthal angle sensing is achieved. For a fixed incident wavelength the azimuthal angle of coupling changes with superstrate refractive index. Similarly, at fixed azimuthal angle the coupling wavelength alters with superstrate index.

Sensitivity enhancement of biosensors is an active field of research. Both surface plasmon polaritons [133–135] and BSWs [14, 18, 22, 23] are widely used for the purpose of making

plasmonic biosensors. Prism coupling techniques – Kretschmann configuration and Otto configurations – are the two most widely used sensing techniques, with angular sensitivity in the range of 50-200 ⁰/RIU. In general the grating coupling technique, although having an advantage of not requiring a voluminous prism, has suffered with lower sensitivity compared to prism coupling techniques. However, all the studies on sensitivity analysis of grating coupling techniques have only utilized polar angle interrogation. Recently, Romanato et al. [120] studied sensitivity enhancement in grating coupled surface plasmon resonance by azimuthal control. The authors search for an optimal value of the azimuthal angle, set the value and sweep over the polar θ_{inc} angle. In this paper, we take an opposite approach. First the θ_{inc} angle is set to an angle greater than θ_{BSW} for $\phi = 0^0$, then the azimuthal angle is swept over to excite azimuthal BSW at appropriate ϕ .

Figure 38(a) shows BSW modes supported by the structure as a function of superstrate refractive indices and azimuthal angle for different values of polar incident angles at the wavelength of 632.8 nm. We observe that for high values of θ_{inc} , the azimuthal angular range for BSWs get wider. More importantly, at smaller azimuthal angles, the dispersion curves tend to flatten, i.e., for a small change in the superstrate refractive index, the change in the azimuthal angle is significantly larger. This has a crucial impact in increasing the azimuthal sensitivity of BSWs. The azimuthal sensitivity ($S_{n_{sup},\phi}$) is defined as

$$S_{n_{sup},\phi} = \frac{\Delta\phi}{\Delta n_{sup}}, \quad (270)$$

where, $\Delta\phi$ is the change in the azimuthal angle and Δn_{sup} is the change in the superstrate refractive index. The results for the azimuthal sensitivity given by Eqn. (270) is shown in Figure 38(b). The sensitivity curves are computed from their respective colored BSW modes in Figure 38(a). The improvement in the sensitivity can be clearly seen from the figure, with the azimuthal sensitivity as high as ~ 2500 ⁰/RIU. Higher sensitivity is especially useful for detecting tiny variations in the refractive index, as well as in detecting antibody-protein binding for disease detection. The sensitivity enhancement reported here is an order of magnitude higher compared to the previously reported grating coupled surface plasmon/BSW

sensitivities [25, 137–140], which typically is in the range of 50-200 $^{\circ}$ /RIU.

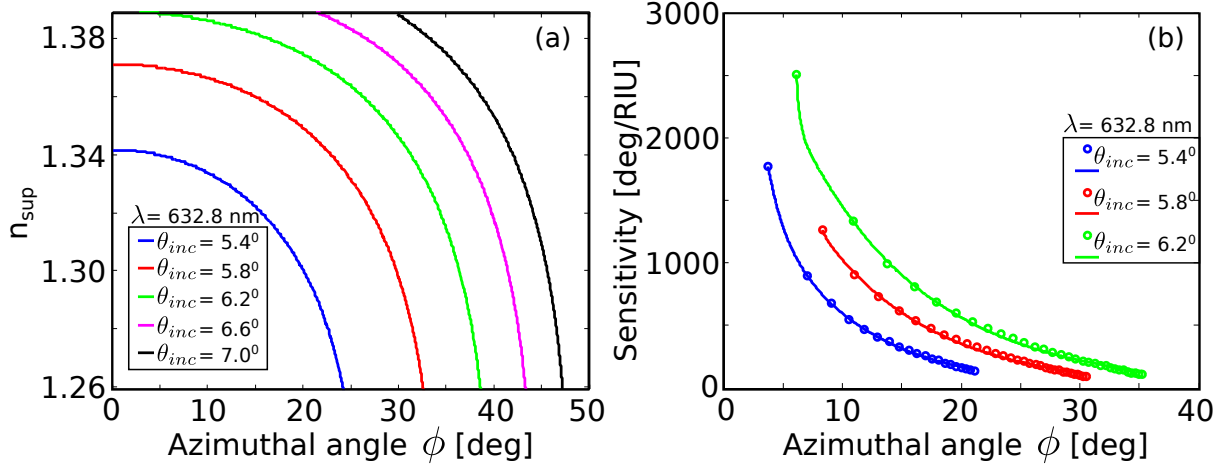


Figure 38: (a) BSW modes as a function of superstrate refractive index and azimuthal angle for different values of θ_{inc} and $\lambda = 632.8$ nm. (b) Azimuthal sensitivity of BSWs.

Figure 39(a) shows the reflectivity curves of the azimuthal BSWs for different values of the superstrate refractive indices. The solid curves are obtained using the 3D SMRCWA method, whereas the open circle curves are computed from COMSOL multiphysics. The results from both the numerical techniques are in excellent agreement with each other. We can observe from the figure that for a small change in the refractive index value ($\Delta n_{sup} = 0.005$), the azimuthal angular shift between the resonance peaks gets larger at small azimuthal angles. Finally, the field profile of azimuthal BSW for the superstrate refractive index of 1.33 (water) is shown in Figure 39(b)-39(d). The corresponding resonance peak is indicated in Fig 5(a) by the arrows. As in the case of conventional BSW ($\phi = 0^{\circ}$), the surface field intensity is highly amplified, and the mode is slightly leaky as well.

6.4 Summary

We have studied a new way of exciting Bloch surface waves in dielectric multilayer structures with grating profile on the top-most layer via azimuthal interrogation. Fixing the polar

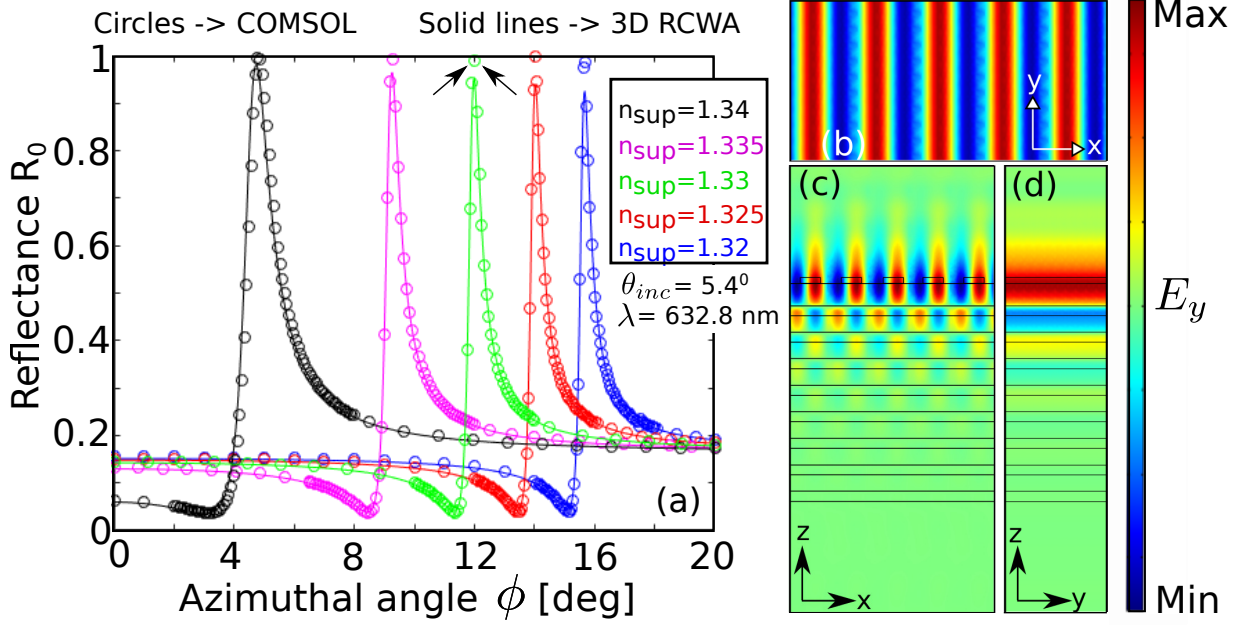


Figure 39: (a) Reflectivity curves as a function of Azimuthal angle for different values of n_{sup} . The wavelength (λ) and incident angle (θ) are fixed at 632.8 nm and 5.4° respectively. The results obtained using COMSOL (circles) and an in-house 3D RCWA code (solid lines) show good agreement. (b) x-y (c) x-z (d) y-z plane views of azimuthal BSW at the resonance peak indicated by the arrows in (a).

incident angle to a value slightly higher than the BSW angle (for $\phi = 0^\circ$ configuration), azimuthal BSWs can be excited by sweeping over the azimuthal angle. We show that as the refractive index of the superstrate layer increases, the azimuthal angular displacement between the BSW resonances increases as well. This significantly increases the sensitivity of azimuthal BSWs. We report an order of magnitude higher sensitivity compared to the sensitivity of conventional BSWs.

CHAPTER 7

CONCLUSION AND FUTURE WORK

In conclusion, BSWs are surface bound electromagnetic waves that have applications in various fields, such as label-free bio-sensing, fluorescence detection, optical data storage buffers using slow light, slow-light enhanced non-linear optical effects, and surface-enhanced Raman spectroscopy. In this dissertation, I have described a BSW-mediated configuration for slow light generation and explored BSW assisted bio-sensing specifically new avenues to improve the sensitivity of BSW based bio-sensors using different variations of 1D photonic crystals.

I demonstrated that BSWs in simple one-dimensional periodic multilayer structures can be used to reduce the group velocity of light. The reduction in the speed of light is attributed to the surface bound and non-radiative nature of BSWs that temporarily traps and stores light on the surface of such materials. The technique is relatively simple compared to other techniques described previously in the literature [53, 54].

I also numerically showed, for the first time, that BSWs/BLSWs can be excited in non-periodic multilayer structures. All previous work in BSWs was based on periodic multilayers with some sort of defect surface layer. Using non-periodic multilayer structures such as Fibonacci quasi-crystals, Thue-Morse aperiodic multilayers, and pseudo-random Maximum-length sequence multilayers, we demonstrated that the desirable properties of BSWs can be improved compared to the properties of BSWs in their periodic counterparts. Specifically, the sensitivity of BSW-based bio-sensors can be enhanced using such non-periodic multilayer structures. In addition the electromagnetic field amplification and penetration depth in prism-coupled configurations (Kretschmann or Otto geometries) can be engineered. The ability to tailor these qualities are of significant importance both in sensing and in enhancing non-linear optical phenomena.

Prism-coupling techniques are currently the dominant method used to excite BSWs;

however, the bulkiness of prisms limits the application of BSWs in nano-scaled sensors. To mitigate this problem, I investigated the grating-coupling technique that does not require a prism to generate BSWs with incident light. I presented a novel way of enhancing the sensitivity of one-dimensional photonic crystals through the use of azimuthal angle generation of BSWs. The maximum sensitivity achieved using azimuthal BSWs is more than 10-fold better as compared to the previously reported sensitivities in the literature using conventional polar angle coupling [25, 137–140].

The work in this dissertation can be envisaged as a road-map to explore new applications of BSWs in photonics. For example, the work on BSWs in 1D non-periodic multilayer structures can be extended into 2D non-periodic photonic crystals. Such systems can be created using either dielectric rods or etched holes in various patterns such as Fibonacci, Thue-Morse, or Maximum-length sequences. It is envisioned that such 2D non-periodic structures that support BSWs can be used for various optical devices such as beam splitters, waveguides, optical buffers, and slow light devices. The extension to two dimensions provides a larger parameter space with which to engineer desirable properties.

BSWs can be used in harvesting energy from light. A key drawback is that, because the phase matching restriction requires the use of either prism or periodic grating structure, it is only possible to couple a narrow wavelength and/or angular range into BSWs. To overcome this limitation, it is plausible to explore novel aperiodic surface structures that possess a range of grating wave vectors permitting coupling of a broad optical wavelength range (or a broad angular range of monochromatic radiation). One strategy to realize this objective is to employ gratings based on Maximal-length sequence patterns which mathematically possess all grating periodicities equally.

Another avenue of taking this work forward is through the design of BSW-based lasers. The strong confinement of BSWs to the material surface leads to high electromagnetic fields. By further confining the propagating modes in the plane of the surface, through the use of grating structures, it is possible to construct surface standing wave cavities. Laser radiation

could either be coupled out of the cavity using prism coupling or through first-order diffraction from the end gratings that define the cavity. Placing a gain medium on the surface or embedded in the termination layer of the multilayer, enables the creation of a new class of BSW laser. The BSW resonance is approximately 100 times narrower with concomitantly higher field intensities resulting in lasers with much lower threshold. In addition the possibility of making the termination layer, where the BSW field intensity is greatest, the gain medium makes this configuration an ideal candidate for developing a new compact laser source.

Another fruitful research avenue to extend this research is through the design of functional BSW materials that can serve as a platform for a new class of photonic circuits. Many authors have suggested and even done rudimentary experiments using surface plasmons on metal films as a venue for compact photonic circuits. However, the large dielectric loss of metals results in very short propagation distances for surface plasmons which means these schemes are unlikely to succeed in practical applications. In contrast, the BSW can propagate two orders of magnitude further because the dielectric multilayer materials have extremely low loss. Long propagation distance and the ability to create integrated laser sources make this functional material system a little studied, but highly promising, avenue for optical processing and interconnects.

Thus, this work is a starting point for a rich variety of scientific applications that can benefit human lives. I have listed some ideas that can be explored based on my work here. The hope is to inspire the reader to take these ideas forward and advance them with even newer concepts and applications.

BIBLIOGRAPHY

- [1] J. D. Joannopoulos, S. G. Johnson, J. N. Winn, and R. D. Meade, “Photonic crystals: Molding the flow of light, 2nd Edition,” *Princeton University Press*, (2008).
- [2] E. Yablonovitch, “Inhibited spontaneous emission in solid-state physics and electronics,” *Phys. Rev. Lett.*, **58**, 2059 (1987).
- [3] S. John, “Strong localization of photons in certain disordered dielectric superlattices,” *Phys. Rev. Lett.*, **58**, 2468 (1987).
- [4] W. M. Robertson, G. Arjavalingam, R. D. Meade, K. D. Brommer, A. M. Rappe, and J. D. Joannopoulos, “Measurement of photonic band structure in a two-dimensional periodic dielectric array,” *Phys. Rev. Lett.*, **68**, 2023 – 2026 (1992).
- [5] W. M. Robertson, G. Arjavalingam, R. D. Meade, K. D. Brommer, A. M. Rappe, and J. D. Joannopoulos, “Measurement of the photon dispersion relation in two-dimensional ordered dielectric arrays,” *J. Opt. Soc. Am. B*, **10**, 322 – 327 (1993).
- [6] P. Yeh, A. Yariv, and C. S. Hong, “Electromagnetic propagation in periodic stratified media-I: General theory,” *J. Opt. Soc. Am.*, **67** (4), 423 – 438 (1977).
- [7] R. D. Meade, K. D. Brommer, A. M. Rappe, and J. D. Joannopoulos, “Electromagnetic Bloch waves at the surface of a photonic crystal,” *Phys. Rev. B*, **44**, 10961 – 10964 (1991).
- [8] W. M. Robertson, G. Arjavalingam, R. D. Meade, K. D. Brommer, A. M. Rappe, and J. D. Joannopoulos, “Observation of surface photons on periodic dielectric arrays,” *Opt. Lett.*, **18**, 528 – 530 (1993).
- [9] W. M. Robertson, “Experimental measurement of the effect of termination on surface electromagnetic waves in one-dimensional photonic bandgap arrays,” *J. Lightwave Tech.*, **17**, 2013 – 2017 (1999).

- [10] W. M. Robertson, and M. S. May, “Surface electromagnetic wave excitation on one-dimensional photonic band-gap arrays,” *Appl. Phys. Lett.*, **74**, 1800 – 1803 (1999).
- [11] A. Otto, “Excitation of nonradiative surface plasma waves in silver by the method of frustrated total reflection,” *Z. Phys.*, **216** (4), 398 – 410 (1968).
- [12] E. Kretschmann, and H. Raether, “Radiative decay of non radiative plasmons excited by light,” *Z. Naturforsch. A*, **23**, 2135 – 2136 (1968).
- [13] U. Fano, “The theory of anomalous diffraction gratings and of quasi-stationary waves on metallic surfaces (Sommerfelds Waves),” *J. Opt. Soc. Amer.*, **31**, 213 – 222 (1941).
- [14] K. Toma, E. Descrovi, M. Toma, M. Ballarini, P. Mandracci, F. Giorgis, A. Mateescu, U. Jonas, W. Knoll, and J. Dostalek, “Bloch surface wave-enhanced fluorescence biosensor,” *Biosen. & Bioelec.*, **43**, 108 – 114 (2013).
- [15] A. Angelini, E. Enrico, N. D. Leo, P. Munzert, L. Boarino, F. Michelotti, F. Giorgis, and E. Descrovi, “Fluorescence diffraction assisted by Bloch surface waves on a one-dimensional photonic crystal,” *New Jour. of Phys.*, **15**, 073002 (2013).
- [16] K. Matsubara, S. Kawata, and S. Minami, “Multilayer system for a high-precision surface plasmon resonance sensor,” *Opt. Lett.*, **15**, 75 – 77 (1990).
- [17] C. Jamois, C. Li, R. Orobtcouk, and T. Benyattou, “Slow Bloch surface wave devices on porous silicon for sensing applications,” *Phot. and Nano. - Fund. and Appli. B*, **8**, 72 – 77 (2010).
- [18] A. Farmer, A. C. Friedli, S. M. Wright, and W. M. Robertson, “Biosensing using surface electromagnetic waves in photonic band gap multilayers,” *Sensors and Actuators B*, **173**, 79 – 84 (2012).
- [19] A. Sinibaldi, N. Danz, E. Descrovi, P. Munzert, U. Schulz, F. Sonntag, L. Dominici,

- and F. Michelotti, “Direct comparison of the performance of Bloch surface wave and surface plasmon polariton sensors,” *Sensors and Actuators B*, **174**, 292 – 298 (2012).
- [20] F. Frascella, S. Ricciardi, P. Rivolo, V. Moi, F. Giorgis, E. Descrovi, F. Michelotti, P. Munzert, N. Danz, L. Napione, M. Alvaro, and F. Bussolino, “A fluorescent one-dimensional photonic crystal for label-free biosensing based on Bloch surface waves,” *Sensors*, **13**, 2011 – 2022 (2013).
- [21] R. Rizzo, N. Danz, F. Michelotti, E. Maillart, A. Anopchenko, and C. Wächter, “Optimization of angularly resolved Bloch surface wave bio-sensors,” *Opt. Exp.*, **22**, 2566 – 2578 (2013).
- [22] F. Giorgis, E. Descrovi, C. Summonte, L. Dominici, and F. Michelotti, “Experimental determination of the sensitivity of Bloch surface waves based sensors,” *Opt. Exp.*, **18**, 8087 – 8083 (2010).
- [23] M. Shinn, and W. M. Robertson, “Surface plasmon-like sensor based on surface electromagnetic waves in a photonic band-gap material,” *Sensors and Actuators B*, **105**, 360 – 364 (2005).
- [24] M. Liscidini, and J. E. Sipe, “Enhancement of diffraction for biosensing applications via Bloch surface waves,” *Appl. Phys. Lett.*, **91**, 253125 (2007).
- [25] G. A. Rodriguez, J. D. Ryckman, Y. Jiao, and S. M. Weiss, “A size selective porous silicon grating-coupled Bloch surface and sub-surface wave biosensor,” *Bio-sensors and Bioelectronics*, **54**, 486 – 493 (2014).
- [26] V. Koju, and W. M. Robertson, “Slow light by Bloch surface wave tunneling,” *Opt. Exp.*, **22**, 15679 – 15685 (2014).
- [27] A. Angelini, E. Barakat, P. Munzert, L. Boarino, N. D. Leo, E. Enrico, F. Giorgis, H.

- P. Herzig, C. F. Pirri, and E. Descrovi, “Focusing and extraction of light mediated by Bloch surface waves,” *Sci. Reports*, **4**, 5428 (2014).
- [28] L. Yu, E. Barakat, T. Sfez, L. Hvozدارa, J. D. Francesco, and H. P. Herzig, “Manipulating Bloch surface waves in 2D: a platform concept-based flat lens,” *Light: Science & Applications*, **3**, e124 (2013).
- [29] A. Delfan, M. Liscidini, and J. E. Sipe, “Surface enhanced Raman scattering in the presence of multilayer dielectric structures,” *J. Opt. Soc. Am. B*, **29**, 1863 – 1874 (2012).
- [30] S. Pirotta, X. G. Xu, A. Delfan, S. Mysore, S. Maiti, G. Dacarro, M. Patrini, M. Galli, G. Guizzetti, D. Bajoni, J. E. Sipe, G. C. Walker, and M. Liscidini, “Surface-enhanced Raman scattering in purely dielectric structures via Bloch surface waves,” *J. Phys. Chem. C*, **117**, 6821 – 6825 (2013).
- [31] P. Yeh, “Optical waves in layered media,” *John Wiley & Sons, Inc*, (1988).
- [32] R. C. Rumpf, “Improved formulation of scattering matrices for semi-analytical methods that is consistent with convention,” *PIER B*, **35**, 241 – 261 (2011).
- [33] Z. Y. Li, and L. L. Lin, “Photonic band structures solved by a plane-wave-based transfer-matrix method,” *Phys. Rev. E*, **67**, 046607 (2003).
- [34] D. Y. K. Ko, and J. R. Sambles, “Scattering matrix method for propagation of radiation in stratified media: Attenuated total reflection studies of liquid crystal,” *J. Opt. Soc. Am. A*, **5**, 1863 – 1866 (1988).
- [35] R. Redheffer, “Difference equations and functional equations in transmission-line theory,” *Modern Mathematics for the Engineer*, **12**, 282 – 337 (1961).
- [36] M. G. Moharam, E. B. Grann, and D. A. Pommet, “Formulation for stable and efficient implementation of the rigorous coupled-wave analysis of binary gratings,” *J. Opt. Soc. Am. A*, **12**, 1068 – 1076 (1995).

- [37] M. G. Moharam, E. B. Grann, D. A. Pommet, and T. K. Gaylord, “Stable implementation of the rigorous coupled-wave analysis for surface-relief gratings: enhanced transmittance matrix approach,” *J. Opt. Soc. Am. A*, **12**, 1068 – 1076 (1995).
- [38] L. Li, “New formulation of the Fourier modal method for cross surface-relief gratings,” *J. Opt. Soc. Am. A*, **14**, 2758 – 2767 (1997).
- [39] T. K. Gaylord, and M. G. Moharam, “Analysis and applications of optical diffraction by gratings,” *Proc. IEEE*, **73**, 894 – 937 (1985).
- [40] M. G. Moharam, and T. K. Gaylord, “Rigorous coupled-wave analysis of planar-grating diffraction,” *J. Opt. Soc. Am.*, **71**, 811 – 818 (1981).
- [41] M. G. Moharam, and T. K. Gaylord, “Diffraction analysis of dielectric surface-relief gratings,” *J. Opt. Soc. Am. A*, **72**, 1385 – 1392 (1982).
- [42] M. G. Moharam, and T. K. Gaylord, “Rigorous coupled-wave analysis of metallic surface-relief gratings,” *J. Opt. Soc. Am. A*, **3**, 1780 – 1787 (1986).
- [43] D. M. Sullivan, “Electromagnetic simulation using the FDTD method,” *Piscataway, NJ: IEEE Press*, (2000).
- [44] A. Taflove, and S. C. Hagness, “Computational Electrodynamics: the Finite-Difference Time-Domain Method, 2nd Edition,” *Norwood, MA: Artech House, Inc.*, (2000).
- [45] K. S. Yee, “Numerical solution of the initial boundary value problems involving Maxwell’s equations in isotropic media,” *IEEE Trans. Antennas and Propagation*, **14**, 302 – 307 (1996).
- [46] S. D. Gedney, “Introduction to the Finite-Difference Time-Domain (FDTD) Methods for Electromagnetics,” *Morgan & Claypool publishers*, (2011).

- [47] A. F. Oskooi, D. Roundy, M. Ibanescu, P. Bermel, J. D. Joannopoulos, and S. G. Johnson, “MEEP: A flexible free-software package for electromagnetic simulations by the FDTD method,” *Computer Physics Communications*, **181**, 687 – 702 (2010).
- [48] J. L. Volakis, A. Chatterjee, and L. C. Kempel, “Finite Element Methods for Electromagnetics: With Applications to Antennas, Microwave Circuits, and Scattering,” *IEEE Press, New York*, (1998).
- [49] F. A. Fernandez, and Y. Lu, “Microwave and Optical Waveguide Analysis by the Finite Element Method,” *John Wiley, Chichester, New York*, (1996).
- [50] P. P. Silvester, and R. L. Ferrari, “Finite Elements for Electrical Engineers, 3rd edition,” *Cambridge University Press, Cambridge*, (1990).
- [51] L. Y. Tio, A. A. P. Gibson, B. Dillon, and L. E. Davis, “Weak form finite element formulation for the Helmholtz equation,” *Int. Journal of Elec. Eng. Edu.*, **41**, 1 (2004).
- [52] Internet, “www.comsol.com,” *COMSOL Inc.*
- [53] L. V. Hau, S. E. Harris, Z. Dutton, and C. H. Behroozi, “Light speed reduced to 17 metres per second in an ultracold atomic gas,” *Nature*, **397**, 594 – 598 (1999).
- [54] G. Heinze, C. Hubrich, and T. Halfmann, “Stopped light and image storage by electromagnetically induced transparency up to the regime of one minute,” *Phys. Rev. Lett.*, **111**, 033601 (2013).
- [55] S. Wang, H. Erlig, H. R. Fetterman, E. Yablonovitch, V. Grubsky, D. S. Starodubov, and J. Feinberg, “Measurement of the temporal delay of a light pulse through a one-dimensional photonic crystal,” *Micro. Opt. Tech. Lett.*, **20**, 17 – 21 (1999).
- [56] T. Asano, K. Kiyota, D. Kumamoto, B. S. Song, and S. Noda, “Time-domain measurements of picosecond light-pulse propagation in a two-dimensional photonic crystal-slab waveguide,” *Appl. Phys. Lett.*, **84**, 4690 – 4692 (2002).

- [57] T. Baba, D. Mori, K. Inoshita, and Y. Kuroki, “Light localization in line defect photonic crystal waveguides,” *IEEE J. Select. Topics Quant. Electron.*, **10**, 484 – 491 (2004).
- [58] C. E. Finlayson, F. Cattaneo, N. M. B. Perney, J. J. Baumberg, M. C. Netti, M. E. Zoorob, M. D. B. Charlton, and G. J. Parker, “Slow light and chromatic temporal dispersion in photonic crystal waveguides using femtosecond time of flight,” *Phys. Rev. Lett.*, **73**, 016619 (2006).
- [59] T. Baba, and D. Mori, “Slowlight engineering in photonic crystals,” *J. Phys. D*, **40**, 2659 – 2665 (2007).
- [60] T. Krauss, “Slow light in photonic crystal waveguides,” *J. Phys. D*, **40**, 2666 – 2670 (2007).
- [61] G. Grgić, J. G. Pedersen, S. Xiao, and N. A. Mortensen, “Group index limitations in slow-light photonic crystals,” *Photon. Nanost. – Fund. and App.*, **8**, 56 – 61 (2010).
- [62] M. E. Yanik, and S. Fan, “Stopping light all optically,” *Phys. Rev. Lett.*, **92**, 083901 (2004).
- [63] M. E. Yanik, W. Suh, Z. Wang, and S. Fan, “Stopping light in a waveguide with an all-optical analog of electromagnetically induced transparency,” *Phys. Rev. Lett.*, **93**, 233903 (2004).
- [64] K. Üstün, and H. Kurt, “Ultra slow light achievement in photonic crystals by merging coupled cavities with waveguides,” *Opt. Exp.*, **18**, 21155-21161 (2010).
- [65] T. F. Krauss, “Why do we need slow light?,” *Nat. Phot.*, **2**, 448 – 450 (2008).
- [66] T. Baba, “Slow light in photonic crystals,” *Nat. Phot.*, **2**, 465 – 573 (2008).
- [67] H. Gersen, T. J. Karle, R. J. P. Engelen, W. Gogaerts, J. P. Korterik, N. F. van Hulst, T. F. Krauss, and L. Kuipers, “Real-spaced observation of ultraslow light in photonic crystal waveguides,” *Phys. Rev. Lett.*, **94**, 073903 (2005).

- [68] Y. A. Vlasov, M. O'Boyle, H. F. Hamann, and S. J. McNab, "Active control of slow light on a chip with photonic crystal waveguides," *Nature*, **438**, 65 – 69 (2005).
- [69] V. Govindan, and S. Blair, "Nonlinear pulse interaction in microresonator slow-light waveguides," *J. Opt. Soc. Am. B*, **25**, C23 – C30 (2008).
- [70] M. Soljačić, S. Johnson, S. Fan, M. Ibanescu, E. Ippen, and J. Joannopoulos, "Photonic-crystal slow-light enhancement of nonlinear phase sensitivity," *J. Opt. Soc. Am. B*, **19**, 2052 – 2059 (2002).
- [71] M. Soljačić, and J. D. Joannopoulos, "Enhancement of nonlinear effects using photonic crystals," *Nat. Mater.*, **3**, 211 – 219 (2004).
- [72] K. Inoue, H. Oda, N. Ikeda, and K. Asakawa, "Enhanced third-order nonlinear effects in slow light photonic-crystal slab waveguides of line defect," *Opt. Exp.*, **17**, 7206 (2009).
- [73] J. McMillan, X. Yang, N. Panoiu, R. Osgood, and C. Wong, "Enhanced stimulated Raman scattering in slow-light photonic crystal waveguides," *Opt. Lett.*, **31**, 1235 – 1237 (2006).
- [74] N. A. Mortensen, and S. S. Xiao, "Slow-light enhancement of Beer-Lambert-Bouguer absorption," *Appl. Phys. Lett.*, **90**, 141108 (2007).
- [75] Y. Zhao, Y. Zhang, and Q. Wang, "High sensitivity gas sensing method based on slow light in photonic crystal waveguide," *Sensors and Actuators B*, **173**, 28 – 31 (2012).
- [76] G. M. Gehring, A. C. Liapis, S. G. Lukishova, and R. W. Boyd, "Time-domain measurements of reflection delay in frustrated total internal reflection," *Phys. Rev. Lett.*, **111**, 030404 (2013).
- [77] T. Hattori, N. Tsurumachi, S. Kawato, and H. Nakatsuka, "Photonic dispersion relation in a one-dimensional quasicrystal," *Phys. Rev. B*, **50**, 4220 – 4223 (1994).

- [78] M. A. Kaliteevski, V. V. Nikolaev, R. A. Abram, and S. Brand, “Bandgap structure of optical Fibonacci lattices after light diffraction,” *Opt. Spectrosc.*, **91**, 109–118 (2001).
- [79] X. Q. Hauang, S. S. Jiang, R. W. Peng, and A. Hu, “Perfect transmission and self similar optical transmission spectra in symmetric Fibonacci-class multilayers,” *Phys. Rev. B*, **63**, 245104 (2001).
- [80] R. W. Peng, X. Q. Huang, F. Qiu, M. Wang, A. Hu, S. S. Jiang, and M. Mazzer, “Symmetry-induced perfect transmission of light waves in quasiperiodic dielectric multilayers,” *Appl. Phys. Lett.*, **80**, 3063–3065 (2002).
- [81] R. Nava, J. Taguena-Martinez, J. A. del Rio, and G. G. Naumis, “Perfect light transmission in Fibonacci arrays of dielectric multilayers,” *J. Phys. Condens. Matter*, **21**, 155901 (2009).
- [82] N. Liu, “Propagation of light waves in Thue-Morse dielectric multilayers,” *Phys. Rev. B*, **55**, 3543–3547 (1997).
- [83] L. Dal Negro, C. J. Oton, Z. Gaburro, L. Pavesi, P. Johnson, A. Lagendijk, R. Righini, M. Colocci, and D. S. Wiersma, “Light transport through the band-edge states of Fibonacci quasicrystals,” *Phys. Rev. Lett.*, **90**, 055501 (2003).
- [84] M. Ghulinyan, C. J. Oton, L. D. Negro, and L. Pavesi, R. Sapienza, M. Colocci, and D. S. Wiersma, “Light-pulse propagation in Fibonacci quasicrystals,” *Phys. Rev. B*, **71**, 094204 (2005).
- [85] W. Gellermann, M. Kohmoto, B. Sutherland, and P. C. Taylor, “Localization of light waves in Fibonacci dielectric multilayers,” *Phys. Rev. Lett.*, **72**, 633–636 (1994).
- [86] M. Dulea, M. Johnsson, and R. Riklund, “Localization of electrons and electromagnetic waves in a deterministic aperiodic system,” *Phys. Rev. B*, **45**, 105–114 (1992).

- [87] Z. V. Vardeny, A. Nahata, and A. Agrawal, “Optics of photonic quasicrystals,” *Nature Photonics*, **7**, 177 – 187 (2013).
- [88] V. Koju, and W. M. Robertson, “Excitation of Bloch-like surface waves in quasi-crystals and aperiodic dielectric multilayers,” *Opt. Lett.*, **41**, 2915 – 2918 (2016).
- [89] V. Koju, and W. M. Robertson, “Bloch-like surface waves in Fibonacci quasi-crystals and Thue-Morse aperiodic dielectric multilayers,” *Proc. of SPIE, 9929, Nanostructured Thin Films IX*, 99290O (2016).
- [90] M. Kohmoto, L. P. Kadanoff, and C. Tang, “Localization problem in one dimension: Mapping and Escape,” *Phys. Rev. Lett.*, **50**, 1870 (1983).
- [91] R. Riklund, and M. Severin, “Optical properties of perfect and non-perfect quasi-periodic multilayers: a comparison with periodic and disordered multilayers,” *J. Phys. C.*, **21**, 3217 (1988).
- [92] D. Dulea, M. Severin, and R. Riklund, “Transmission of light through deterministic aperiodic non-Fibonacci multilayers,” *Phys. Rev. B*, **42**, 14396 – 14403 (1990).
- [93] G. P. Bryan-Brown, J. R. Sambles, and M. C. Hutley, “Polarization conversion through the excitation of surface plasmons on a metallic grating,” *J. Mod. Opt.*, **37**, 1227 (1990).
- [94] S. J. Elston, G. P. Bryan-Brown, and J. R. Sambles, “Polarization conversion from diffraction gratings,” *Phys. Rev. B*, **44**, 6393 – 6400 (1991).
- [95] F. V. Laere, G. Roelkens, M. Ayre, J. Schrauwen, D. Taillaert, D. V. Thourhout, T. F. Krauss, and R. Baets, “Compact and highly efficient grating couplers between optical fiber and nanophotonic waveguides,” *J. Lightwave Tech.*, **25**, 151 – 156 (2007).
- [96] J. Lu, C. Petre, E. Yablonovitch, and J. Conway, “Numerical optimization of a grating coupler for the efficient excitation of surface plasmons at an Ag-SiO₂ interface,” *J. Opt. Soc. Am. B*, **24**, 2268 – 2272 (2007).

- [97] Y. Tang, and D. Dai, "Proposal for a grating waveguide serving as both a polarization splitter and an efficient coupler for silicon-on-insulator nanophotonic circuits," *IEEE Photonics Tech. Lett.*, **21**, 242 – 244 (2009).
- [98] A. Y. Piggott, J. Lu, T. M. Babinec, K. G. Lagoudakis, J. Petykiewicz, and J. Vockovic, "Inverse design and implementation of a wavelength demultiplexing grating coupler," *Sci. Reports*, **4**, 7210 (2014).
- [99] M. Liscidini, and J. E. Sipe, "Analysis of Bloch-surface-wave assisted diffraction-based bio-sensors," *J. Opt. Soc. Amer.*, **26**, 279 – 289 (2009).
- [100] M. Liscidini, M. Galli, M. Patrini, R. W. Loo, M. C. Goh, C. Ricciardi, F. Giorgis, and J. E. Sipe, "Demonstration of diffraction enhancement via Bloch surface waves in a-SiN:H multilayers," *Appl. Phys. Lett.*, **94**, 043117 (2009).
- [101] J. R. Devore, "Refractive indices of Rutile and Sphalerite," *J. Opt. Soc. Am.*, **41**, 416 (1951).
- [102] I. H. Malitson, "Interspecimen comparison of the refractive index of Fused Silica," *J. Opt. Soc. Am.*, **55**, 1205 (1965).
- [103] C. C. Ting, S. Y. Chen, and D. M. Liu, "Structural evolution and optical properties of TiO₂ thin films prepared by thermal oxidation of sputtered Ti films," *J. Appl. Phys.*, **88**, 4628 (2000).
- [104] S. Chao, W. H. Wang, and C. C. Lee, "Low-loss dielectric mirror with ion-beam-sputtered TiO₂-SiO₂ mixed films," *Appl. Opt.*, **40**, 2177 (2001).
- [105] M. Born, and E. Wolf, "Principles of Optics, Electromagnetic Theory of propagation, Interface and Diffraction of Light," *Pergamon Press Inc., New York*, (1980).
- [106] A. Shalabney, and I. Abdulhalim, "Electromagnetic fields distribution in multilayer

- thin film structures and the origin of sensitivity enhancement in surface plasmon resonance sensors,” *Sensors and Actuators A*, **159**, 24 – 32 (2010).
- [107] A. A. Maradudin, I. Simonsen, and W. Zierau, “Leaky surface electromagnetic waves on a high-index dielectric grating,” *Opt. Lett.*, **41** (10), 2229 – 2232 (2016).
- [108] C. W. Hsu, B. Zhen, S. L. Chua, S. G. Johnson, J. D. Joannopoulos, and M. Soljačić, “Bloch surface eigenstates within the radiation continuum,” *Light: Science & Applications*, **2**, e84 (2013).
- [109] C. W. Hsu, B. Zhen, J. Lee, S. L. Chua, S. G. Johnson, J. D. Joannopoulos, and M. Soljačić, “Observation of trapped light within the radiation continuum,” *Nature*, **499**, 188 – 191 (2013).
- [110] J. W. Yoon, H. S. Song, and R. Magnusson, “Critical field enhancement of asymptotic optical bound states in the continuum,” *Sci. Reports*, **5**, 18301 (2015).
- [111] Y. Ding, and R. Magnusson, “Resonant leaky-mode spectral-band engineering,” *Opt. Exp.*, **12**, 5661 – 5674 (2004).
- [112] S. S. Wang, and R. Magnusson, “Theory and applications of guided-mode resonance filters,” *Appl. Opt.*, **32** (14), 2602 – 2613 (1993).
- [113] R. Magnusson, J. Yoon, and D. Wawro, “Properties of resonant modal-plasmonic multiparametric biosensors,” *Proc. SPIE 8570, Frontiers in Biological Detection: From Nonosensors to Systems V*, 85700K (2013).
- [114] D. Fattal, J. Li, Z. Peng, M. Fiorentino, and R. G. Beausoleil, “Flat dielectric grating reflectors with focusing abilities,” *Nat. Photon.*, **4**, 466 – 470 (2010).
- [115] J. H. Lee, J. W. Yoon, M. J. Jung, J. K. Hong, S. H. Song, and R. Magnusson “A semiconductor metasurface with multiple functionalities: A polarizing beam splitter with simultaneous focusing ability,” *Appl. Phys. Lett.*, **104**, 233505 (2014).

- [116] J. C. Ginn, I. Brener, D. W. Peters, J. R. Wendt, J. O. Stevens, P. F. Hines, L. I. Basilio, L. K. Warne, J. F. Ihefeld, P. G. Clen, and M. B. Sinclair, “Realizing optical magnetism from dielectric metamaterials,” *Phys. Rev. Lett.*, **108**, 097402 (2012).
- [117] F. Monticone, and A. Alù, “Leaky-wave theory, techniques, and applications: From microwaves to visible frequencies,” *Proc. IEEE*, **103** (5), 793 – 821 (2015).
- [118] S. Collin, “Nanostructure arrays in free-space: optical properties and applications,” *Rep. Prog. Phys.*, **77**, 126402 (2014).
- [119] D. Y. Kim, “Effect of the azimuthal orientation on the performance of grating-coupled surface-plasmon resonance biosensors,” *Appl. Opt.*, **44** (6), 3218 – 3223 (2005).
- [120] R. Romanato, K. H. Lee, H. K. Kang, G. Ruffato, and C. C. Wong. “Sensitivity enhancement in grating coupled surface plasmon resonance by azimuthal control,” *Opt. Exp.*, **17** (14), 12145 – 12154 (2009).
- [121] S. J. Elston, G. P. Bryan-Brown, and J. R. Sambles, “Polarization conversion from diffraction gratings,” *Phys. Rev. B*, **44**, 6393 (1991)
- [122] N. Passilly, P. Karvinen, K. Ventola, P. Laakkonen, J. Turunen, and J. Tervo, “Polarization conversion by dielectric subwavelength gratings in conical mounting,” *J. Euro. Opt. Soc.*, **3**, 08009 (2008).
- [123] M. Laroche, F. Marquier, C. Vandembem, and J. Greffet, “Polarization conversion with a photonic crystal slab,” *J. Euro. Opt. Soc.*, **3**, 08038 (2008).
- [124] Y. Li, T. Yang, S. Song, Z. Pang, G. Du, and S. Han, “Phase properties of Bloch surface waves and their sensing applications,” *Appl. Phys. Lett.*, **103**, 041116 (2013).
- [125] V. N. Konopsky, T. Karakouz, E. V. Alieva, C. Vicario, S. K. Sekatskii, and G. Dietler, “Photonic crystal biosensor based on optical surface waves,” *Sensors*, **13** (2), 2566 – 2578 (2013).

- [126] J. Borish, and J. B. Angell, “An efficient algorithm for measuring the impulse response using pseudorandom noise,” *J. Audio Eng. Soc.*, **31**, 478 – 489 (1983).
- [127] X. Sun, X. Shu, and C. Chen, “Grating surface plasmon resonance sensor: angular sensitivity, metal oxidation effect of Al-based device in optimal structure,” *Appl. Opt.*, **54** (6), 1548 – 1554 (2015).
- [128] A. Sinibaldi, A. Fieramosca, R. Rizzo, A. Anopchenko, N. Danz, P. Munzert, C. Magistris, C. Barolo, and F. Michelotti, “Combining label-free and fluorescence operation of Bloch surface wave optical sensors,” *Opt. Lett.*, **39** (10), 2947 – 2950 (2014).
- [129] W. Kong, Z. Zheng, Y. Wan, S. Li, and J. Liu, “High-sensitivity sensing based on intensity-interrogated Bloch surface wave sensors,” *Sensors and Actuators B: Chemical*, **193**, 467 – 471 (2014).
- [130] Y. Wang, J. Wu, Z. Lan, Y. Xiao, Q. Li, F. Peng, J. Lin, and M. Huang, “Preparation of porous nanoparticle TiO₂ films for flexible dye-sensitized solar cells,” *Chinese Sci. Bull.*, **56**, 2649 – 2653 (2011).
- [131] I. Bernacka-Wojcik, P. J. Wojcik, H. Aguas, E. Fortunato, and R. Martins, “Inkjet printed highly porous TiO₂ films for improved electrical properties of photoanode,” *Jour. of Colloid and Interface Sci.*, **465**, 208 – 214 (2016).
- [132] R. Rizzo, N. Danz, F. Michelotti, E. Maillart, A. anopchenko, and C. Wachter, “Optimization of angularly resolved Bloch surface wave bio-sensors,” *Opt. Exp.*, **22**, 2566 – 2578 (2013).
- [133] K. Matsubara, S. Kawata, and S. Minami, “Optical chemical sensor based on surface plasmon measurement,” *Appl. Opt.*, **27**, 1160 (1988).
- [134] L. M. Zhang, and D. Uttamchandani, “Optical chemical sensing employing surface plasmon resonance,” *Electron. Lett.*, **23**, 1469 (1988).

- [135] P.S. Vukusic, G. P. Bryan-Brown, and J. R. Sambles, “Surface plasmon resonance on grating as novel means for gas sensing,” *Sensors and Actuators B*, **8**, 155 (1992).
- [136] S. T. Koev, A. Agrawal, H. J. Leze, and V. A. Aksyuk, “An efficient large-area grating coupler for surface plasmon polaritons,” *Plasmonics*, **7**, 269 (2012).
- [137] K. M. Byun, S. J. Kim, and D. Kim, “Grating-coupled transmission-type surface plasmon resonance sensors based on dielectric and metallic gratings,” *Appl. Opt.*, **46 (23)**, 5703 (2007).
- [138] C. Hu, and D. Liu, “High-performance grating coupled surface plasmon resonance sensor based on Al-Au bimetallic layer,” *Mod. Appl. Sci.*, **4 (6)**, 8 (2010).
- [139] E. A. Kadomina, E. A. Bezus, and L. L. Doskolovich, “Diffraction-grating-based Bloch surface wave refractive index sensors,” *Comp. Opt. and Nanophotonics, Information Technology and Nanotechnology*, (ITNT-2016).
- [140] X. Kang, L. Wen, and Z. Wang, “Design of guided Bloch surface wave resonance bio-sensors with high sensitivity,” *Opt. Comm.*, **383**, 531 (2017).

APPENDICES

APPENDIX A

MODELING AZIMUTHAL BLOCH SURFACE WAVE IN COMSOL MULTIPHYSICS

COMSOL Multiphysics is a commercial finite element software widely used for numerical simulations of physical phenomena from a variety of fields such as physics, chemistry, and biology. It has been adopted in both, academic and industrial research and production. In this dissertation, we have used COMSOL Multiphysics 5.1a to model azimuthal Bloch surface waves in a 3D geometry. The geometry used here is a periodic multilayer structure of TiO_2 and SiO_2 with grating profile on the top-most SiO_2 layer. This chapter presents a step-by-step tutorial to build the geometry, define the materials, specify the appropriate boundary conditions, run the model, and visualize the results. The model described below is used to generate the results [Figure 36(e), 36(f), and 39] in chapter 6. The chapter follows the tutorial style adopted in official COMSOL Multiphysics tutorials.

A.1 Model Setup

Modeling Instructions

From the **File** menu, choose **New**.

NEW

In the **New** window, click **Model Wizard**.

MODEL WIZARD

1. In the **Model Wizard** window, click **3D**.
2. In the **Select Physics** tree, select **Radio Frequency > Electromagnetic Waves, Frequency Domain (emw)**

3. Click **Add**.
4. Click **Study**.
5. In the **Select Study** tree, select **Preset Studies**> **Frequency Domain**.
6. Click **Done**.

GLOBAL DEFINITIONS

Parameters

1. On the **Home** toolbar, click **Parameters**.
2. In the **Settings** window for Parameters, locate the **Parameters** section.
3. In the table, enter the following settings:

Table A.1: Parameters used in modeling 3D azimuthal Bloch surface wave

Name	Expression	Value	Description
dTiO ₂	126.12[nm]	1.2613E-7 m	thickness of TiO ₂
dSiO ₂	205.41[nm]	2.0541E-7 m	thickness of SiO ₂
dDefect	280.03[nm]	2.8003E-7 m	thickness of SiO ₂ defect
dGrating	70[nm]	7E-8 m	thickness of grating
ff	0.5	0.5	fillout factor
GPeriod	510[nm]	5.1E-7m	grating period
eTiO ₂	6.6755	6.6755	relative permittivity of TiO ₂
eSiO ₂	2.1229	2.1229	relative permittivity of SiO ₂
na	1.33	1.33	refractive index of superstrate
nb	sqrt(eSiO2)	1.457	refractive index of substrate
nBilayer	8	8	number of bilayers
theta	5.4[deg]	0.094248 rad	Polar angle of incidence in superstrate
phi	12[deg]	0.20944 rad	Azimuthal angle of incidence in both media
thetab	asin(na*sin(theta)/nb)	0.08601 rad	Polar angle in substrate
lmd	632.8[nm]	6.328E-7	Wavelength
f0	c.const/lmd	4.7376E14 1/s	Frequency

We specify the azimuthal angle (ϕ) to be 12° here. This value, however will not remain constant, and change while conducting parametric sweep over the azimuthal angle. It needs to be specified here so that it is accessible to the parametric solver.

A.2 Geometry Construction

GEOMETRY

Block 1 (blk1)

1. On the **Geometry** toolbar, click **Block**.
2. In the **Settings** window for Block, locate the **Size and Shape** section.
3. In the **Width** text field, type **GPeriod**.
4. In the **Depth** text field, type **GPeriod/4**.
5. In the **Height** text field, type **dTiO₂**.
6. In the **Settings** window for Block, locate the **Position** section.
7. Set **Base** to **Corner**.
8. Type **0** in the **x**, **y**, **z** text fields.
9. In the **Settings** window for Block, locate the **Axis** section.
10. Set **Axis type** to **z-axis**.
11. In the **Settings** window for Block, locate the **Rotation** section.
12. In the **Rotation** text field, type **0**.

Block 2 (blk2)

1. On the **Geometry** toolbar, click **Block**.
2. In the **Settings** window for Block, locate the **Size and Shape** section.
3. In the **Width** text field, type **GPeriod**.
4. In the **Depth** text field, type **GPeriod/4**.
5. In the **Height** text field, type **dSiO₂**.
6. In the **Settings** window for Block, locate the **Position** section.
7. Set **Base** to **Corner**.
8. Type **0** in the **x**, **y** text fields.
9. In the **z** text field, type **dTiO₂**.
10. In the **Settings** window for Block, locate the **Axis** section.
11. Set **Axis type** to **z-axis**.
12. In the **Settings** window for Block, locate the **Rotation** section.
13. In the **Rotation** text field, type **0**.

Array 1 (arr1)

We now create an array of the above defined geometries. This avoids the manual creation of the components, and helps in defining a periodic structure in a convenient way.

1. On the **Geometry** toolbar, select **Transforms** and click **Array**.
2. In the **Settings** window for Array, locate the **Input** section.
3. In the **Input objects** field, select **blk1** and **blk2**.

4. In the **Settings** window for Array, locate the **Size** section.
5. Set **Array type** to **Linear**.
6. In the **Size** text field, type **nBilayer-1**.
7. In the **Settings** window for Array, locate the **Displacement** section.
8. Type **0** in the **x, y** text fields.
9. In the **z** text field, type **dSiO₂ + dTiO₂**.

Block 3 (blk3)

1. On the **Geometry** toolbar, click **Block**.
2. In the **Settings** window for Block, locate the **Size and Shape** section.
3. In the **Width** text field, type **GPeriod**.
4. In the **Depth** text field, type **GPeriod/4**.
5. In the **Height** text field, type **dTiO₂**.
6. In the **Settings** window for Block, locate the **Position** section.
7. Set **Base** to **Corner**.
8. Type **0** in the **x, y** text fields.
9. In the **z** text field, type **(nBilayer-1)*(dTiO₂+dSiO₂)**.
10. In the **Settings** window for Block, locate the **Axis** section.
11. Set **Axis type** to **z-axis**.
12. In the **Settings** window for Block, locate the **Rotation** section.

13. In the **Rotation** text field, type **0**.

Block 4 (blk4)

1. On the **Geometry** toolbar, click **Block**.
2. In the **Settings** window for Block, locate the **Size and Shape** section.
3. In the **Width** text field, type **GPeriod**.
4. In the **Depth** text field, type **GPeriod/4**.
5. In the **Height** text field, type **dDefect**.
6. In the **Settings** window for Block, locate the **Position** section.
7. Set **Base** to **Corner**.
8. Type **0** in the **x**, **y** text fields.
9. In the **z** text field, type $(n\text{Bilayer}-1) \cdot (d\text{TiO}_2 + d\text{SiO}_2) + d\text{TiO}_2$.
10. In the **Settings** window for Block, locate the **Axis** section.
11. Set **Axis type** to **z-axis**.
12. In the **Settings** window for Block, locate the **Rotation** section.
13. In the **Rotation** text field, type **0**.

Block 5 (blk5)

1. On the **Geometry** toolbar, click **Block**.
2. In the **Settings** window for Block, locate the **Size and Shape** section.

3. In the **Width** text field, type $ff * GPeriod$.
4. In the **Depth** text field, type $GPeriod/4$.
5. In the **Height** text field, type $dGrating$.
6. In the **Settings** window for Block, locate the **Position** section.
7. Set **Base** to **Corner**.
8. In the **x** text field, type $(1-ff) * GPeriod/2$
9. In the **y** text field, type **0**
10. In the **z** text field, type $(nBilayer-1) * (dTiO_2 + dSiO_2) + dTiO_2 + dDefect$.
11. In the **Settings** window for Block, locate the **Axis** section.
12. Set **Axis type** to **z-axis**.
13. In the **Settings** window for Block, locate the **Rotation** section.
14. In the **Rotation** text field, type **0**.

Block 6 (blk6)

1. On the **Geometry** toolbar, click **Block**.
2. In the **Settings** window for Block, locate the **Size and Shape** section.
3. In the **Width** text field, type $GPeriod$.
4. In the **Depth** text field, type $GPeriod/4$.
5. In the **Height** text field, type $5 * dDefect$.
6. In the **Settings** window for Block, locate the **Position** section.

7. Set **Base** to **Corner**.
8. Type **0** in the **x, y** text fields.
9. In the **z** text field, type $(n\text{Bilayer}-1)*(d\text{TiO}_2+d\text{SiO}_2) +d\text{TiO}_2+d\text{Defect}$.
10. In the **Settings** window for Block, locate the **Axis** section.
11. Set **Axis type** to **z-axis**.
12. In the **Settings** window for Block, locate the **Rotation** section.
13. In the **Rotation** text field, type **0**.

Block 7 (blk7)

1. On the **Geometry** toolbar, click **Block**.
2. In the **Settings** window for Block, locate the **Size and Shape** section.
3. In the **Width** text field, type **GPeriod**.
4. In the **Depth** text field, type **GPeriod/4**.
5. In the **Height** text field, type **5*dDefect**.
6. In the **Settings** window for Block, locate the **Position** section.
7. Set **Base** to **Corner**.
8. Type **0** in the **x, y** text fields.
9. In the **z** text field, type **-5*dDefect**.
10. In the **Settings** window for Block, locate the **Axis** section.
11. Set **Axis type** to **z-axis**.

12. In the **Settings** window for Block, locate the **Rotation** section.
13. In the **Rotation** text field, type **0**.

Form Union (fin)

1. In the **Model Builder** window, under **Component 1 (comp1) <Geometry 1** right-click **Form Union (fin)** and choose **Build Selected**.

A.3 Material Setup

MATERIALS

In the **Model Builder** window, under **Component 1** right-click **Materials** and choose **Blank Material**.

Material 1 (mat1)

1. In the **Settings** window for Material, type **Water** in the **Label** field.
2. Locate the **Material Contents** section. In the table, enter the following settings:

Table A.2: Refractive index parameter for superstrate layer

Properties	Name	Value	Unit	Property group
Refractive index	n	na	1	Refractive index

Material 2 (mat2)

1. Right-click **Materials** and choose **Blank Material**.
2. In the **Settings** window for Material, type **SiO₂** in the **Label** field.
3. Select Domains 1, 3, 5, 7, 9, 11, 13, 15, 17, and 19.

Table A.3: Refractive index parameter for SiO₂

Properties	Name	Value	Unit	Property group
Refractive index	n	sqrt(eSiO ₂)	1	Refractive index

4. Locate the **Material Contents** section. In the table, enter the following settings:

Material 3 (mat3)

1. Right-click **Materials** and choose **Blank Material**.
2. In the **Settings** window for Material, type **TiO₂** in the **Label** field.
3. Select Domains 2, 4, 6, 8, 10, 12, 14, and 16.
4. Locate the **Material Contents** section. In the table, enter the following settings:

Table A.4: Refractive index parameter for TiO₂

Properties	Name	Value	Unit	Property group
Refractive index	n	sqrt(eTiO ₂)	1	Refractive index

The structure geometry at this point should look like the geometry shown in Figure 40.

A.4 Physics Setup

ELECTROMAGNETIC WAVES, FREQUENCY DOMAIN (EMW)

1. In the **Model Builder** window, under **Component 1 (comp1)** click **Electromagnetic Waves, Frequency Domain (emw)**.
2. In the **Settings** window, locate the **Settings** section.
3. From the **Solve for** list, choose **Full field**.

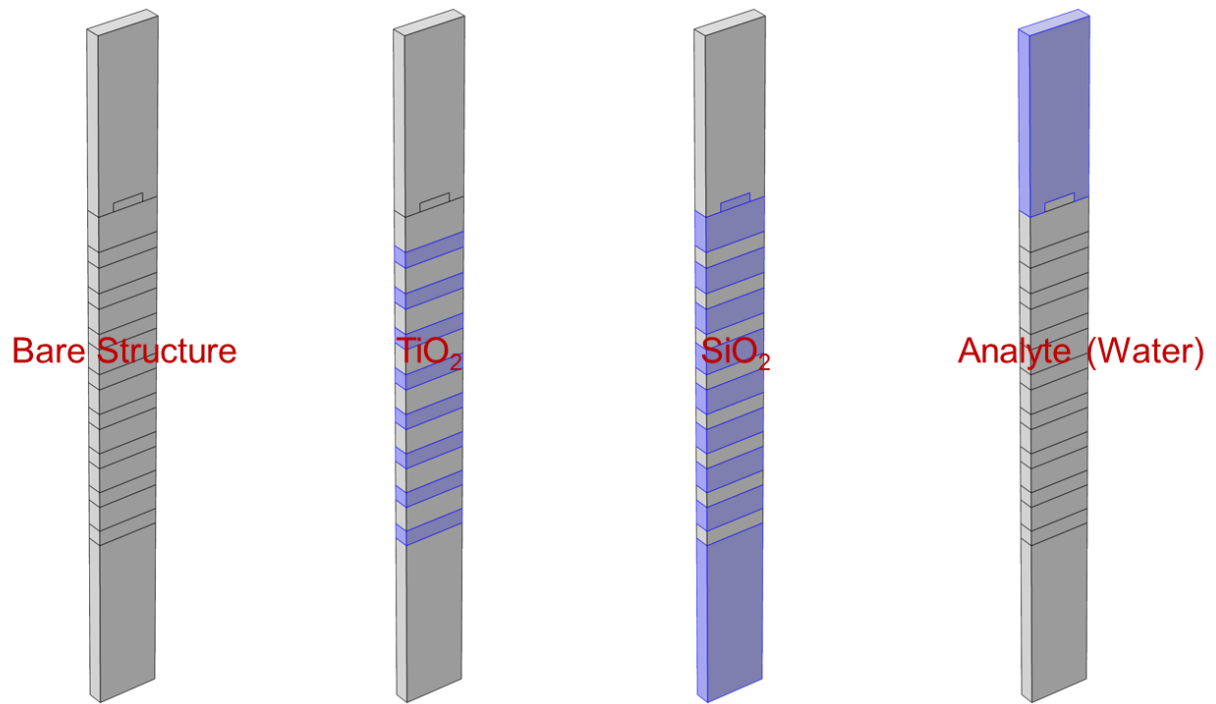


Figure 40: Geometries of multilayer structure with grating profile showing different components

Port 1

Defining port boundary conditions correctly is crucial in modeling BSWs. In 2D modeling, it is relatively easier to set the port boundaries up. However, while modeling BSWs in 3D, special care has to be taken. In order to specify the direction of input waves into the structure and output waves exiting the structure correctly, we need to use 'periodic port reference point' at both the ports. This helps in correct implementation of the reference coordinates at the input and output ports.

1. On the **Physics** toolbar, click **Boundaries** and choose **Port**.
2. Select Boundary 55 only.
3. In the **Settings** window for Port, locate the **Port Properties** section.
4. From the **Type of port** list, choose **Periodic**.

5. From the **Wave excitation at this port** list, choose **On**.
6. Locate the **Port Mode Settings** section. Specify the \mathbf{E}_0 vector as **sin(phi), cos(phi), 0** for **x, y, z** components.
7. In the α_1 text field, type **theta**.
8. In the α_2 text field, type **phi**.
9. In the n text field, type **na**.
10. In the f_{max} text field, type **na**.

Periodic Port Reference Point

1. Right-click on **Port 1** and select **Periodic Port Reference Point 1**.
2. On the **Settings** window for Periodic Port Reference Point 1, locate the **Point Selection** section.
3. From the **Selection** list, choose **bManual**.
4. Select Point 19 only.

Diffraction Order 1

1. Right-click on **Port 1** and select **Diffraction Order**.
2. In the **Settings** window for Diffraction Order, locate the **Port Mode Settings** section.
3. From the **Components** list, choose **Out-of-plane vector**.
4. In the m text field, type 1.

5. In the n text field, type 0.
6. In the θ_{in} text field, type 0.

Diffraction Order 2

1. Right-click on **Port 1** and select **Diffraction Order**.
2. In the **Settings** window for Diffraction Order, locate the **Port Mode Settings** section.
3. From the **Components** list, choose **Out-of-plane vector**.
4. In the m text field, type -1.
5. In the n text field, type 0.
6. In the θ_{in} text field, type 0.

Diffraction Order 3

1. Right-click on **Port 1** and select **Diffraction Order**.
2. In the **Settings** window for Diffraction Order, locate the **Port Mode Settings** section.
3. From the **Components** list, choose **In-plane vector**.
4. In the m text field, type 1.
5. In the n text field, type 0.
6. In the θ_{in} text field, type 0.

Diffraction Order 4

1. Right-click on **Port 1** and select **Diffraction Order**.
2. In the **Settings** window for Diffraction Order, locate the **Port Mode Settings** section.
3. From the **Components** list, choose **In-plane vector**.
4. In the m text field, type -1.
5. In the n text field, type 0.
6. In the θ_{in} text field, type 0.

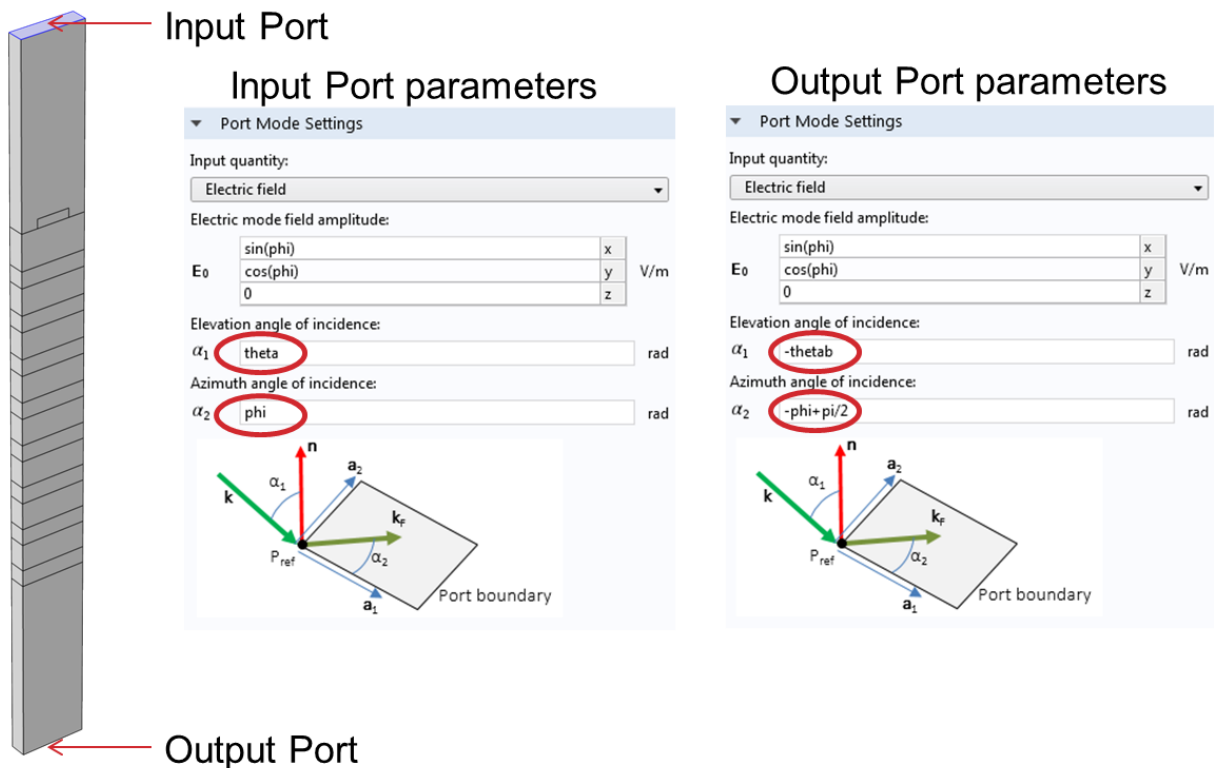


Figure 41: Input and output port boundary condition parameters

The input and output ports, and their parameter specifications are shown in Figure 41.

Port 2

1. On the **Physics** toolbar, click **Boundaries** and choose **Port**.
2. Select Boundary 3 only.
3. In the **Settings** window for Port, locate the **Port Properties** section.
4. From the **Type of port** list, choose **Periodic**.
5. From the **Wave excitation at this port** list, choose **Off**.
6. Locate the **Port Mode Settings** section. Specify the \mathbf{E}_0 vector as **sin(phi), cos(phi)**, **0** for **x, y, z** components.
7. In the α_1 text field, type **-thetab**.
8. In the α_2 text field, type **-phi+pi/2**.
9. In the n text field, type **nb**.
10. In the f_{max} text field, type **na**.

Periodic Port Reference Point

1. Right-click on **Port 2** and select **Periodic Port Reference Point 1**.
2. On the **Settings** window for Periodic Port Reference Point 1, locate the **Point Selection** section.
3. From the **Selection** list, choose **bManual**.

4. Select Point 66 only.

Diffraction Order 1

1. Right-click on **Port 1** and select **Diffraction Order**.
2. In the **Settings** window for Diffraction Order, locate the **Port Mode Settings** section.
3. From the **Components** list, choose **Out-of-plane vector**.
4. In the m text field, type 1.
5. In the n text field, type 0.
6. In the θ_{in} text field, type 0.

Diffraction Order 2

1. Right-click on **Port 1** and select **Diffraction Order**.
2. In the **Settings** window for Diffraction Order, locate the **Port Mode Settings** section.
3. From the **Components** list, choose **Out-of-plane vector**.
4. In the m text field, type -1.
5. In the n text field, type 0.
6. In the θ_{in} text field, type 0.

Diffraction Order 3

1. Right-click on **Port 1** and select **Diffraction Order**.
2. In the **Settings** window for Diffraction Order, locate the **Port Mode Settings** section.
3. From the **Components** list, choose **In-plane vector**.
4. In the m text field, type 1.
5. In the n text field, type 0.
6. In the θ_{in} text field, type 0.

Diffraction Order 4

1. Right-click on **Port 1** and select **Diffraction Order**.
2. In the **Settings** window for Diffraction Order, locate the **Port Mode Settings** section.
3. From the **Components** list, choose **In-plane vector**.
4. In the m text field, type -1.
5. In the n text field, type 0.
6. In the θ_{in} text field, type 0.

Periodic Condition 1

1. Right-click on **Electromagnetic Waves, Frequency Domain (emw)** and select **Periodic Condition**.
2. Select Boundaries 2, 5, 8, 11, 14, 17, 20, 23, 26, 29, 32, 35, 38, 41, 44, 47, 50, 53, 56-73, 78.

3. In the **Settings** window for Periodic Condition, locate the **Periodicity Settings** section.
4. From the **Type of periodicity** list, choose Floquet periodicity.
5. From the **k-vector for Floquet periodicity** list, choose [From periodic port].

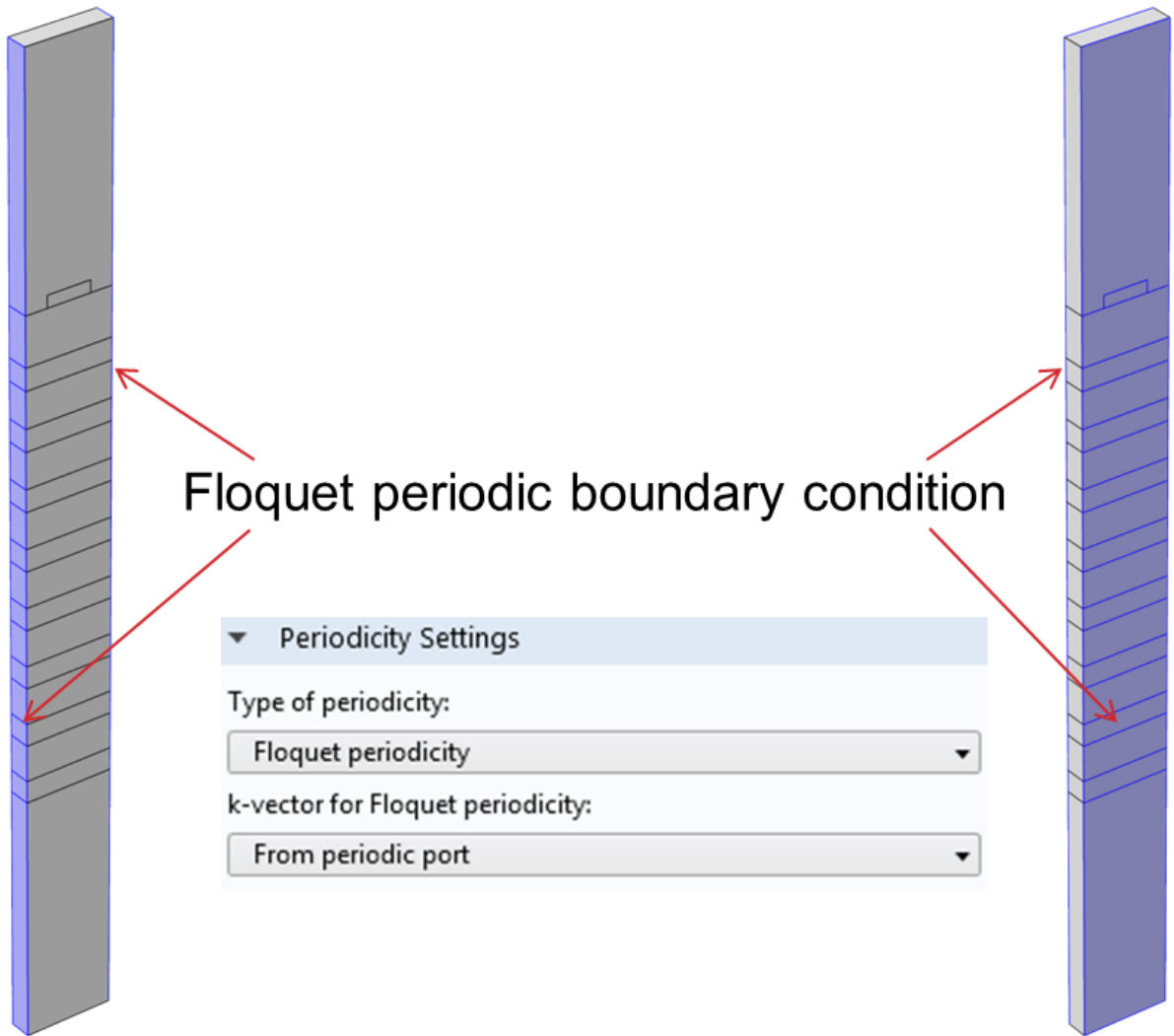


Figure 42: Floquet periodic boundary condition parameters

Periodic boundary condition specifications are shown in Figure 42.

Periodic Condition 2

1. Right-click on **Electromagnetic Waves, Frequency Domain (emw)** and select **Periodic Condition**.
2. Select Boundaries 1, 4, 7, 10, 13, 16, 19, 22, 25, 28, 31, 34, 37, 40, 43, 46, 49, 52, 81-98.
3. In the **Settings** window for Periodic Condition, locate the **Periodicity Settings** section.
4. From the **Type of periodicity** list, choose Floquet periodicity.
5. From the **k-vector for Floquet periodicity** list, choose [**From periodic port**].

A.5 Mesh Setup

Meshing the geometry is an important aspect of finite element simulation. The resolution of the mesh has a significant importance in determining the accuracy of the numerical simulation. As a rule of thumb, the smallest mesh element size in finite element is typically one-tenth of a wavelength. The mesh parameters used in our simulation are shown below and in Figure 43.

MESH 1

1. In the **Model Builder** window, under **Component 1 (comp1)** click **Mesh 1**.
2. In the **Settings** window for Mesh, locate the **Mesh Settings** section.
3. From the **Sequence type** list, choose **User-controlled mesh**.

Size

1. In the **Settings** window for Size, locate **Element Size** section.
2. From the **Calibrate for** list, choose **General physics**.
3. Click on the **Custom** radio button.
4. In the **Settings** window for Size, locate **Element Size Parameters** section.
5. In the **Maximum element size** text field, type 0.555E-7.
6. In the **Minimum element size** text field, type 1.11E-7.
7. In the **Maximum element growth rate** text field, type 1.3.
8. In the **Curvature factor** text field, type 0.2.
9. In the **Resolution of narrow regions** text field, type 1.

Free Triangular 1

1. Right-click on **Mesh 1**, under **More Operations** choose **Free Triangular**.
2. In the **Settings** window for Free Triangular 1, locate **Boundary Selection** section.
3. From the **Geometry entity level** list, choose **Boundary**.
4. From the **Selection** list, choose **Manual**.
5. Select the **Active** toggle button.
6. Select Boundaries 1, 4, 7, 10, 13, 16, 19, 22, 25, 28, 31, 34, 37, 40, 43, 46, 49, and 52.

Copy 1

1. Right-click on **Mesh 1**, under **More Operations** choose **Copy**.

2. In the **Settings** window for Copy 1, locate **Source Entities** section.
3. From the **Selection** list, choose **Manual**.
4. Select the **Active** toggle button.
5. Select Boundaries 1, 4, 7, 10, 13, 16, 19, 22, 25, 28, 31, 34, 37, 40, 43, 46, 49, and 52.
6. In the **Settings** window for Copy 1, locate **Destination Entities** section.
7. From the **Selection** list, choose **Manual**.
8. Select the **Active** toggle button.
9. Select Boundaries 81-98.

Free Triangular 2

1. Right-click on **Mesh 1**, under **More Operations** choose **Free Triangular**.
2. In the **Settings** window for Free Triangular 2, locate **Boundary Selection** section.
3. From the **Geometry entity level** list, choose **Boundary**.
4. From the **Selection** list, choose **Manual**.
5. Select the **Active** toggle button.
6. Select Boundaries 2, 5, 8, 11, 14, 17, 20, 23, 26, 29, 32, 35, 38, 41, 44, 47, 50, 53, and 75.

Copy 2

1. Right-click on **Mesh 1**, under **More Operations** choose **Copy**.
2. In the **Settings** window for Copy 2, locate **Source Entities** section.

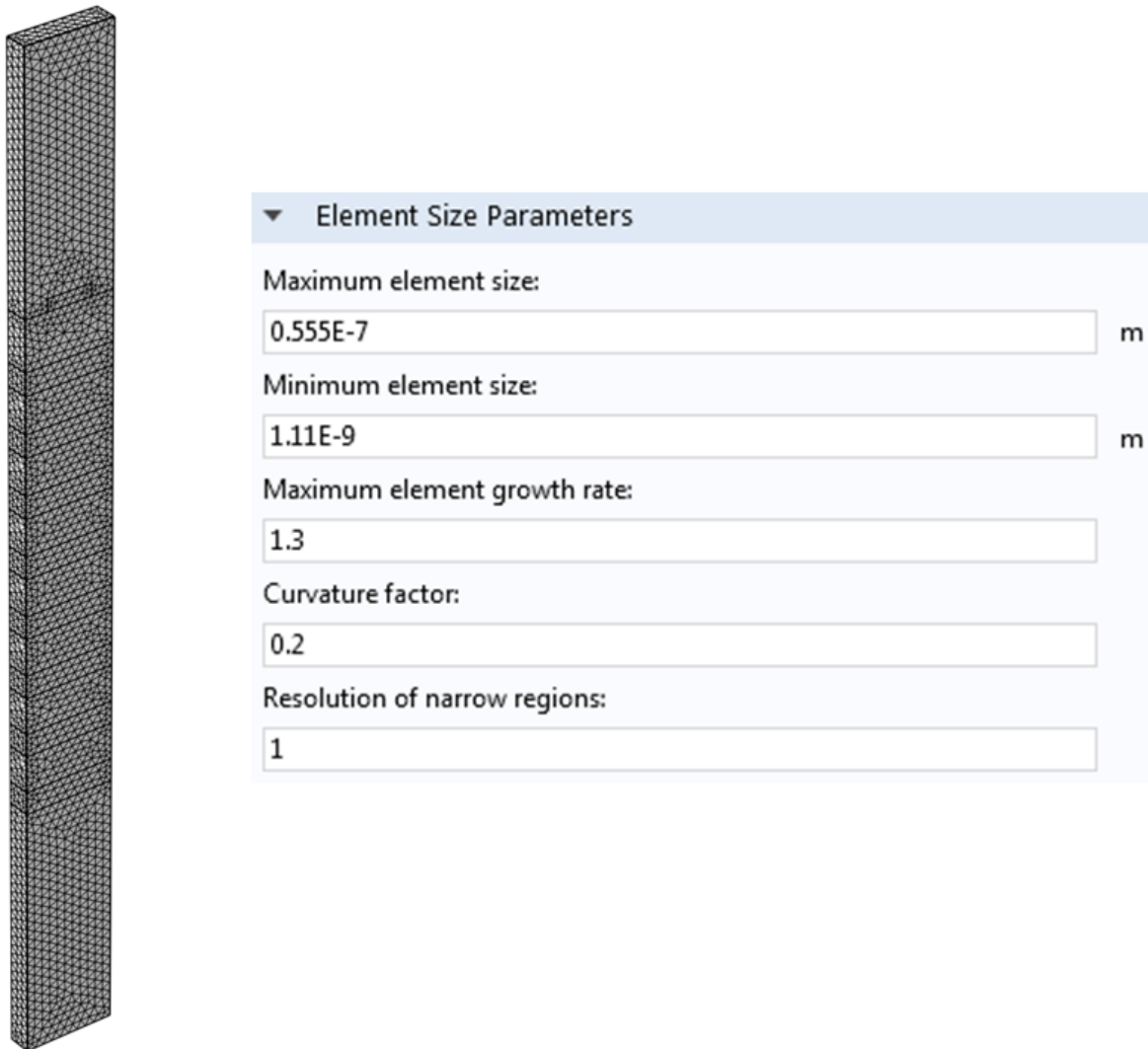


Figure 43: Mesh parameters

3. From the **Selection** list, choose **Manual**.
4. Select the **Active** toggle button.
5. Select Boundaries 2, 5, 8, 11, 14, 17, 20, 23, 26, 29, 32, 35, 38, 41, 44, 47, 50, 53, and 75.
6. In the **Settings** window for Copy 2, locate **Destination Entities** section.
7. From the **Selection** list, choose **Manual**.

8. Select the **Active** toggle button.

9. Select Boundaries 56-78.

Free Tetrahedral 1

1. Right-click on **Mesh 1**, choose **Free Tetrahedral**.

2. In the **Settings** window for Free Tetrahedral 1, locate **Domain Selection** section.

3. From the **Geometry entity level** list, choose **Remaining**.

4. Select the **Active** toggle button.

STUDY 1

Step 1: Frequency Domain

1. In the **Settings** window for Frequency Domain, locate the **Study Settings** section.

2. In the **Frequencies** text field, type **f0**.

Parametric Sweep

1. On the **Study** toolbar, click **Parametric Sweep**.

2. In the **Settings** window for Parametric Sweep, locate **Study Settings** section.

3. Click **Add**.

4. From the **Parameter name** dropdown menu, choose **phi (Azimuthal angle of incidence in both media)**.

5. Click **Range**.

6. In the **Range** dialog box, type 0[deg] in the **Start** text field.
7. In the **Stop** text field, type 10[deg].
8. In the **Number of values**, type 11.
9. Click **Replace**.
10. Click **Range**.
11. In the **Range** dialog box, type 10.1[deg] in the **Start** text field.
12. In the **Stop** text field, type 14.5[deg].
13. In the **Number of values**, type 100.
14. Click **Add**.
15. Click **Range**.
16. In the **Range** dialog box, type 15[deg] in the **Start** text field.
17. In the **Stop** text field, type 20[deg].
18. In the **Number of values**, type 5.
19. Click **Add**.
20. On the **Study** toolbar, click **Compute**.

A.6 Results

RESULTS

The results presented in Figure 44 and 45 are a subset of the results described in chapter 6.

Electric Field (emw)

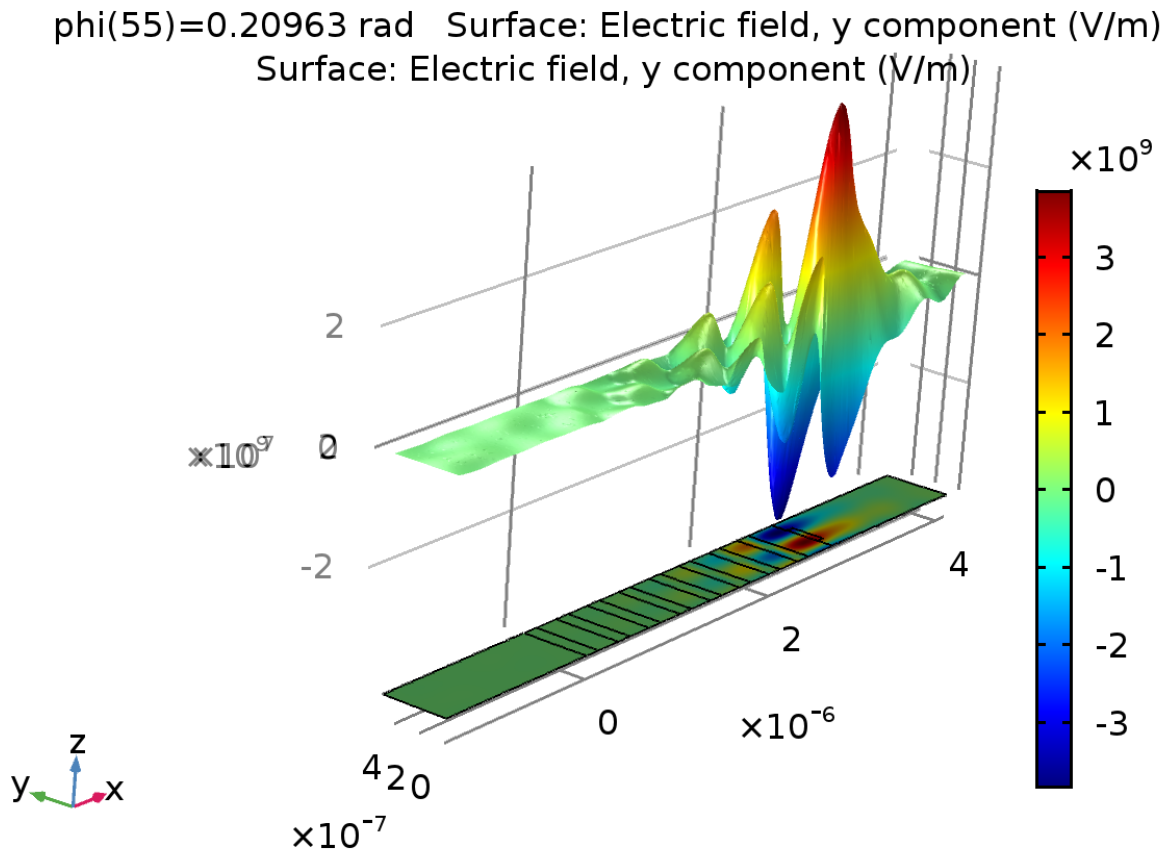


Figure 44: Electric field profile, y component, of azimuthal Bloch surface wave

1. Right-click on **Results** and select **2D Plot Group**.
2. Locate the **Data** section. From the **Parametric value (phi (rad))** list, choose 0.20963.
3. Right-click on **2D Plot Group 1** and select **Surface**.
4. Locate the **Data** section. From the **Data set** list, choose **From parent**.
5. In the **Expression** text field, type **emw.Ey**.
6. Right-click on **Surface 1** and choose **Height Expression**.
7. In the **Offset** text field, type 1.6E-6.

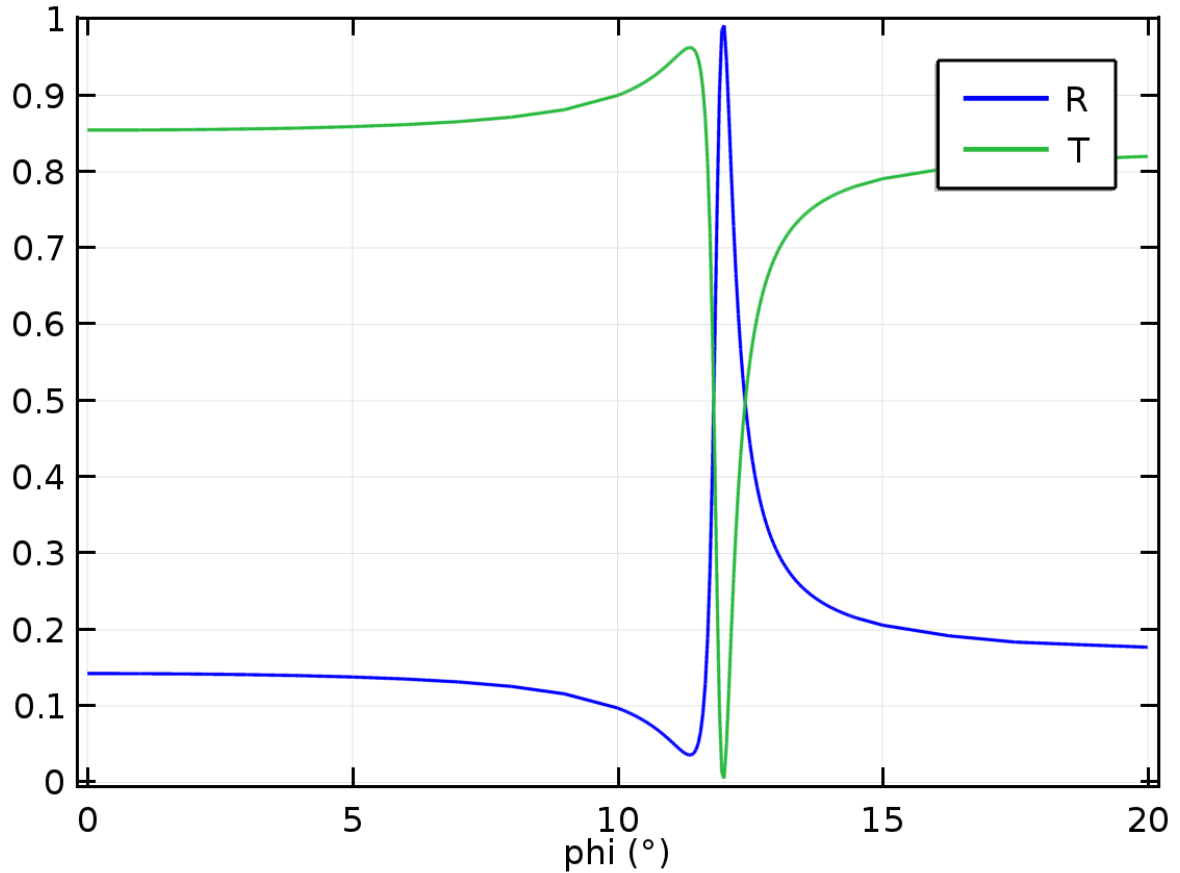


Figure 45: Reflectance (R) and Transmittance (T) of azimuthal Bloch surface wave

8. Right-click on **2D Plot Group 1** and select **Surface**.

9. Locate the **Data** section. From the **Data set** list, choose **From parent**.

10. In the **Expression** text field, type **emw.Ey**.

11. On the **2D Plot Group 1** toolbar, click **Plot**.

1D Plot Group 2

1. Right-click on **Results** and select **1D Plot Group**.

2. Right-click on **1D Plot Group 2** and select **Global**.

3. In the **Settings** window for Global, locate **y-Axis Data** section.
4. In the table, enter the following settings:

Table A.5: Reflectance and Transmittance from S-parameters

Expression	Unit	Description
$\text{abs}(\text{emw.S11})^2$	1	R
$\text{abs}(\text{emw.S21})^2$	1	T

5. Locate the **x-Axis Data** section. From the **Parameter** list, choose **Parameter value**.
6. From the **Unit** list, choose 0 .
7. On the **1D Plot Group 2** toolbar, click **Plot**.